Master thesis and internship[BR]- Master's thesis : A new RANS-based added turbulence intensity model for wind farm flow modelling[BR]- Integration Internship : Technical University of Denmark

Auteur : Delvaux, Théo
Promoteur(s) : Terrapon, Vincent
Faculté : Faculté des Sciences appliquées
Diplôme : Master en ingénieur civil en aérospatiale, à finalité spécialisée en "aerospace engineering"
Année académique : 2022-2023
URI/URL : http://hdl.handle.net/2268.2/17869

Université de Liège - Faculté des Sciences Appliquées

A new RANS-based added turbulence intensity model for wind farm flow modelling

---

Travail de fin d'études réalisé en vue de l'obtention du grade de master Ingénieur Civil en Aérospatiale par Delvaux Théo

Année académique
2022-2023

Superviseurs
Terrapon Vincent
van der Laan Paul

Abstract

When placed in the wake of an upstream rotor, a wind turbine is subjected to significant power reductions. The modelling of wind turbine wakes is therefore a subject of growing importance, as part of a broader drive to develop renewable energies worldwide. Typically, wind farms comprise dozens of turbines, for which conventional methods of flow simulation quickly become unfeasible. For this reason, engineering wake models are used to give fast and reliable estimates of the Annual Energy Production of wind farms. One of these models, currently under development at the Technical University of Denmark, is based on a RANS look-up table of wakes, generated for a stand-alone wind turbine under various flow conditions. Despite promising results, this method is currently limited by its high memory requirements. Therefore, the aim of this work is to design a new wake model capable of faithfully replacing the look-up table. In particular, emphasis is placed on the development of a new added turbulence intensity model. First, several expressions for a one-dimensional single-wake model are investigated. The retained model is then generalized to higher dimensions and studied in parallel to a velocity deficit model. Finally, the new wake model is implemented in the PyWake software, with which wake superposition methods are used to analyze the flow characteristics in the merged wakes of an array of five wind turbines. It results that, whether used in single or multiple wake situations, the new model developed in this work faithfully represents the predictions of the RANS look-up table model. In addition, an in-depth analysis of the superposition methods supports the physical interpretation, still debated today, of some of these methods.

Acknowledgments

First of all, I would like to thank my supervisor, Dr. van der Laan, for his enthusiastic welcome to the Department of Wind and Energy Systems at the Technical University of Denmark. His willingness to help and his judicious advice helped me considerably in this project. His passion for the topic has been a real source of inspiration for me, confirming my choice of future career.

I would also like to thank Professor Terrapon for his availability and advice throughout this work as well as for his involvement in my search for a PhD position.

I finally want to thank my parents for always believing in me and helping me as much as they could. Last but not least, thank you to my girlfriend, Lola Charles, for always supporting me, both in this project and in my everyday life. Thank you.

Contents

Chapter 1

Introduction

1.1 Context and motivation

Before delving into the details of wind farm flow modelling, a quick overview of the main characteristics of a wake flow is provided. Far upstream of a wind turbine, the air flow is considered undisturbed. Two key quantities are used to describe it, *i.e.* the mean speed U_∞ and the level of atmospheric turbulence intensity Ti_k^0. While the former has a fairly intuitive definition, the latter will be precisely defined in the next section of this work. In the few meters upstream of the rotor, the presence of the turbine has an impact on the flow, the velocity of which begins to decrease. This region is known as the induction zone, and is a symptomatic feature of a wider phenomenon called the blockage effect. This effect represents the tendency of a fraction of the flow to bypass the rotor, and on a larger scale, the entire wind farm. In practice, the operating regime of a wind turbine is defined in terms of the thrust and power coefficients, respectively denote C_T and C_P. Those two coefficients are linked to the total thrust force T on the blades and to the harnessed power P as

$$C_T = \frac{T}{\frac{1}{2}\,\rho\,U^2\,A} \quad \text{and} \quad C_P = \frac{P}{\frac{1}{2}\,\rho\,U^3\,A}. \tag{1.1}$$

In these expressions, ρ is the air density, U is the local incoming velocity and A is the rotor area. Intuitively, C_T is a measurement of the magnitude of the footprint left by the turbine on the flow and C_P is the fraction of power collected relative to the total wind power passing through the rotor. The power is harnessed by extracting momentum from the flow, causing a significant velocity deficit, ΔU, right downstream of the turbine. Besides, the velocity gradients between this region and the surrounding flow result in a large production of turbulent kinetic energy, and therefore a higher level of turbulence intensity. This increment of turbulence is referred to as the added turbulence intensity, $\Delta\mathrm{Ti}_k$. As the downstream distance increases, the diffusion of momentum from the surrounding flow to the wake reduces the velocity deficit. This effect is known as the wake recovery process. A key element to keep in mind is that the turbulence intensity in the wake enhances the mixing with the undisturbed flow and therefore leads to faster wake recoveries. An insight of the velocity and turbulence intensity fields in the wake of a stand-alone wind turbine is depicted in Fig. 1.1. The data how been generated for a

NREL-5MW turbine using LES [1] and RANS [2] simulations. Fig. 1.1 gives a clear overview of the general shape of the wake, and highlights the different degrees of fidelity specific to LES and RANS.

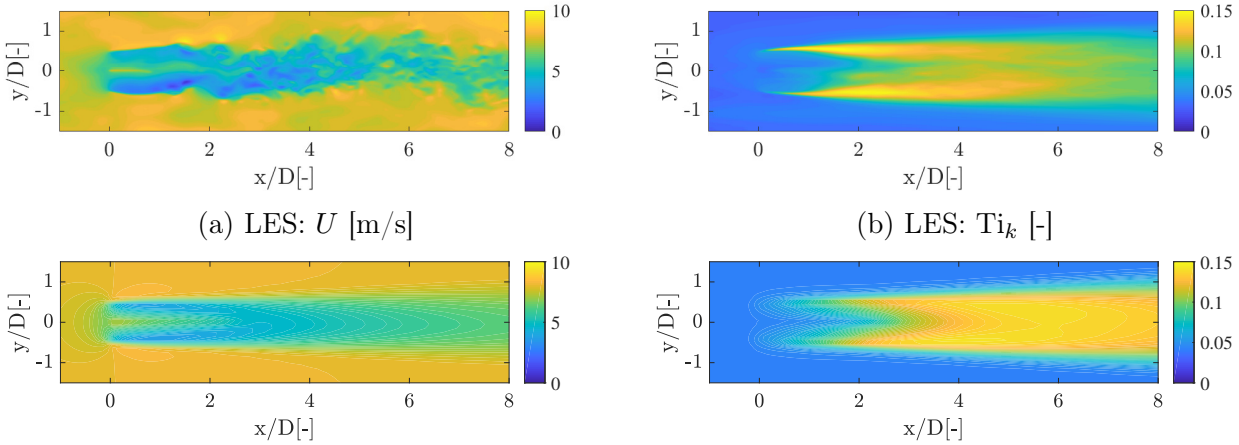

(a) LES: U [m/s]

(b) LES: Ti_k [-]

(c) RANS: U [m/s]

(d) RANS: Ti_k [-]

Figure 1.1: Overview of the velocity (left) and turbulence intensity fields (right) in the wake of a NREL-5MW rotor at $\mathrm{Ti}_k^0 = 0.04$ and $C_T \simeq 0.7$. The upper and lower figures show the LES and the RANS predictions, respectively.

In order to dispense with cumbersome and time-consuming RANS or LES simulations of wind farms, several engineering models have been developed. In general, those models tackle the description of the evolution of ΔU and $\Delta \mathrm{Ti}_k$ in the wake of a stand-alone turbine. When considering arrays of wind turbines, the single-wake models can be seen as building blocks that are combined together through superposition methods to represent the merged wake. It is important to point out that these superposition methods have no strong physical basis to date, and are therefore currently the subject of a considerable number of research studies.

In this context, a single-wake engineering model, currently under development at the Technical University of Denmark, consists in a large look-up table containing the velocity deficit and the added turbulence intensity at any point in a three-dimensional domain. Moreover, these quantities have been generated under a wide variety of conditions and are intended to provide a comprehensive RANS-based single-wake model. This approach provides highly reliable building blocks that can be used in parallel to superposition methods in multiple-wake situations. Still, the use of this model is limited by its substantial memory requirements. Hence, the aim of this work is to provide a memory-efficient and equally reliable alternative to the look-up table model. In particular, the focus is on improving the modelling of added turbulence intensity, which has so far been the subject of little research works.

1.2 State of the art

1.2.1 Velocity field in the wake of a stand-alone turbine

The modelling of the velocity field in the wake of a single wind turbine has been the topic of a large number of research studies over the past decades. Since the second half of the twentieth century, numerous models have been proposed and tested against numerical predictions of increasing fidelity. In parallel, the development of remote measurement devices such as Sodar [3] and Lidar [4] has enabled to collect measurements of full-scale wind field, which have been wildly used to calibrate the velocity deficit models. Among all the existing wake models, this section aims at presenting the main velocity deficit models that are currently used to estimate the velocity deficit generated in the wake of a stand-alone wind turbine.

Although the performance of this model has now been surpassed by that of more recent models, the Jensen model [5] is considered one of the pioneers of the field and is still in use today. The initial expression proposed by Jensen stems from the conservation of mass over a cylindrical control volume that encompass the rotor and is later re-written by Katic et al. [6] in term of the thrust coefficient C_T of the turbine:

$$\frac{\Delta U}{U_\infty} = \frac{1 - \sqrt{1 - C_T}}{(1 + 2\,k\,x/D)^2}, \tag{1.2}$$

where ΔU is the velocity deficit with respect to the undisturbed velocity U_∞, D is the diameter of the rotor and x is the downstream distance behind it. In this early model, the value of the wake decay constant k is set to 0.075 and accounts for the expansion of the wake width as well as for the reduction of the deficit with increasing downstream distances. Note that other values of the k coefficients have been proposed in Barthelmie et al. [7], *i.e.* $k = 0.04 \sim 0.05$, for offshore conditions, specifically. In the initial Jensen model [5], the velocity field is assumed to have a simple top hat distribution, the amplitude of which is given by Eq. 1.2. Hence, the model predictions have been observed to be marred by a non-physical discontinuity between the undisturbed flow field and the wake region. However, implementations of the Jensen model [5] are available in many wind farm flow modelling software, *e.g.* WAsP [8] or PyWake [9], and are still commonly used in practice.

More recently, Nygaard [10] proposed a variation of the Jensen model based on the assumption that the wake growth depends on the local level of turbulence intensity, denoted $\mathrm{Ti}_u(x)$, in the wake:

$$\frac{dD_w}{dx} = A\,\mathrm{Ti}_u(x), \tag{1.3}$$

where $D_w(x)$ is the local diameter of the wake at distance x from the rotor and A is a calibration constant. In order to close the model (Eq. 1.3), Nygaard follows the expression suggested by Frandsen [11] for the turbulence intensity in the wake. The exact definition of this quantity as well as details on the Frandsen model are given in Sec. 1.2.2. Contrary to the initial Jensen model (Eq. 1.2), Eq. 1.3 accounts for the effect of turbulence on the wake recovery and allows to leave out the assumption of linear wake growth. For a value of the calibration coefficient

$A = 0.6$, the Nygaard model (Eq. 1.3) was used to evaluate the impact that the wake created by the Humber Gateway wind farm has on the neighbouring wind farm of Westermost Rough, UK. This benchmark study concluded that the power predictions of the Nygaard model outperformed that of the classical Jensen model when compared to the actual power measurements. For that reason, the promising expression Eq. 1.3 will be further investigated later in this work (Sec. 3.2.1).

A few years after the development of the original Jensen model, Larsen [12] proposes a velocity deficit model based on the RANS axisymmetric form of the Navier-Stokes equations. The continuity and momentum equations are simplified under the assumptions of a steady and self-similar flow at high Reynolds number. The Prandtl's mixing length model, where the characteristic length is selected as the wake width, is used to close the set of equations. The latter is then solved analytically for a small perturbation of the velocity field using first, and alternatively second, order approximations. The resulting velocity deficit and wake growth are respectively found to evolve as $\Delta U \sim x^{-2/3}$ and $r_w \sim x^{1/3}$. In contrast to the non-physical profile of the Jensen [5] model, Larsen's development leads to a continuous velocity deficit profile reminiscent of a Gaussian function. Later, a modification of the boundary conditions used to solve the set of equations is proposed in order to account for multiple wakes, leading to a second version of the Larsen model [13].

In Frandsen [14], the mass and momentum conservation equations are both written over the cylindrical control volume introduced by Jensen. Assuming a steady, self-similar and axisymmetric wake, Frandsen derives the following equation:

$$\frac{\Delta U}{U_\infty} = \frac{1}{2}\left(1 - \sqrt{1 - \frac{2\,C_T}{\beta + \alpha x/D}}\right) \quad \text{with} \quad \beta = \frac{1 + \sqrt{1 - C_T}}{2\sqrt{1 - C_T}}, \tag{1.4}$$

in which the wake growth coefficient α is estimated to be around ten times the value of the k coefficient used in Jensen [5] (Eq. 1.2). In the same work, the generalization of this model to a row of wind turbines is made possible by the development of a recursive scheme. Although the model accounts for momentum conservation and is therefore physically more comprehensive than the Jensen model, Frandsen [14] still relies on the strong assumption that, at each downstream position, the velocity deficit is evenly distributed in the plane perpendicular to the flow.

In light of the results of the Frandsen [14] model, Bastankhah and Porté-Agel[15] suggest to relax the straight velocity profile assumption by introducing the self-similar relation:

$$\frac{\Delta U}{U_\infty} = C(x)\, f(r/\delta(x)) \quad \text{with} \quad f = \exp\left(\frac{-r^2}{2\sigma^2}\right), \tag{1.5}$$

where r is the radial distance from the center of the rotor and $\delta(x) = \sigma(x)$ the characteristic wake width at each downstream position. Note that the choice of a Gaussian self-similar function is inspired by the shape of the wakes behind bluff bodies, for which numerous studies exist. Following the approach introduced by Frandsen [14], Eq. 1.5 is injected in the mass and

momentum conservation equations so as to retrieve the analytical form of $C(x)$. Similarly to Jensen [5], Bastankhah and Porté-Agel [15] assume a linear wake growth, *i.e.* $\sigma \sim k\,x$, and retrieve the values of k from LES simulations under various flow conditions. As a direct result of the wake recovery phenomenon, Bastankhah and Porté-Agel observe that the wake expansion coefficient k tends to significantly increase with the level of atmospheric turbulence in the incoming flow. Eventually, provided that the value of the expansion coefficient k is known, the model proposed by Bastankhah and Porté-Agel is shown to offer significant improvements in terms of velocity field and power estimations. On a relevant note, it should be recalled that alternatives to the simple linear wake growth exist. For example, Shapiro et al. [16] derive distinct expressions for the vertical and the horizontal wake growths, *i.e.* $\sigma(x)_y$ and σ_z, in which the wake width remains essentially constant before linearly increasing in the far wake.

In the continuation of the work of Bastankhah and Porté-Agel [15], Niayifar and Porté-Agel [17] use the set of measurements for k from [15] to derive a linear empirical law for the evolution of the wake expansion coefficient with respect to the level of incoming turbulence intensity. The performance of the full model for the velocity deficit are then assessed using LES simulations of the Horns Rev1 wind farm. To do so, the velocity deficit model is used in parallel with the Crespo and Hernandez [18] model for the added turbulence intensity model. Overall, the resulting model shows good agreement with the LES and substantial improvements compared to the predictions of the WAsP [8] software. In light of these results, the Niayifar and Porté-Agel model [17] is further investigated in Sec. 3.1.1 and used together with the new model for the added turbulence intensity developed in Sec. 2.4.1. For the sake of brevity, the expressions of the deficit amplitude $C(x)$, the standard deviation $\sigma(x)$ (Eq. 1.5) and the wake expansion coefficient k are explicitly given in Sec. 3.1.1.

Although Niayifar and Porté-Agel [17] provides close estimate of the power in the Horns Rev wind farm, it is important to bear in mind that the model is not flawless. For example, recent work by Lingkan and Buxton [19] suggest that the amplitude of the deficit evolves as $\Delta U_{max} \sim x^{-2}$, whereas Niayifar predicts $\Delta U_{max} \sim x^{-1}$, as seen in Sec. 3.1.1. In Lingkan and Buxton [19], the emphasis is on the experimental study of the evolutions of the velocity deficit and the added turbulence in the wake. The wind tunnel measurements are performed using a hot wire probe in the wake of porous disks, placed either in stand-alone or columnar configuration. These very recent experimental data will be used several times in this work to keep a critical eye on the results of the various models discussed.

To conclude this section, a brief overview of the model proposed by Blondel [20] is given. The main idea of this model is to generalize the self-similarity assumption to the near wake, using a Gaussian function of order n. A corrective term for the near-wake is then introduced and the value of the n parameter is determined such that the equations of conservation of mass and momentum remain verified. Although this model shows promising results, it should be kept in mind that it requires empirical calibration of a large number of parameters.

1.2.2 Turbulence intensity field in the wake of a stand-alone turbine

As mentioned earlier, the turbulence intensity enhances the mixing of the wake with the undisturbed air and therefore plays an important part in the recovery process of the velocity deficit. In the most recent deficit models introduced in Sec. 1.2.1, the level of turbulence directly impacts the wake expansion coefficient k, simultaneously affecting both the recovery rate and the wake growth. While, for a stand-alone turbine, the atmospheric turbulence intensity is dominant, the level of turbulence intensity added by the upstream turbines should be considered in multiple-wake situations. For that reason, this section focuses on a review of existing added turbulence intensity models and their main features.

Before going any further, the general definition of the turbulence intensity Ti_k and that of the streamwise turbulence intensity Ti_u are recalled hereafter:

$$\mathrm{Ti}_k = \sqrt{\frac{2}{3}}\frac{\sqrt{k}}{U} \quad \text{with} \quad k = \frac{\sigma_u^2 + \sigma_v^2 + \sigma_w^2}{2} \tag{1.6}$$

and

$$\mathrm{Ti}_u = \frac{\sigma_u}{U}. \tag{1.7}$$

In Eq. 1.6 and Eq. 1.7, U is the mean flow velocity, k is the turbulent kinetic energy and σ_u is the standard deviation of the wind speed fluctuations along the downstream direction. Two similar quantities, σ_v and σ_w, can be defined to respectively account for the turbulent fluctuations along the transverse and the vertical directions. Measurements of the fluctuations in the atmospheric surface layer have been performed at several places around the world and a summary of the main results is provided by Panofsky and Dutton [21]. It follows that, in the scope of this work, the standard ratios of turbulence of the atmospheric surface layer can be assumed equal to:

$$\frac{\sigma_v^\infty}{\sigma_u^\infty} \simeq 0.8 \quad \text{and} \quad \frac{\sigma_w^\infty}{\sigma_u^\infty} \simeq 0.5 \tag{1.8}$$

It is important to realize that, if isotropic turbulence is assumed, the ratios take unitary values and both definitions of the turbulence intensity, Eq. 1.6 and Eq. 1.7 are identical. In the atmospheric boundary layer, Crespo and Hernandez [18] relate the atmospheric turbulence intensity Ti_k^0 to the streamwise turbulence intensity Ti_u^0 by injecting Eq. 1.8 into Eq. 1.6:

$$\mathrm{Ti}_k^0 \simeq 0.8 \times \mathrm{Ti}_u^0 \quad \text{where} \quad \mathrm{Ti}_k^0 = \sqrt{\frac{2}{3}}\frac{\sqrt{k_\infty}}{U_\infty} \quad \text{and} \quad \mathrm{Ti}_u^0 = \frac{\sigma_u^\infty}{U_\infty}. \tag{1.9}$$

In this expression, the mean flow velocity U and the turbulent kinetic energy are the free stream quantities, U_∞ and k_∞. In the wake of a wind turbine, it is known that the flow is subjected to an increase of turbulence intensity due to the viscous rotor drag, the surface shear and the wake shear [22]. In this region, Crespo and Hernandez [18] propose to simply re-write Eq. 1.9 for the total level of turbulence intensity as:

$$\mathrm{Ti}_k \simeq 0.8 \times \mathrm{Ti}_u \quad \text{where} \quad \mathrm{Ti}_k = \sqrt{\frac{2}{3}}\frac{\sqrt{k}}{U_\infty} \quad \text{and} \quad \mathrm{Ti}_u = \frac{\sigma_u}{U_\infty}, \tag{1.10}$$

in which the mean flow velocity is assumed equal to the free stream velocity U_∞. Note that in Eq. 1.10, the relation between Ti_k and Ti_u implicitly assumes that Eq. 1.8 remains valid in the wake, *i.e.* that the turbulence anisotropies in the wake and in the atmospheric boundary layer are similar. In the literature, two main definitions of the added turbulence intensity can be found:

$$\Delta\mathrm{Ti}_k = \sqrt{\frac{2}{3}}\,\frac{\sqrt{k}-\sqrt{k_\infty}}{U_\infty} = \mathrm{Ti}_k - \mathrm{Ti}_k^0 \tag{1.11}$$

and

$$\Delta\mathrm{Ti}_k = \sqrt{\frac{2}{3}}\,\frac{\sqrt{k-k_\infty}}{U_\infty} = \sqrt{(\mathrm{Ti}_k)^2 - (\mathrm{Ti}_k^0)^2}, \tag{1.12}$$

in which $\Delta\mathrm{Ti}_u \simeq \Delta\mathrm{Ti}_k/0.8$ directly results from Eq. 1.10. While Eq. 1.11 has the advantage of remaining defined even for $k < k_\infty$, Eq. 1.12 stems from the physical hypothesis that the turbulent kinetic energy Δk produced at the rotor adds up to that of the ambient flow:

$$k = \Delta k + k_\infty. \tag{1.13}$$

This assumption, introduced by Crespo and Hernandez [18], is wildly used in the literature, as in Larsen [22], Frandsen [11], Xie and Archer [23], Qian and Ishihara [24], Tian et al. [25] and Lingkan and Buxton [19]. In all these works, Eq. 1.12 is preferred over Eq. 1.11 to define the added turbulence intensity in the wake.

In Crespo and Hernandez [18], the equations of conservation of momentum and of the turbulent kinetic energy are simplified under a set of assumptions and solved for the maximum value of Δk in the wake. Using the definition Eq. 1.12, the maximum level of streamwise added turbulence intensity writes:

$$\Delta\mathrm{Ti}_{u,max} = 0.362\,(1-(1-C_T)^{0.5}). \tag{1.14}$$

This expression is expected to be verified in the near wake only, *i.e.* where the turbulent dissipation is negligible compared to the production of turbulent kinetic energy. In the far wake region, Crespo and Hernandez [18] calibrate the coefficients of an empirical expression against the results of RANS simulations and obtain:

$$\Delta\mathrm{Ti}_{u,max} = 0.73\,a^{0.8325}\,(\mathrm{Ti}_u^0)^{-0.0325}\,\tilde{x}^{-0.32}, \tag{1.15}$$

in which the subscript max refers to the maximum over a crosswind section at a distance x behind the rotor. In Eq. 1.15, $\tilde{x}$ denotes the normalized downstream distance x/D and $a = 1-(1-C_T)^{0.5}$ is the induction factor. Overall, Crespo and Hernandez [18] show acceptable results of both Eq. 1.14 and Eq. 1.15.

Later, Larsen [22] suggests, without further detail, to use the Bernoulli representation of an idealized rotor together with a Boussinesq-K model [26] and the additive kinetic energy assumption (Eq. 1.13). The resulting expression for $\Delta\mathrm{Ti}_{u,max}$ reads:

$$\Delta\mathrm{Ti}_{u,max} = 0.29\,\tilde{x}^{-1/3}\sqrt{1-\sqrt{1-C_T}}. \tag{1.16}$$

It can be noted that both Eq. 1.15 and Eq. 1.16 predict approximately the same evolution with respect to the downstream distance.

In Frandsen [11], the determination of a conservative added turbulence intensity model is tackled in view of improving the modelling of the loading on the blades. The expression proposed by Frandsen [11] involves two coefficients, the calibration of which is carried out based on full-scale measurements at $C_T \simeq 0.7$, and writes:

$$\Delta \mathrm{Ti}_{u,max} = \frac{1}{1.5 + 0.8\,\tilde{x}\,C_T^{-0.5}}. \tag{1.17}$$

Moreover, it is shown and discussed in Lingkan and Buxton [19] that the scaling $\Delta \mathrm{Ti}_{u,max} \sim \tilde{x}^{-1}$ used in Frandsen [11] offers the best agreement with respect to the wind tunnel measurements.

Based on an initial model proposed by Quarton [27], Xie and Archer [23] re-calibrate the expression using LES data generated for an incoming turbulence intensity level $\mathrm{Ti}_u^0 = 0.07$ over the range of conditions $C_T \in [0.37; 0.56]$. The final relationship for $\Delta \mathrm{Ti}_{u,max}$ involves the length of the near wake region, denoted x_n, as predicted by Vermeulen [28]:

$$\Delta \mathrm{Ti}_{u,max} = 5.7\,C_T^{0.5} (\mathrm{Ti}_u^0)^{0.68} \left(\frac{x}{x_n}\right)^{-0.96}. \tag{1.18}$$

In all the one-dimensional added turbulence intensity models introduced so far, the focus is on the maximum value over a crosswind section so that the distribution of the turbulence over this section is considered homogeneous. The only exception being Frandsen [11], in which a simple Gaussian profile, similar to that of the velocity deficit, is assumed. More recently, Qian and Ishihara [24] have developed a three-dimensional added turbulence intensity model based on the results of LES simulations. Over the set of conditions $C_T \in [0.35; 0.8]$ and $\mathrm{Ti}_u^0 \in [0.035; 0.137]$, Qian and Ishihara [24] first derive the relation

$$\Delta \mathrm{Ti}_{u,max} = \frac{1}{2.3\,C_T^{-1.2} + (\mathrm{Ti}_u^0)^{0.1}\tilde{x} + q}, \quad \text{where} \quad q = 0.7\,C_T^{-3.2} (\mathrm{Ti}_u^0)^{-0.45} (1+\tilde{x})^{-2}. \tag{1.19}$$

Attention should be paid to the fact Eq. 1.19 is expected to remain valid in both the near and far wakes, contrary to all the other models considered in the scope of this work. Then, an axisymmetric added turbulence intensity field is modelled using a two-term Gaussian function. Contrary to the simple Gaussian function used in Frandsen [11], a two-term Gaussian allows to represent the high levels of added turbulence generated at the rotor periphery. Moreover, this choice of modelling function appears to be strongly supported by the results of Lingkan and Buxton [19]. The final modelling step consists in correcting the axisymmetric profile so as to account for the dependence on the vertical position. Eventually, the model is shown to outperform the predictions of the Frandsen [11] model when compared to wind tunnel experimental measurements.

Inspired by the researches of Xie and Archer [23], Tian et al. [25] calibrate the following expression for the amplitude of the added turbulence intensity:

$$\Delta \mathrm{Ti}_{u,max} = \frac{\kappa}{2}\,C_T^{\kappa/4}\,(\mathrm{Ti}_u^0)^{-\kappa/8}\,\tilde{x}^{-\kappa}, \quad \text{with} \quad \kappa = 0.5 \tag{1.20}$$

against LES data. Following the procedure described in Qian and Ishihara [24], an axisymmetric profile is proposed. Unlike Qian and Ishihara [24], in which a two-term Gaussian function is considered, a dual-cosine shape function is used to model the profile of the added turbulence intensity. Finally, a vertical correction, similar to that applied in Qian and Ishihara [24] is added to the model. Overall, the model shows good performance, although no significant improvement with respect to the Qian and Ishihara [24] model is observed.

In Sec. 2.1.2 the predictions of all the models introduced in the current section are compared to the RANS data generated by EllipSys, with the aim of identifying potential candidates for the modelling of the RANS look-up table.

1.2.3 Superposition methods for wind farm flow modelling

In Sec. 1.2.1 and Sec. 1.2.2, the emphasis was placed on the modelling of the velocity deficit and the added turbulence intensity in the wake of a stand-alone turbine. As explained in Sec. 1.1, the single-wake models can then be combined using superposition methods to represent multiple-wake situations. For that reason, this section aims at providing a comprehensive overview of the existing superposition methods used to assess the effects, both in terms of velocity deficits and added turbulence intensities, of merged wakes in wind farms.

An non-exhaustive overview of the main current superposition methods is given in Tab. 1.1. In Tab. 1.1a, the total wake velocity U at a downstream position x is observed to depend on the velocity deficit $\Delta U_i(x)$ computed for each of the N upstream turbines. As specified in Zong [29], for each method in Tab. 1.1a, the velocity deficit ΔU_i can be either defined with respect to the inflow velocity of the wind farm, *i.e.*

$$\Delta U_i = U_\infty - u_w^i, \tag{1.21}$$

or with respect to the local inflow velocity u_0^i perceived by the ith turbine:

$$\Delta U_i = u_0^i - u_w^i. \tag{1.22}$$

In Eq. 1.21 and Eq. 1.22, u_w^i denotes the wake velocity of the ith turbine considered in a stand-alone configuration. It should be noted that a similar discussion holds for the increase of turbulence intensity $\Delta \mathrm{Ti}_{k,i}$. However, in order to limit the number of methods investigated in the scope of this project, only the definition of ΔU_i given by Eq. 1.22 is retained. Likewise, the local incoming turbulence intensity seen by the ith turbine is always used to compute the increment $\Delta \mathrm{Ti}_{k,i}$. The decision made to use the local inflow values as inputs to determine the characteristics of the next wake is essentially motivated by the physical intuition of the problem and follows the recommendations of Zong [29].

Although Machefaux et al. [30] and Lingkan and Buxton [19] point out that the superposition methods listed in Tab. 1.1 do not have any strong theoretical basis, physical interpretations of some of these methods have been proposed. For example, Lissaman [31] claims that the expression of method A in Tab. 1.1a, used together with the definition Eq. 1.21, can be seen as

Table 1.1: Non-exhaustive list of existing superposition methods for the velocity deficit (a) and the added turbulence intensity (b).

(a) Velocity deficit

Method	Rule
A	$U = U_\infty - \sum_i^N (\Delta U_i)$
B	$U = U_\infty - \sqrt{\sum_i^N (\Delta U_i)^2}$
C	$U = U_\infty - \max_i\{\Delta U_i\}$

(b) Added turbulence intensity

Method	Rule
A	$\mathrm{Ti}_k^w = \mathrm{Ti}_k^0 + \sum_i^N (\Delta \mathrm{Ti}_{k,i})$
B	$\mathrm{Ti}_k^w = \mathrm{Ti}_k^0 + \sqrt{\sum_i^N (\Delta \mathrm{Ti}_{k,i})^2}$
C	$\mathrm{Ti}_k^w = \mathrm{Ti}_k^0 + \max_i\{\Delta \mathrm{Ti}_{k,i}\}$
D	$\mathrm{Ti}_k^w = \sqrt{(\mathrm{Ti}_k^0)^2 + \sum_i^N (\Delta \mathrm{Ti}_{k,i})^2}$
E	$\mathrm{Ti}_k^w = \sqrt{(\mathrm{Ti}_k^0)^2 + (\Delta \mathrm{Ti}_{k,N})^2}$

a first order approximation of the momentum conservation equation. This method is however not recommended by Crespo et al. [32] who highlight the risk of predicting negative values of U. Katic et al. [6] then propose the relation given as method B in Tab. 1.1a, arguing that the mean kinetic energy can reasonably be assumed conserved in the wake. Later, Niayifar and Porté-Agel [17] and Voustinas et al. [33] respectively re-write methods A and B in Tab. 1.1a using the second definition for ΔU_i (Eq. 1.22). Eventually, Machefaux et al. [30] introduce method C in Tab. 1.1a, following from the assumption that only the largest velocity deficit has an impact in the merged wake.

In Tab. 1.1b, methods A, B and C are simply proposed by analogy to the deficit methods in Tab. 1.1. Moreover, method D can be seen as the generalization of Eq. 1.12 to a multiple-turbine configuration. On a relevant note, it can be recalled that in Sec. 1.2.2, Eq. 1.12 has been shown to stem from the assumption that the turbulent kinetic energy is an additive quantity. In Lingkan and Buxton [19], method D and B (Tab. 1.1b) are investigated and lead to close and consistent results for small spacings between the porous disks. Finally, in method E, only the effect of the most upstream turbine is accounted for. Note that the results from Lingkan and Buxton [19] suggest the use of method E only in case of larger spacings in the wind farm.

1.3 The PyWakeEllipSys software

The software used to generate the RANS look-up table model introduced in Sec. 1.1 is the PyWakeEllipSys in-house flow solver of DTU Wind and Energy Systems [2], referred to as EllipSys in the rest of this work. It consists of a plug-in to PyWake, with which the Reynolds-averaged Navier-Stokes equations can be solved for a wind farm, without the need for any engineering models. The characteristic features of this software are briefly described, emphasizing the choices made when generating the RANS look-up table.

In EllipSys, the forces exerted by the turbine on the flow are represented by an actuator disk model over a local polar grid. A total of twenty-two different actuator disk models of various fidelity levels is featured. Among other characteristics, an atmospheric surface layer model was applied at the inflow boundary and the wake rotation effects were accounted for when building the RANS look-up table. Moreover, the local rotor grid is mapped onto a cartesian grid covering the entire domain, the spacing of which increases with distance from the turbine. In addition, EllipSys offers different closure model of the RANS equations. In the case of interest, the k-ε-f_P model proposed by van der Laan et al. [34] was employed. This model relies on the expression of the Reynolds stress $\overline{u_i' u_j'}$ provided by the classical Boussinesq hypothesis,

$$\overline{u_i' u_j'} = \frac{2}{3} k \, \delta_{ij} - 2 \, \nu_T S_{ij}, \quad \text{with} \quad S_{ij} = \frac{1}{2} \left(\frac{\partial \overline{u_i}}{\partial x_j} + \frac{\partial \overline{u_j}}{\partial x_i} \right), \tag{1.23}$$

where ν_T is the eddy viscosity and $\overline{u_i}$ is the i component of the mean flow velocity. A modified version of the popular k-ε closure is introduced, in which the additional parameter f_P allows to limit the impact of ν_T in the regions of large velocity gradients, *i.e.* the near wake. This modification is particularly suitable for wind farm flow modelling as an over-estimation of the Reynolds stress leads to excessive values of the turbulence intensity, and therefore to too optimistic predictions of the wake recovery speed.

In the RANS look-up table model of the added turbulence intensity, for which alternative options are explored in this work, $\Delta \mathrm{Ti}_k$ is defined following Eq. 1.12. An important comment must however be addressed. Since the RANS look-up table model relies on the Boussinesq hypothesis (Eq. 1.23), the anisotropy in the wake cannot be well accounted for. For that reason, the results of EllipSys, identified by "$RANS$", verify the following identities

$$\mathrm{Ti}_{k,max}^{RANS}(x) \simeq \mathrm{Ti}_{u,max}^{RANS}(x) \quad \text{and} \quad \mathrm{Ti}_{k,avg}^{RANS}(x) \simeq \mathrm{Ti}_{u,avg}^{RANS}(x). \tag{1.24}$$

In these expressions, the subscripts max and avg respectively denote the maximum and the average over a rotor section at position x. It can be concluded that a wake modelled with the RANS look-up table approach is always implicitly assumed isotropic. It should however be emphasized that, upstream of a stand-alone turbine, the standard ratios of turbulence of the atmospheric surface layer (Eq. 1.8) remain valid, *i.e.* $\mathrm{Ti}_k^0 \simeq 0.8 \times \mathrm{Ti}_u^0$.

Before going any further, it is worth pointing out that, although RANS data are used as a reference for calibrating a new engineering wake model, they are intrinsically flawed. A comparison between the LES predictions generated by van der Laan [1] for the NREL-5MW rotor and the corresponding RANS data ($\mathrm{Ti}_k^0 = 0.04$) is shown in Fig. 1.2a and Fig. 1.2b. The isotropic behavior of the RANS quantities can be observed by comparing the evolution of $\mathrm{Ti}_{u,max}^{RANS}$ (Fig. 1.2a) and $\mathrm{Ti}_{k,max}^{RANS}$ (Fig. 1.2b). As expected from Eq. 1.24, the RANS predictions do not show any clear distinction between Ti_k and Ti_u. By contrast, the LES results depict a strong increase of the maximum streamwise added turbulence intensity in the near wake. Although the RANS predictions show better agreement with the LES data for Ti_k than for Ti_u, the RANS results are seen to significantly under- then over- predict the LES predictions as x increases (Fig. 1.2b). In view of the significant differences observed, it's worth pointing

out that the methodology developed in the following sections is not intrinsically linked to the RANS data from the look-up table. In other words, the new model developed in this work could easily be re-calibrated against an LES database.

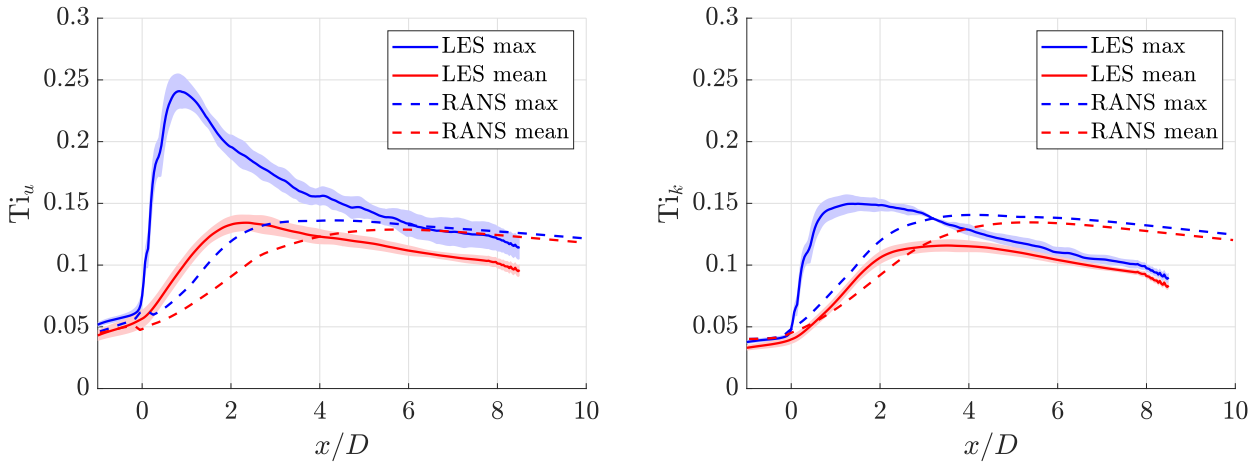

(a) Ti$_u$ (b) Ti$_k$

Figure 1.2: Comparison of the LES and RANS predictions of the total level of turbulence intensity in the wake. The maximum and rotor average values are shown for Ti_u (a) and Ti_k (b). A 95% confidence interval is added the LES curves.

1.4 Thesis outline

As introduced in Sec. 1.1, the main objective of this work is to provide a reliable and memory-efficient alternative to the single-wake RANS look-up table model. To do so, Chapter 2 tackles the determination of a one-dimensional single-wake model for the added turbulence intensity. A first approach, informed by a comparative analysis of the existing models, is developed on the basis of theoretical considerations. Three different models for the amplitude, or maximum, of the added turbulence intensity, $\Delta\text{Ti}_{k,max}$, are investigated. A second approach is then considered for the development of a fourth model.

In Chapter 3, the focus is placed on the multi-dimensional generalization of the new one-dimensional single-wake model. In order to derive a comprehensive wake model capable of reliably substituting the RANS look-up table, the added turbulence intensity model is supplemented by a two-dimensional single-wake velocity deficit model. Since the main focus of this work is not on improving velocity deficit models, a recently developed model is selected and re-calibrated against the RANS data.

Eventually, the analysis carried out in Chapter 4 allows to assess the performance of the new comprehensive wake model in a multiple-wake configuration. To achieve this, the new model is implemented in the PyWake software [9]. Besides discussing whether or not the RANS look-up

table model can effectively be replaced by the new wake model, the superposition methods themselves are analysed. In particular, emphasis is placed on the inherent link between the selected definition of $\Delta \mathrm{Ti}_k$ (Eq. 1.11 or Eq. 1.12) and the suitable superposition methods.

Chapter 2

Single wake modeling: Determination of a new model for the amplitude of the wake added turbulence intensity

2.1 Preliminary study

2.1.1 Theoretical considerations

This first step towards the development of a new added turbulence intensity model consists in an analytical approach that aims at determining the scaling of the turbulence intensity added by the presence of a wind turbine. The current section relies on various assumptions and is therefore only intended to provide a theoretically-grounded starting point for the development of a more complete model. It should be emphasized that the following discussion is widely inspired from the work of Scott et al. [35], in which a theoretical model of the eddy viscosity is investigated. The main idea proposed by Scott et al. [35] is to write the total Reynolds stress in the wake flow, $\overline{u_i' u_j'}$, as:

$$\overline{u_i' u_j'} = \overline{u_i' u_j'}\Big|_\infty + \Delta\overline{u_i' u_j'} \tag{2.1}$$

where $\Delta\overline{u_i' u_j'}$ denotes the increment of Reynolds stress caused by the presence of the turbine and $\overline{u_i' u_j'}\Big|_\infty$ refers to the background Reynolds stress, assumed equal to the atmospheric Reynolds stress in the scope of this work. Applying the Boussinesq hypothesis to the background flow, the corresponding Reynolds stress read

$$\overline{u_i' u_j'}\Big|_\infty = \frac{2}{3} k_\infty \delta_{ij} - 2\,\nu_T^\infty S_{ij}\Big|_\infty, \tag{2.2}$$

where ν_T^∞ is the atmospheric eddy viscosity. Injecting 2.2 into Eq. 2.1 and using Eq. 1.23 for $\overline{u_i' u_j'}$, the following expression can be derived

$$\Delta\overline{u_i' u_j'} = \frac{2}{3}\Delta k\,\delta_{ij} - 2\,(\nu_T\,S_{ij} - \nu_T^\infty\,S_{ij}\Big|_\infty). \tag{2.3}$$

In this expression, the difference between the atmospheric and the wake flow turbulent kinetic energies explicitly appears and is therefore substituted by Δk (Eq. 1.13). This shows that, as could have been expected, the decomposition introduced by Scott et al. [35] is intrinsically linked to the assumption that the turbulent kinetic energy is additive, Eq. 1.13. By analogy to the cononical form of the Boussinesq hypothesis, Scott et al. [35] define an increment of eddy viscosity, $\Delta\nu_T$, as:

$$\Delta\nu_T \left(S_{ij} - S_{ij}\Big|_\infty\right) = \nu_T\, S_{ij} - \nu_T^\infty\, S_{ij}\Big|_\infty, \tag{2.4}$$

so that Eq. 2.3 re-writes

$$\Delta\overline{u_i' u_j'} = \frac{2}{3}\,\Delta k\,\delta_{ij} - 2\,\Delta\nu_T \left(S_{ij} - S_{ij}\Big|_\infty\right). \tag{2.5}$$

In Scott et al. [35], LES simulations of the flow with and without the turbine are performed and processed to retrieve the values of $\Delta\nu_T$ from Eq. 2.5 at any downstream position.

Moreover, in Davidson [36] a scaling of the eddy viscosity is obtained, based on dimensional analysis:

$$\nu_T \sim \sqrt{k}\, l_c, \tag{2.6}$$

where l_c is the characteristic size of the large eddies in the flow. In light of this expression and following from the assumption of additive turbulent energy (Eq. 1.13), it is proposed to assume that the added eddy viscosity $\Delta\nu_T$ (Eq. 2.4) scales as:

$$\Delta\nu_T \sim \sqrt{\Delta k}\, l_c. \tag{2.7}$$

As a result, Eq. 1.12 can be re-written as:

$$\Delta\mathrm{Ti}_k \sim \sqrt{\frac{2}{3}}\,\frac{\Delta\nu_T}{U_\infty\, l_c}. \tag{2.8}$$

In this last expression, a key element to keep in mind is that the characteristic size l_c of the eddies is unknown but expected to decrease with increasing downstream distance. In addition, Eq. 2.8 is presumed valid at any distance from the rotor, since no near or far wake specific assumptions have been made. The aim of the rest of this section is therefore to particularize this equation according to the region considered in the wake.

At large downstream distances, the main assumption widely made in the literature is that the wake profile is self-similar. Considering, in addition, that the wake is axisymmetric, Durbin and Pettersson [37] obtain the following scaling for the center-line velocity deficit $\Delta U_{CL}(x)$ and the wake diameter $\delta(x)$:

$$\Delta U_{CL} \sim x^{-2/3} \quad \text{and} \quad \delta(x) \sim x^{1/3}. \tag{2.9}$$

Although the experimental research studies carried out by Lingkan and Buxton [19] point out that Eq. 2.9 leads to discrepancies for both $\delta(x)$ and $\Delta U_{CL}(x)$, the scaling proposed by Durbin and Pettersson [37] is retained in the scope of this work. From Eq. 2.9, Durbin and Pettersson [37] predict that the eddy viscosity should evolve as:

$$\nu_T \sim x^{-1/3}. \tag{2.10}$$

Moreover, in the development of Scott et al. [35], the background, *i.e.* atmospheric, flow is assumed fully developed so that $S_{ij}\Big|_{\infty}$ and ν_T^{∞} do not depend on the downstream position. Therefore, from Eq. 2.4 it follows that:

$$\Delta\nu_T \sim \nu_T \sim x^{-1/3}. \tag{2.11}$$

Injecting this last relation in Eq. 2.8, it can be concluded that the added turbulence intensity in the far wake evolves as:

$$\Delta\mathrm{Ti}_k \sim \sqrt{\frac{2}{3}}\frac{x^{-1/3}}{U_\infty\, l_c}. \tag{2.12}$$

By contrast to the self-similar wake profile observed in the far wake, the near wake is essentially a foot print of the blade thrust force distribution, which leads to a non-self-similar shape, often approximated by a top hat profile. For that reason, an alternative to the work of Durbin and Pettersson [37] must be considered. While the self-similarity assumption is not valid in the near wake region, the viscous dissipation is expected to be negligible compared to the production of turbulent kinetic energy. Consequently, the steady dissipation-free transport equation for the turbulent kinetic energy has been re-written as a transport equation for Δk, under the assumption that the inflow turbulent kinetic energy k_∞ is independent of x. All the attempts made to solve this equation however proved unsuccessful. Hence, the decision was made to simply inject the expression obtained by Scott et al. [35] for the added eddy viscosity $\Delta\nu_T$ into Eq. 2.8. The resulting equation for $\Delta\mathrm{Ti}_k$ reads:

$$\Delta\mathrm{Ti}_k = \sqrt{\frac{2}{3}}\frac{A\, f(\tilde{x})}{U_\infty, l_c} \quad \text{with} \quad f(\tilde{x}) = \frac{\tilde{x}}{\sigma^2}\exp\left(\frac{-\tilde{x}^2}{2\sigma^2}\right), \tag{2.13}$$

where $\tilde{x} = x/D$, $\sigma = \tilde{x}_{max}$ is the relative position at which $\Delta\nu_T$ is maximum and A is a parameter to be defined.

2.1.2 Comparative study of the existing added turbulence intensity models

In this section, the focus is on the comparison of the existing models for the maximum of the added turbulence intensity, $\Delta\mathrm{Ti}_{k,max}$, with the RANS predictions of the EllipSys software, $\mathrm{Ti}_{k,max}^{RANS}$. Through this analysis, two main objectives are addressed. First, it is interesting to identify which existing models give the best approximation of the data, the underlying idea being to determine the key characteristics for the design of the new model. Then, this section also aims to provide evidence for the validation of the scalings, Eq. 2.12 and Eq. 2.13, obtained for $\Delta\mathrm{Ti}_k$ in Sec. 2.1.1. It should be pointed out that the distinction made in Sec. 1.2.2 between the definitions of $\Delta\mathrm{Ti}_{u,max}$ and $\Delta\mathrm{Ti}_{k,max}$ is no longer relevant in this analysis, given the isotropic nature (Eq. 1.24) of the reference data, $\Delta\mathrm{Ti}_{k,max}^{RANS}$. For that reason, the output of each added turbulence model listed in Sec. 1.2.2 is denoted $\Delta\mathrm{Ti}_{k,max}$ for consistency. In order to qualitatively assess the performances of these models, a relative cumulative error ε can be defined as:

$$\varepsilon = \frac{\int_{\tilde{x}_0}^{\tilde{x}_f} |\Delta\mathrm{Ti}_{k,max}^{RANS} - \Delta\mathrm{Ti}_{k,max}|\, d\tilde{x}}{\int_{\tilde{x}_0}^{\tilde{x}_f} \Delta\mathrm{Ti}_{k,max}^{RANS}\, d\tilde{x}}. \tag{2.14}$$

In Eq. 2.14, the boundaries $\tilde{x}_0$ and $\tilde{x}_f$ define the range of downstream distance over which the relative error ε is computed. The upper limit $\tilde{x}_f$ is set at the furthest position available in the RANS look-up table. In order not to excessively penalize models that are not defined in $tildex = 0$, the lower limit is arbitrarily set at 50 m behind the rotor. One could, however, repeat this analysis starting a few diameters away from the rotor, arguing that the focus should be placed on the region in which another turbine is likely to be located.

For the sake of completeness, the modelled values, $\Delta\mathrm{Ti}_{k,max}$, are compared to their RANS counterparts, $\Delta\mathrm{Ti}_{k,max}^{RANS}$, over a large variety of conditions. Indeed, three values of the atmospheric turbulence intensity are considered, *i.e.*, $\mathrm{Ti}_k^0 = 0.05$, $\mathrm{Ti}_k^0 = 0.15$ and $\mathrm{Ti}_k^0 = 0.30$, together with three different thrust coefficients, *i.e.*, $C_T = 0.1$, $C_T = 0.4$, $C_T = 0.8$). Only the case $\mathrm{Ti}_k^0 = 0.05$ is depicted hereafter, the two others being shown in App. 5.2. The effect of the downstream distance on the added turbulence intensity is highlighted in Fig. 2.1, Fig. 5.1 (App. 5.2) and Fig. 5.3 (App. 5.2), for which physical interpretations are discussed. Note that, in order to facilitate the comparison of the $\Delta\mathrm{Ti}_{k,max}$ curves for different C_T values, the values are normalized by the absolute RANS maximum $\Delta\mathrm{Ti}_{k,max}^{RANS}$, *i.e.* the peak value of $\Delta\mathrm{Ti}_{k,max}^{RANS}$ over the downstream distance. Besides that, the relative cumulative error ε defined in Sec. 2.1.2 and represented in Fig. 2.2, Fig. 5.2 (App. 5.2) and Fig. 5.4 (App. 5.2) allows a clear comparison of the fidelity of the tested models.

From Fig. 2.1, a few observations of the RANS predictions can be made and discussed in parallel with physical interpretations. First, a strong increase of $\Delta\mathrm{Ti}_{k,max}^{RANS}$ can be seen in the near wake region, followed by a smooth decay in the far wake, the magnitude of which is determined by the value of the C_T coefficient. At short distances from the rotor, the strong large-scale velocity gradients involve a large production of turbulent kinetic energy, resulting in the sudden increase of $\Delta\mathrm{Ti}_{k,max}^{RANS}$. Note that this significant growth is in line with the Rayleigh function suggested by Scott et al [35] (Eq. 2.13). It should be emphasized that the turbulent kinetic energy (TKE) is not produced, strictly speaking, but converted from the kinetic energy of the surrounding flow. As the downstream distance increases, the eddy viscosity enhances the momentum diffusion from the surrounding flow towards the wake so that the velocity deficit starts to recover. This results in lower velocity gradients and therefore less turbulent kinetic energy generation. Hence, the evolution of $\Delta\mathrm{Ti}_{k,max}^{RANS}$ flattens, as shown in Fig. 2.1. Simultaneously, the turbulent kinetic energy is transferred from the large eddies to smaller scales, following the Kolmogorov's theory. At some downstream distance in the wake, the viscous dissipation becomes non-negligible compared to the production of TKE. This position seems to be $\tilde{x} \simeq 5$ for $C_T = 0.8$, as shown in Fig. 2.1 for $C_T = 0.8$. Contrary to wall turbulence, for which Durbin [37] identifies that the ratio of the production and the dissipation rates is approximately equal to 0.9, the exact value of this ratio in the far wake of a turbine appears to be function of both the thrust coefficients and the inflow turbulence intensity. Similarly, the peak value $\Delta\mathrm{Ti}_{k,absmax}^{RANS}$ and the position $\tilde{x}_{max}$ at which it is reached is observed to evolve with C_T and Ti_k^0. From Fig. 2.1, Fig. 5.1 (App. 5.2) and Fig. 5.3 (App. 5.2), it appears that $\Delta\mathrm{Ti}_{k,max}^{RANS}$ is essentially an increasing function of C_T. In the same figures, the position $\tilde{x}_{max}$ is seen to approach the rotor when C_T and/or Ti_k^0 increase. This phenomenon is discussed in more details in Sec. 2.3.1 and Sec. 2.4.1.

In the rest of this section, particular attention is paid to the Larsen (Eq. 1.16), Ishihara (Eq. 1.19) and Crespo (Eq. 1.15) models. As a matter of fact, the results provided by the Frandsen (Eq. 1.17), Xie & Archer (Eq. 1.18) and Tian (Eq. 1.20) models in Fig. 2.2, Fig. 5.2 (App. 5.2) and Fig. 5.4 (App. 5.2) often show large discrepancies with respect to the RANS data and are therefore not further discussed for the sake of brevity. Despite the small relative error obtained with the first model proposed by Crespo and Hernandez [18] (Eq. 1.14) at $C_T = 0.1$, more realistic values of the thrust coefficient lead to significantly larger errors. For that reason, the Crespo model of the near wake region is not retained as a promising candidate for possible improvements of the added turbulence intensity modeling. However, the far wake model developed by Crespo and Hernandez [18] (Eq. 1.15) matches the far wake behavior of the predicted RANS data $\Delta \mathrm{Ti}_{k,max}^{RANS}$ with high fidelity, as seen in Fig. 2.1. This observation is of particular interest as it supports the theoretical scaling, Eq. 2.12, derived in Sec. 2.1.1. Indeed, both Eq. 2.12 and the Crespo model (Eq. 1.15), for which good agreement is shown in Fig. 2.1, predict an evolution $\Delta \mathrm{Ti}_{k,max} \sim x^{-1/3}$ in the far wake.

Moreover, in Fig. 2.1, Fig. 5.2 (App. 5.2) and Fig. 5.4 (App. 5.2), the principal asset of the relation proposed by Qian and Ishihara [24] (Eq. 1.19), *i.e.* the near wake modelling, can be observed. Provided that the turbine operates at $C_T > 0.1$, this model indeed features a close estimation of the RANS data in the near wake region. In Fig.2.2, Fig. 5.2(App. 5.2) and Fig. 5.4(App. 5.2), the resulting relative cumulative error appears to be strongly limited, showing evidence of the need for a reliable near wake model. By comparison to the other models, the expression proposed by Larsen [22] (Eq. 1.16) seems to provide the most robust estimation of the added turbulence intensity under various C_T and Ti_k^0 conditions. The model indeed performs well at predicting the C_T dependence as very little variation of the relative error (Eq. 2.14) is observed in Fig. 2.2, Fig. 5.2 and Fig. 5.4 for values of $C_T > 0.1$. Furthermore, it should be noted that the evolution of the added turbulence intensity with the downstream distance, as predicted by Larsen, is the same as that obtained analytically in Sec. 2.1.1, Eq. 2.12. In Fig. 2.1, Fig. 5.1 (App. 5.2) and Fig. 5.3 (App. 5.2), the model matches the far wake behavior of the RANS data with great fidelity.

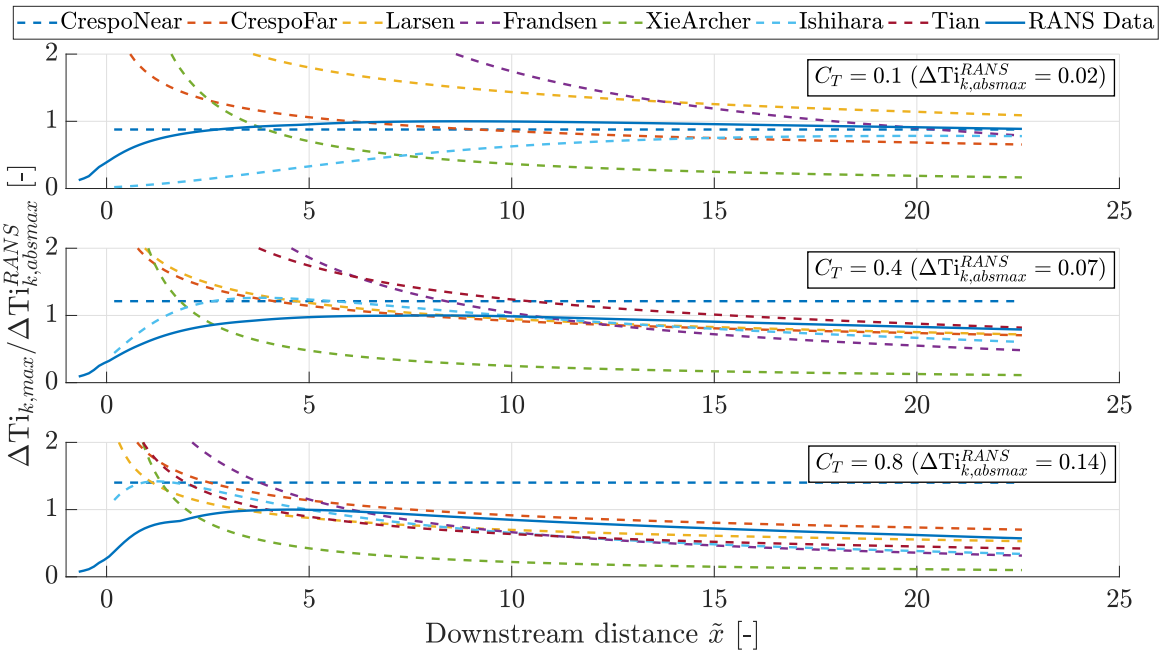

Figure 2.1: Comparison of $\Delta \mathrm{T}_{k,max}(x/D)$ as computed by the RANS simulations and as predicted by the existing models for $\mathrm{Ti}_0^k = 0.05$ and different values of C_T. Data are normalized by the maximal value of the RANS added turbulence intensity over the 3D domain ($\Delta \mathrm{Ti}^{RANS}_{k,absmax}$).

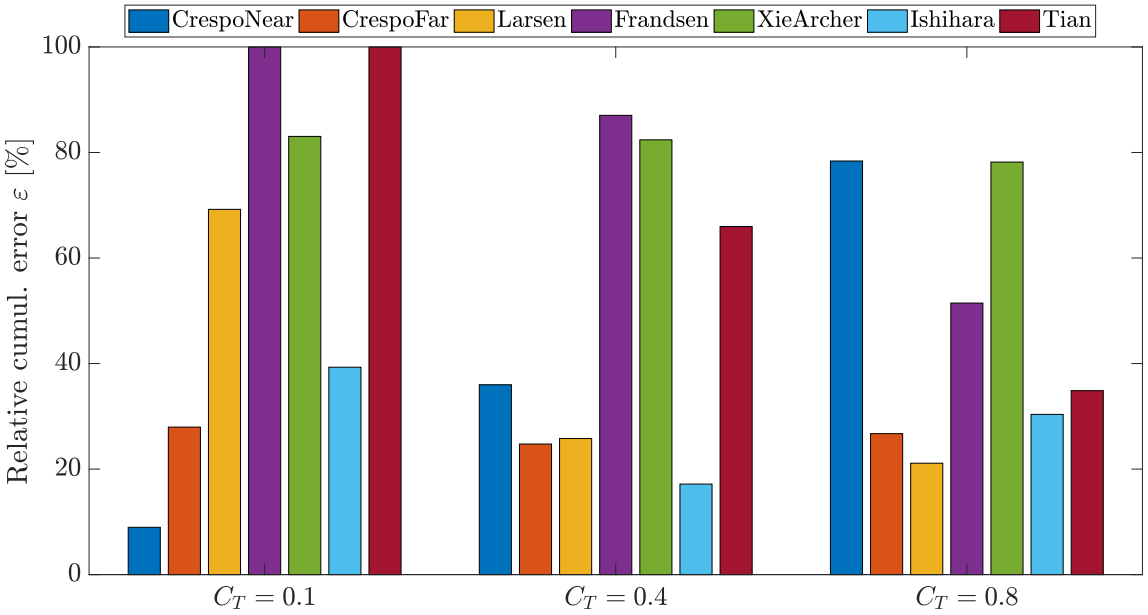

Figure 2.2: Comparison of the relative cumulative error ε (Eq. 2.14) for each existing model under $\mathrm{Ti}_0^k = 0.05$ and different C_T conditions.

The analysis carried out in this section first allows a better understanding of the wake recovery process. Among all the tested expressions, mainly those which tend to give the closest results to the RANS data for a wide variety of C_T and Ti_k^0 are discussed. Both the Larsen and the Crespo models, Eq. 1.16 and Eq. 1.15 suggest that $\Delta\mathrm{Ti}_{k,max}$ decreases as $x^{-1/3}$ downstream, hence supporting the theoretical prediction of Sec. 2.1.1. In light of the performance of the Ishihara model (Eq. 1.19), it can be concluded that a faithful representation of the near wake allows to drastically reduce the relative cumulative error ε. At this stage, it is therefore difficult to determine which of the two proposed theoretical scalings, Eq. 2.12 and Eq. 2.13, would be best suited to describe the evolution with x of added turbulence intensity in the wake.

2.2 Development of a first approach for the design of a new added turbulence intensity model

2.2.1 Methodology

In order to account for the downstream evolution of $\Delta\mathrm{Ti}_{k,max}$ in both the far and the near wake regions, the scaling (Eq. 2.13) derived from the work of Scott et al. [35] is used as a first starting point for the development of the new $\Delta\mathrm{Ti}_{k,max}$ model. In Eq. 2.13, the expression of A parameter is has to be determined. To do so, Scott et al [35] suggest to use the radius R of the rotor as a representative length scale, together with the expression of the wake velocity

$$U = U_\infty \sqrt{1 - C_T} \tag{2.15}$$

proposed by Bastankhah and Porté-Agel [38]. Using dimensional analysis, Scott et al [35] obtain that $A = RU/2$. The choice of this velocity scale however seems unsuitable to describe the turbulence intensity as it predicts negligible values of $\Delta\ \mathrm{Ti}_{k,max}$ when the turbine operates at high thrust coefficients. Therefore, the velocity deficit derived from Eq. 2.15,

$$\Delta U = U_\infty - U = U_\infty \left(1 - \sqrt{1 - C_T}\right), \tag{2.16}$$

is expected to be a better candidate for the velocity scale. It follows the expression of the corresponding scaling factor A:

$$A = \frac{R\, U_\infty \left(1 - \sqrt{1 - C_T}\right)}{2} \tag{2.17}$$

Injecting A (Eq. 2.17) into Eq. 2.13 allows to write:

$$\Delta\mathrm{Ti}_{k,max} = \alpha \left(1 - \sqrt{1 - C_T}\right) \frac{\tilde{x}}{\sigma^2} \exp\left(\frac{-\tilde{x}^2}{2\sigma^2}\right), \tag{2.18}$$

where α is function of Ti_k^0 and is a scaling parameter of the problem that is to be determined. It is important to mention that Eq. 2.18 is obtained assuming that the characteristic size of the large eddies, l_c in Eq. 2.8, can be taken equal to the rotor radius. Based on some observations, the model as defined by Eq. 2.18 appears to under-predict the values of $\Delta\mathrm{Ti}_{k,max}$ computed

for low thrust coefficients. Inspired by the analysis carried out in Sec. 2.1.2, and in particular by the good results of the physics-based Larsen model (Eq. 1.16) under different C_T values (Fig. 2.1), it is proposed to replace the A/l_c term in Eq. 2.13 by a $\Phi(C_T)$ fucntion, so that Eq. 2.13 re-writes

$$\Delta \mathrm{Ti}_{k,max} = \alpha\, \Phi\, \frac{\tilde{x}}{\sigma^2} \exp\left(\frac{-\tilde{x}^2}{2\sigma^2}\right) \quad \text{with} \quad \Phi(C_T) = \sqrt{1-\sqrt{1-C_T}}, \tag{2.19}$$

where $\Phi(C_T)$ is the C_T dependent term. As a result, the relationship Eq. 2.19 is expected to model the variation of thrust coefficients with greater fidelity than Eq. 2.18.

Eventually, the Rayleigh function $f(\tilde{x})$ that models the impact of the downstream distance on $\Delta \mathrm{Ti}_{k,max}$ has a maximum value of amplitude $f(\tilde{x}=\sigma) = \sigma^{-1}\exp(-1/2)$ and can therefore be normalized as:

$$f_N(\tilde{x}) = f(\tilde{x})\,\sigma \exp\left(\frac{1}{2}\right) = \frac{\tilde{x}}{\sigma} \exp\left(\frac{\sigma^2-\tilde{x}^2}{2\sigma^2}\right). \tag{2.20}$$

Doing so, $f_N(\tilde{x})$ reaches a maximum value of unitary amplitude at $\tilde{x}=\sigma$. Similarly to what Scott et al. [35] suggest for $\Delta\nu_T$, the position σ of the maximum added turbulence intensity is taken equal to $\sigma = 5.5$. Note that further analysis of the exact position of σ is carried out in Sec. 2.3 and an empirical law is eventually proposed for σ. The resulting new model for the added turbulence intensity reads:

$$\boxed{\Delta \mathrm{Ti}_{k,max} = \alpha \sqrt{1-\sqrt{1-C_T}}\, \frac{\tilde{x}}{\sigma} \exp\left(\frac{\sigma^2-\tilde{x}^2}{2\sigma^2}\right), \quad \sigma = 5.5} \tag{2.21}$$

In this expression, the remaining parameter α is expected to be function of the atmospheric turbulence intensity Ti_k^0 only and can be determined in light of the available RANS data $\Delta \mathrm{Ti}_{k,max}^{RANS}$. First, the following relation is evaluated for any combination of the thrust coefficients and the downstream distances:

$$\alpha = \frac{\Delta \mathrm{Ti}_{k,max}^{RANS}(\tilde{x}, C_T, \mathrm{Ti}_k^0)}{\sqrt{1-\sqrt{1-C_T}}\,(\tilde{x}/\sigma)\,\exp\left(\frac{\sigma^2-\tilde{x}^2}{2\sigma^2}\right)} \tag{2.22}$$

The α parameter is then plotted against Ti_k^0 to highlight the existing relationship between both quantities. This procedure also allows to assess the reliability of the predictions of the new model (Eq. 2.21) proposed for different thrust coefficients and downstream distances. Greater fidelity is indeed achieved by the model for any $(C_T, \tilde{x})$ combinations for which no significant variations of α (Eq. 2.22) is observed. The corresponding results are shown and discussed in Sec. 2.2.2.

In addition, a slightly different model is proposed as an alternative to Eq. 2.21. As discussed earlier in Sec. 2.1.2, Fig. 2.1, Fig. 5.1 (App.5.2) and Fig. 5.3(App.5.2) showed a steep increase of added turbulence intensity in the near wake region, followed by a slow decrease for larger downstream distance. Although the normalized Rayleigh function used in the new model (Eq. 2.21) is expected to faithfully represent the near wake region, large discrepancies can be

anticipated further away from the rotor. The theoretical scaling Eq. 2.12, supported by the results of the Larsen [22] and the Crespo and Hernandez [18] models, therefore inspires a far wake version of Eq. 2.21, for which $f_N(\tilde{x}) = \tilde{x}^{-1/3}$. It follows:

$$\boxed{\Delta \mathrm{Ti}_{k,max} = \beta \sqrt{1 - \sqrt{1 - C_T}}\, \tilde{x}^{-1/3}} \tag{2.23}$$

Where β plays the same role as the α parameter in Eq. 2.21. It is interesting to notice that this expression reduces to Larsen model if β is taken equal to 0.29. As β is however foreseen to vary with Ti_k^0, the same procedure as for the determination of α is carried out. The scaling parameter β is computed as

$$\beta = \frac{\Delta \mathrm{Ti}_{k,max}^{RANS}(\tilde{x}, C_T, \mathrm{Ti}_k^0)}{\sqrt{1 - \sqrt{1 - C_T}}\, \tilde{x}^{-1/3}} \tag{2.24}$$

and then plotted against Ti_k^0. The results obtained for various combinations of C_T and $\tilde{x}$ are investigated in Sec. 2.2.2

2.2.2 Results

The results of the development carried out in Sec. 2.2.1 are shown and discussed. The analysis is limited to four values of C_T, spanning a large range of thrust coefficients. The impact of the downstream distance from the rotor is evaluated at representative values of x in the near and far wakes.

From Fig. 2.3, no clear trend is appearent in the very near wake or in the very far wake. In those regions, the normalized Rayleigh distribution $f_N(\tilde{x})$ fails to reasonably approximate the downstream distance dependence predicted by the RANS data. It is clear that for a data point α, computed for a given C_T and Ti_k^0, $f_N(\tilde{x})$ is found to be a good modelling of the downstream distance dependence if no significant variation of α is observed between the successive subplots of Fig. 2.3. The same conclusion holds for Fig. 2.4, in which $f_N(\tilde{x}) = \tilde{x}^{-1/3}$. In the first model, *i.e.*, Eq. 2.21, one should however bear in mind that the shape of $f_N(\tilde{x})$ strongly depends on the position of the maximum added turbulence intensity, taken equal $\sigma = 5.5$ in Sec. 2.2.1. This motivates the use of a more reliable σ value, as discussed in Sec. 2.3.

For distances $\tilde{x}$ between $2D$ and $8D$, the values of α computed by Eq. 2.22 gather around a clear trend (Fig. 2.3). By comparison to the first model, the data points β computed with the second relation (Eq. 2.23) and shown in Fig. 2.4 follow a similar trend over a larger range of downstream distances. Still, the noticeable evolution along x of this trend and of the data point distribution unveils some flaws in the way the x dependence is modeled by Eq. 2.23. On Fig. 2.4, one should however note that the discrepancies between β at $x = 12D$ and β at $x = 16D$ are significantly smaller than those between β at $x = 1D$ and β at $x = 4D$. This clearly shows evidence of the greater fidelity of model Eq. 2.23 in the far wake region.

In both Fig. 2.3 and Fig. 2.4, smaller spacing between the curves of constant C_T essentially reflects a greater fidelity of the C_T dependent term (*i.e.*, $\Phi(C_T)$) in the model. For larger values

of Ti_k^0, the vertical spacing between the data points computed for different C_T values is seen to decrease significantly. This observation is all the more obvious at large distances from the rotor. When varying the thrust coefficient, one can therefore conclude that the RANS data indeed evolve as "$\Phi(C_T) = \sqrt{1-\sqrt{1-C_T}}$", in the far wake or provided that the atmospheric turbulence intensity is large. Under this last condition, the turbulent mixing is enhanced, hence leading to a faster wake recovery. This seems to point out that the assumptions made by Larsen [22] to derive the C_T dependence $\Phi(C_T)$ are in line with the self-similarity assumption, the validity of which increases at large Ti_k^0 values and large x values. Moreover, it is important to recall that the quality of the predictions of the Larsen model [22] was observed to significantly decrease for $C_T < 0.4$ (Fig. 2.2). This can clearly be observed on Fig. 2.4 at downstream distances $x = 8D$, $x = 12D$ and $x = 16D$ as larger discrepancies, *i.e.* larger vertical spacings, occur for $C_T = 0.1$.

For values of the thrust coefficients larger than $C_T = 0.1$, Fig. 2.4 shows that the scaling coefficient β has a linearly decreasing dependence on Ti_k^0 for $x \geqslant 12D$. Physically, this results again seems to indicate that the remaining added turbulence intensity in the far wake is smaller for large atmospheric turbulence intensities (*i.e.*, rapid wake recovery). With regard to the near wake region, it is clear that the current model leads to non-negligible inaccuracies in that area. Still, a trend seems to emerge. Contrary to the very far wake, the scaling coefficients all observe a non linear growth with Ti_k^0 in the very near wake. In this area, it seems that an increase in the atmospheric turbulent intensity is associated with an increase in the added turbulent intensity. Depending on the downstream distance, the atmospheric turbulent intensity appears to either reinforce $\Delta\mathrm{Ti}_{k,max}$ (near wake) or to contribute to its decrease by favouring the wake recovery (far wake). For intermediate distances, the behavior of the calculated data points β lays in between the non-linear growth predicted in the very near wake and the linear decay obtained in the very far wake.

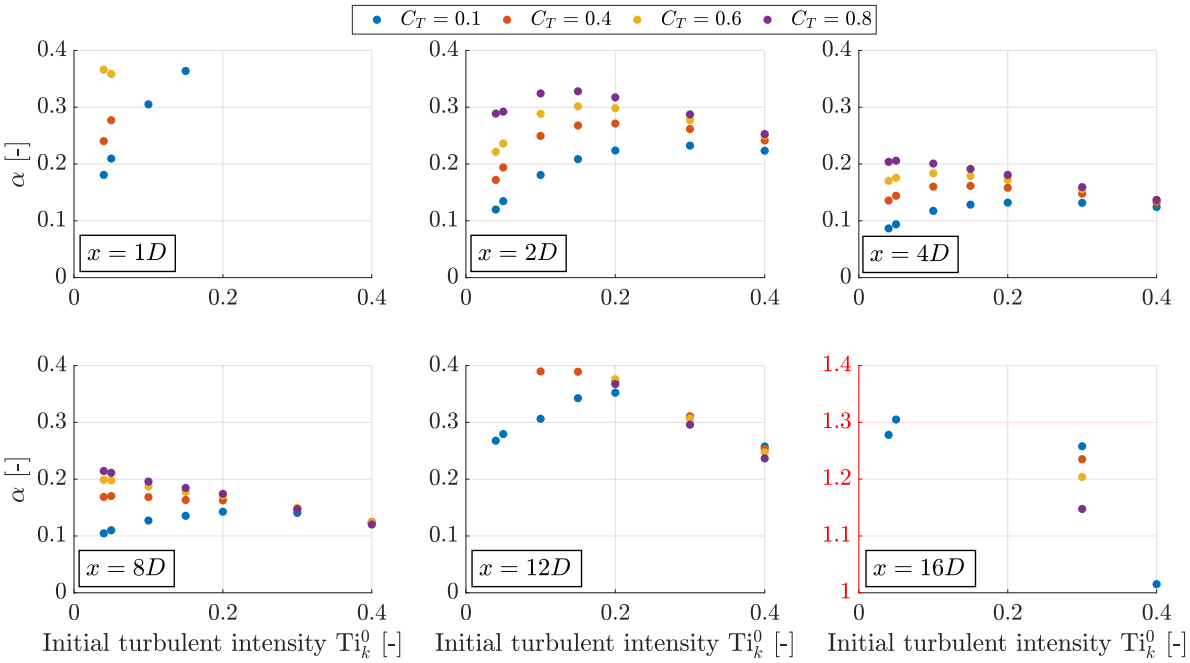

Figure 2.3: Evolution of the scaling parameter α as function of Ti_k^0. Data are computed with Eq. 2.22 for four different thrust coefficients, at six representative distances downstream. A unit offset is applied to the vertical axis of $x = 16D$ for readability.

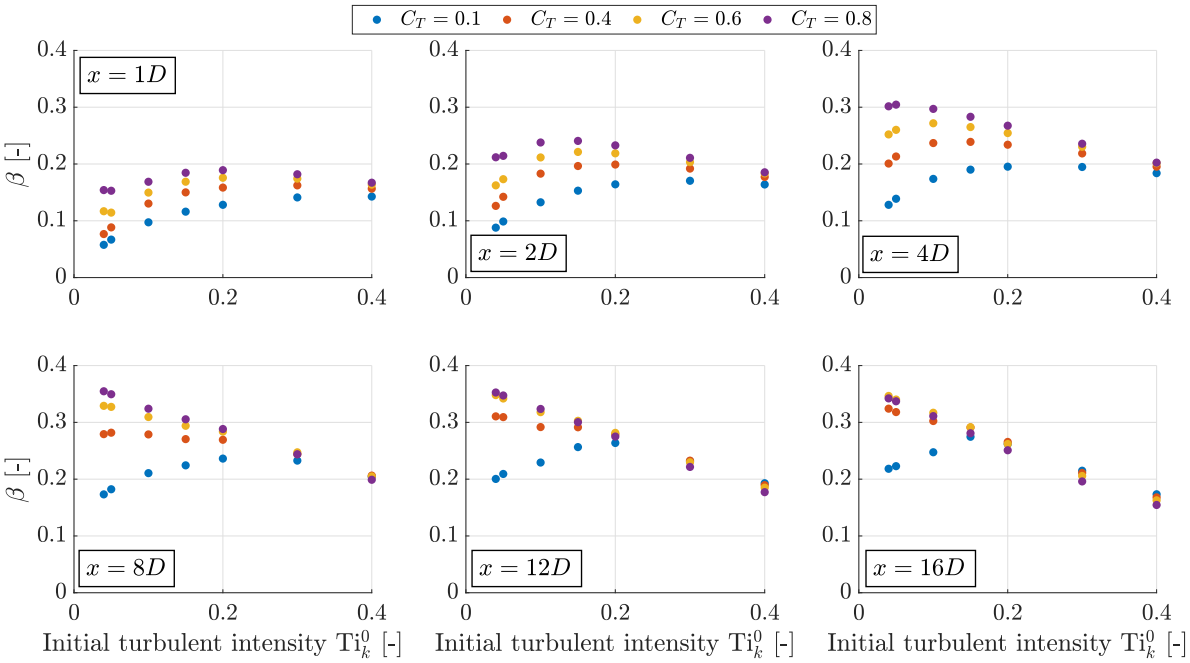

Figure 2.4: Evolution of the scaling parameter β as function of Ti_k^0. Data are computed with Eq. 2.24 for four different thrust coefficients, at six representative distances downstream.

As a conclusion, this section explicitely shows that the C_T dependence is overall well modeled by $\Phi(C_T)$, especially in situations for which the assumptions of self-similarity is valid. It appears that the model proposed by Eq. 2.21 is poorly correlated with the RANS data in the very near and very far wakes. The determination of an empirical law for the position $\tilde{x}_{max} = \sigma$ of the maximum added turbulence intensity is expected to significantly improve the fidelity of $f_N(\tilde{x})$ in the first model (Eq. 2.20). On the contrary, good agreement is exhibited for $f_N(\tilde{x}) = \tilde{x}^{-1/3}$ in the far wake region and for a sufficiently high thrust coefficient ($C_T > 0.1$). Given the results shown in Fig. 2.3 and Fig. 2.4, it is evident that no analytical expression of the form $\alpha(\mathrm{Ti}_k^0)$ and $\beta(\mathrm{Ti}_k^0)$ would provide an accurate modeling of these scaling parameters. The remaining dependence in the downstream distance and, to a lesser extent, in the thrust coefficient, motivates the investigation of alternative forms of the $\Phi(C_T)$ and $f_N(\tilde{x})$ functions.

2.3 Investigation of a possible improvement of the new turbulence added intensity model

2.3.1 Methodology

Based on the promising results of Sec. 2.2.1, the two tested models (Eq. 2.21 and Eq. 2.23) pave the way to the determination of a more sophisticated expression. The main idea behind this new model is to take advantage of the flexibility introduced by the σ parameter in Eq. 2.20 in order to approximate the downstream distance dependence $f_N(\tilde{x})$ with greater fidelity in the near wake. As previously mentioned, this requires an accurate estimation of the position $\sigma = \tilde{x}_{max}$ of the maximum added turbulence intensity $\Delta\mathrm{Ti}_{k,absmax}$ behind the rotor. First, it is worth recalling that the study of the existing $\Delta\mathrm{Ti}_k$ models carried out in Sec. 2.1.2 showed evidence of the impact of C_T and Ti_k^0 on the position $\tilde{x}_{max}$. In particular, it has been observed that the added turbulence intensity reaches its maximum faster if the wake recovery is enhanced. This is the case for large values of the thrust coefficients, *i.e.*, for large gradients between the wind velocity at the rotor and the undisturbed flow (U_∞). Denoting by U_R the axial wind velocity at the rotor hub, the position $\tilde{x}_{max}$ is expected to vary as:

$$\tilde{x}_{max} \sim \frac{U_R}{U_\infty}. \tag{2.25}$$

The velocity ratio U_R/U_∞ can be related to the thrust coefficient C_T using the Actuator Disk Theory and the definition of the induction factor "a":

$$1 - a = \frac{U_R}{U_\infty} = \sqrt{1 - C_T} \tag{2.26}$$

Besides that, high atmospheric turbulence intensities are known to accelerate the recovery process and therefore reduce $\tilde{x}_{max}$. As a matter of fact, Fig. 2.1, Fig. 5.1 (App. 5.2) and Fig. 5.3 (App. 5.2) show that a variation of Ti_k^0 has, in general, more impact on the position $\tilde{x}_{max}$ of the turbulence intensity peak than a modification of C_T. The following relation for $\sigma = \tilde{x}_{max}$ is proposed:

$$\tilde{x}_{max} = \frac{\sqrt{1 - C_T}}{\psi\, \mathrm{Ti}_k^0}, \tag{2.27}$$

where ψ is an unknown constant. An optimization process is then carried out to determine the value of ψ that ensures the greatest fidelity of the model Eq. 2.27. As a reference, the position $\tilde{x}_{max}^{RANS}$ of the added turbulence intensity peak can be recovered from the RANS look-up table provided by EllipSys, for all combinations of C_T and Ti_k^0. The value of ψ is eventually selected so as to minimize the sum of the absolute difference $|\tilde{x}_{max} - \tilde{x}_{max}^{RANS}|$ over all the (C_T,Ti_k^0) combinations. Eventually, the value of the optimal parameter of Eq. 2.27 is found to be

$$\psi = 2.03 \tag{2.28}$$

Excellent agreement is shown in Sec. 2.3.2 between the model (Eq. 2.27) and the RANS data. Moreover, a relative error ϵ_{pos} ([%]) on the position of the maximum $\tilde{x}_{max}$ can be defined as:

$$\epsilon_{pos}(C_T, \mathrm{Ti}_k^0) = 100 \times \frac{\tilde{x}_{max} - \tilde{x}_{max}^{RANS}}{\tilde{x}_{max}^{RANS}}, \tag{2.29}$$

This error aims to assess the reliability of the model (Eq. 2.27) in a quantitative manner.

It is interesting to notice that the optimization process can be carried out with an alternative form of Eq. 2.27,

$$\tilde{x}_{max} = \frac{(1 - C_T)^{\phi}}{\psi\,(\mathrm{Ti}_k^0)^{\theta}}, \tag{2.30}$$

where two additional parameters, ϕ and θ, are introduced for more generality. Values of the parameters ψ, ϕ and θ have been tested over a large range with numerical steps as small as 0.001, resulting in the optimal set:

$$\psi = 2.321, \quad \phi = 0.485, \quad \theta = 1.036. \tag{2.31}$$

This very encouraging result therefore seems to confirm the relevance of the reasoning behind Eq. 2.27. Note that the size of the numerical step used to determine the optimal value of ψ is discussed in Sec. 2.4.3.

In light of the results obtained in Sec. 2.1.2 for Eq. 2.21 (Fig. 2.3), it is now clear that a Rayleigh function cannot satisfyingly be used to estimate the downstream distance dependence in the far wake. This can be explained by the fact that the characteristic size of the eddies, l_c in Eq. 2.13, is considered equal to the rotor radius R at any downstream distance. Inspired by the two theoretical scalings introduced in Sec. 2.1.1 and validated in Sec. 2.1.2, an expression for a third $\Delta\mathrm{Ti}_{k,max}$ model is proposed as:

$$\boxed{\Delta\mathrm{Ti}_{k,max} = \gamma \sqrt{1 - \sqrt{1 - C_T}}\, f_N(\tilde{x}) \quad \text{with} \quad f_N(\tilde{x}) = \begin{cases} (\tilde{x}/\sigma)\, \exp\left(\frac{\sigma^2 - \tilde{x}^2}{2\sigma^2}\right) & \text{if } \tilde{x} \leqslant \sigma \\ (\tilde{x}/\sigma)^{-1/3} & \text{if } \tilde{x} \geqslant \sigma \end{cases}} \tag{2.32}$$

where $\sigma = \tilde{x}_{max}$ is given by Eq. 2.27 with $\psi = 2.25$, and where γ is the scaling parameter. Similarly to the procedure followed for the first two models (Eq. 2.22 and Eq. 2.24), the scaling parameter γ is computed as:

$$\gamma = \frac{\Delta\mathrm{Ti}_{k,max}^{RANS}(\tilde{x}, C_T, \mathrm{Ti}_k^0)}{\sqrt{1 - \sqrt{1 - C_T}}\, f_N(\tilde{x})}, \tag{2.33}$$

with $f_N(\tilde{x})$ given by Eq. 2.32. The corresponding results are discussed in Sec. 2.3.2. Note that the far wake expression of the downstream distance dependence is modified with respect to Eq. 2.23 to ensure that $f_N(\tilde{x} = \sigma) = 1$ in both the near wake and the far wake expressions. It can already be anticipated that this modification will tend to affect the quality of the excellent agreement between the second model (Eq. 2.23) and the RANS data in the far wake.

2.3.2 Results

The result of the optimization analysis carried out to define the value of $\psi = 2.03$ in Eq. 2.27 are discussed. Fig. 2.5 explicitly compares the RANS data $\tilde{x}_{max}^{RANS}$ and the good approximations, $\tilde{x}_{max}$, provided by Eq. 2.27 for representative values of C_T and Ti_k^0. Furthermore, the relative errors computed under representative conditions are given in Tab. 2.1. Among all the tested conditions, the largest relative error occurs for $C_T = 0.2$ and $\mathrm{Ti}_k^0 = 0.4$ and corresponds to a relative error of $\epsilon_{pos} = +60\%$ between $\tilde{x}_{max} = 1.10$ and $\tilde{x}_{max}^{RANS} = 0.69$. Of all the values of C_T and Ti_k^0 commonly met in practice (Tab. 2.1), it is important to notice that a relative error $\epsilon_{pos} = -36\%$ is obtained for $C_T = 0.8$ and $\mathrm{Ti}_k^0 = 0.15$. The impact that this large relative error has on the accuracy of the final model is to be investigated in Sec. 2.4.3 through a sensitivity analysis.

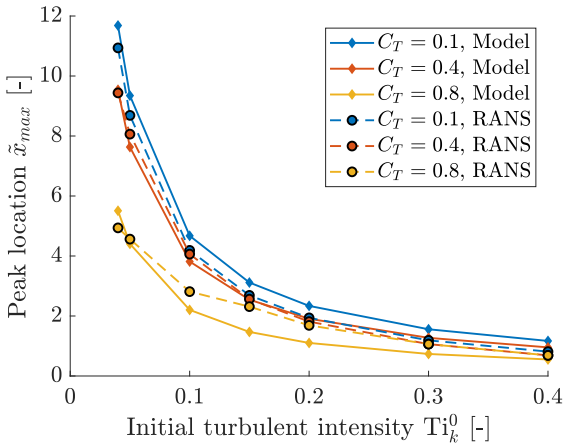

Figure 2.5: Downstream position at which the maximum added turbulence intensity $\mathrm{Ti}_{k,absmax}$ is reached. The predictions $\tilde{x}_{max}$ of Eq. 2.27 are compared to the RANS data $\tilde{x}_{max}^{RANS}$ for different combinations of C_T and Ti_k^0.

Table 2.1: Relative error ϵ_{pos} [%] computed with Eq. 2.29 for representative flow conditions.

C_T	$\mathrm{Ti}_k^0 = 0.05$	$\mathrm{Ti}_k^0 = 0.15$	$\mathrm{Ti}_k^0 = 0.30$
0.1	7.6	16	31
0.4	-5.3	-0.7	20
0.8	-3.4	-36	-31

The results of Eq. 2.33 are computed and depicted in Fig. 2.6. As said earlier, to any combination of C_T and Ti_k^0 corresponds a specific value of σ (*i.e.*, $\tilde{x}_{max}$), retrieved from Eq. 2.27. At a given distance from the rotor, $f_N(\tilde{x})$ cristalizes to the first or the second expression of Eq. 2.32 depending on the situation. For instance, at $\tilde{x} = 1$, the first expression of $f_N(\tilde{x})$ is to be considered for conditions $C_T = 0.1$, $\mathrm{Ti}_k^0 = 0.3$. At the same position $\tilde{x} = 1$, the second

expression $f_N(\tilde{x})$ is employed for conditions $C_T = 0.8$ and $\mathrm{Ti}_k^0 = 0.3$. In Fig. 2.6, a non-linear and decreasing trend can be observed at $x = 1D$. The C_T dependence appears to be well accounted for since the spacings between the curves are small. Discrepancies are however noticed for $C_T = 0.8$ if $\mathrm{Ti}_k^0 \geqslant 0.3$ as the corresponding σ values are such that $\tilde{x} = 1 > \sigma$. Fig. 2.6 clearly shows that, when further downstream distances are considered, the far wake expression of Eq. 2.32 is gradually used for more combinations of (C_T,Ti_k^0). In addition, thanks to the expression $f_N(\tilde{x}) \sim \tilde{x}^{-1/3}$, no significant evolution along $\tilde{x}$ is observed in Fig. 2.6 in the far wake. Nevertheless, the presence of an additional C_T dependence (through σ) in $f_N(\tilde{x}) = (\tilde{x}/\sigma)^{-1/3}$ results in a substantially larger spacings between the C_T curves than what has been observed with Eq. 2.23 in Fig. 2.4.

Overall, this third model for $\Delta\mathrm{Ti}_{k,max}$ brings a significant improvement solely for a very limited set of downstream distances, essentially centered around $\tilde{x} = 1$. In this region, the C_T dependence is well modelled for most values of the atmospheric turbulence intensity but rapidly leads to large discrepancies further away from the rotor. It seems difficult that a simple expression of the γ parameter can exist in view of the large variability in either x or C_T introduced by this new model in most conditions. For that reason, no further study of this model is provided in the scope of this project. However, it is good to remember that the analysis carried out in this section allowed to determine a reasonably accurate model for the position of the added turbulence intensity peak, $\tilde{x}_{max}$ (Eq. 2.27). As shown later in this work, this quantity is to play an important part in the final model for the amplitude of the added turbulence intensity.

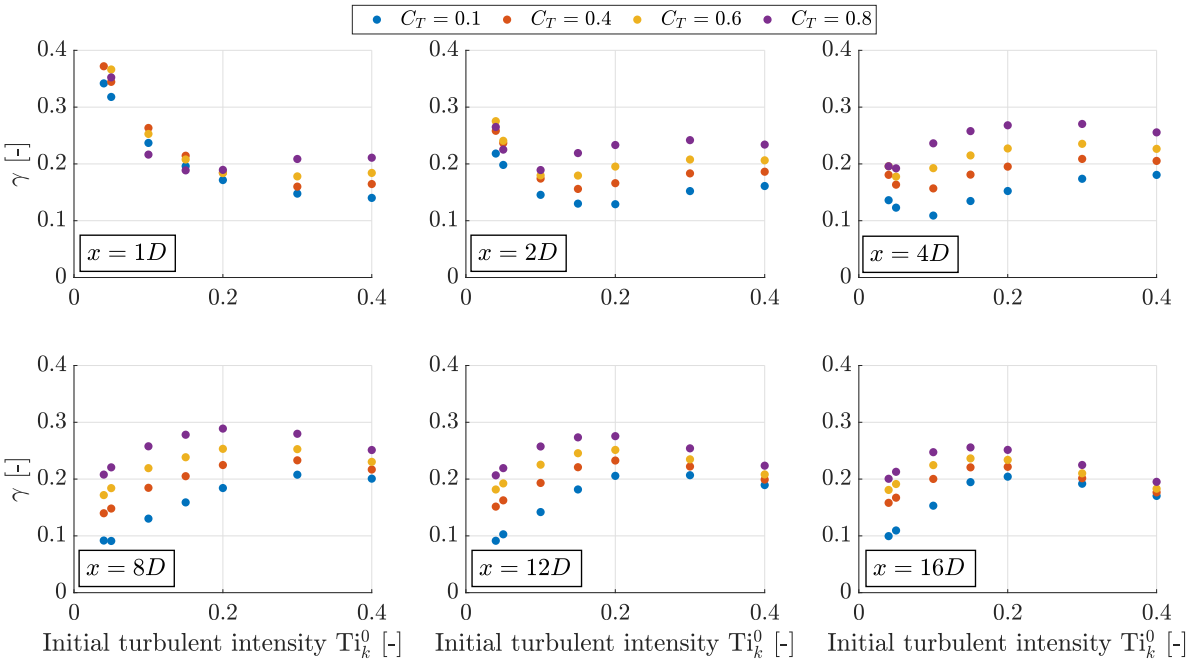

Figure 2.6: Evolution of the scaling parameter α as function of Ti_k^0. Data are computed with Eq. 2.33 for four different thrust coefficients, at six representative distances downstream.

2.4 Development of a second approach for the design of a new added turbulence intensity model

2.4.1 Methodology

In light of the previous sections, an alternative approach is considered for the modelling of the added turbulence intensity. The idea of a downstream distance dependence described by a Rayleigh-like function is retained, together with the expression of the position $\tilde{x}_{max}$ of the added turbulence intensity peak developed in Sec. 2.3.

In Sec. 2.2.1, the first two attempts made to derive a new added turbulence intensity model (Eq. 2.21 and Eq. 2.23) implicitly rely on the assumption that the turbulence intensity can be decomposed as the product of three functions:

$$\Delta \mathrm{Ti}_{k,max} = A(\mathrm{Ti}_k^0)\, \Phi(C_T)\, f_N(\tilde{x}), \tag{2.34}$$

where $A(\mathrm{Ti}_k^0)$ is the scaling coefficient denoted as $\alpha(\mathrm{Ti}_k^0)$ and $\beta(\mathrm{Ti}_k^0)$ in the first and second models, respectively. Although some trends for α and β seem to emerge under particular conditions (Fig. 2.3 and Fig. 2.4), results have shown that both scaling coefficients still substantially depend on the thrust coefficient and the downstream distance. A potential improvement is subsequently investigated in Sec. 2.3, where the downstream distance dependence $f_N(\tilde{x})$ is modelled based on both Eq. 2.21 and Eq. 2.23. Note that this third model slightly deviates from the form of Eq. 2.34 as $f_N(\tilde{x})$ also depends on Ti_k^0 and C_T through the σ parameter.

Contrary to those models, the alternative approach introduced in this section does not rely on the decomposition of $\Delta \mathrm{Ti}_{k,max}$ into a product of three terms, each depending on either C_T, Ti_k^0 or $\tilde{x}$. Instead, observations of the RANS database suggest that the position $\tilde{x}_{max}$ and the corresponding amplitude $\Delta \mathrm{Ti}_{k,absmax}$ of the turbulence intensity peak along the streamwise direction are key parameters in the modelling of $\mathrm{Ti}_{k,max}(\tilde{x}, C_T, \mathrm{Ti}_k^0)$. The following self-similar expression is therefore proposed:

$$\Delta \mathrm{Ti}_{k,max} = \Delta \mathrm{Ti}_{k,absmax}\, f_N\left(\tilde{x}/\tilde{x}_{max}\right), \tag{2.35}$$

where the shape function f_N takes a unitary value for $\tilde{x} = \tilde{x}_{max}$. As a reliable expression for $\tilde{x}_{max}(C_T, \mathrm{Ti}_k^0)$ has been obtained in the previous section (Eq. 2.27), the task that remains at this point is to ascertain analytical relationships for $\Delta \mathrm{Ti}_{k,absmax}$ and f_N.

In order to determine an expression for $\Delta \mathrm{Ti}_{k,absmax}$, one simple idea would be to use the peak value predicted by Eq. 2.32 (*i.e.*, for $\tilde{x} = \tilde{x}_{max}$):

$$\Delta \mathrm{Ti}_{k,absmax} = \lambda \sqrt{1 - \sqrt{1 - C_T}}, \tag{2.36}$$

with λ being a scaling parameter. Besides that, empirical testings appear to suggest the use of an even simpler expression:

$$\Delta \mathrm{Ti}_{k,absmax} = \lambda\, C_T. \tag{2.37}$$

To determine the value of , one should first recall that the comparison of the existing models carried out in Sec. 2.1.2 have shown little variation of $\Delta\mathrm{Ti}_{k,absmax}$ with Ti_k^0. In order to further investigate the reason behind this observation, the evolution of $\Delta\mathrm{Ti}_{k,absmax}^{RANS}$ was also studied using the second definition of the added turbulence intensity (Eq. 1.11). It appeared that, when $\Delta\mathrm{Ti}_k$ is defined according to Eq. 1.11, the amplitude of the added turbulence peak, $\Delta\mathrm{Ti}_{k,absmax}^{RANS}$ decreases significantly and non-linearly with Ti_k^0. A potential explanation could be that, if the turbulent kinetic energy of the atmospheric flow (k_∞) is increased by a small increment, the turbulent kinetic energy of the wake (k) is consequently increased by approximately the same increment, so that Δk (Eq. 1.13) remains constant. As a result, the value of $\Delta\mathrm{Ti}_{k,absmax}$ as defined by Eq. 1.12 is not affected, *i.e.* $\Delta\mathrm{Ti}_{k,absmax}$ is not a function of Ti_k^0. On the contrary, the definition Eq. 1.11 naturally leads to the non-linear behavior that has been observed. This interesting conclusion therefore points out that definition Eq. 1.12, in addition to relying on the energy additivity assumption, simplifies the modeling of $\Delta\mathrm{Ti}_{k,absmax}$. Hence, it follows that the scaling parameter λ is assumed to be a constant, the optimal value of which is defined so as to minimize the absolute difference $|\Delta\mathrm{Ti}_{k,absmax}^{RANS}$ - $\Delta\mathrm{Ti}_{k,absmax}|$ summed over all the tested combinations of C_T and Ti_k^0. The result of this optimization process is shown in the next section for $\Delta\mathrm{Ti}_{k,absmax}$, computed with both Eq. 2.36 and Eq. 2.37. Eventually, the minimum error on $\Delta\mathrm{Ti}_{k,absmax}$ (Eq. 2.37) is obtained for

$$\lambda = 0.175. \tag{2.38}$$

The definition Eq. 2.37 is found to perform slightly better than Eq. 2.36, for which the optimal scaling coefficient is $\lambda = 0.166$. Similarly to the relative error ϵ_{pos} on the position $\tilde{x}_{max}$ of the added turbulence intensity peak (Eq. 2.29), a relative error ϵ_{amp} on the amplitude of the peak is defined as

$$\epsilon_{amp}(C_T, \mathrm{Ti}_k^0) = 100 \times \frac{\Delta\mathrm{Ti}_{k,absmax} - \mathrm{Ti}_{k,absmax}^{RANS}}{\mathrm{Ti}_{k,absmax}^{RANS}}. \tag{2.39}$$

and allows to quantify the quality of the modelling of $\Delta\mathrm{Ti}_{k,absmax}$.

Given the self-similar expression Eq. 2.35, it is necessary to determine a family of shape functions f_N appropriate to represent the downstream evolution of the added turbulence intensity. In light of the physical interpretation given in Sec. 2.1.2, it is clear that the shape function must show specific characteristics. In particular, the function must have a rapid growth before $\tilde{x} = \tilde{x}_{max}$, after which a decrease is observed, the latter being more or less rapid depending on the situation. Contrary to a Rayleigh function, a Weibull function with parameters k and c, *i.e.*,

$$f_{Wb}(\tilde{x}/\tilde{x}_{max}) = \frac{k}{c}\left(\frac{(\tilde{x}/\tilde{x}_{max})}{c}\right)^{k-1} \exp\left(-\frac{(\tilde{x}/\tilde{x}_{max})^k}{c^k}\right) \tag{2.40}$$

can be modified to reach a unitary maximum at $(\tilde{x}/\tilde{x}_{max}) = 1$ while keeping an additional free parameter.The following expression is proposed:

$$f_N(\tilde{x}/\tilde{x}_{max}) = \left(\frac{\tilde{x}}{\tilde{x}_{max}}\right)^m \exp\left(m\left(1 - \frac{\tilde{x}}{\tilde{x}_{max}}\right)\right), \tag{2.41}$$

where the additional free parameter is denoted m. In a sense, replacing the Rayleigh function (Eq. 2.13) by Eq. 2.41 somewhat allows to account for the variation of the characteristic size

of the large eddies, l_c (Eq. 2.13), which was simply taken equal to the rotor radius in the first model, Eq. 2.21. Eventually, the value of m can be set using a numerical optimization process described as follows.

- For each value of C_T and Ti_k^0, the quantities $\Delta\mathrm{Ti}_{k,max}^{RANS}(C_T, \mathrm{Ti}_k^0, \tilde{x})$, $\Delta\mathrm{Ti}_{k,absmax}^{RANS}(C_T, \mathrm{Ti}_k^0)$ and $\tilde{x}_{max}^{RANS}$ are retrieved from the RANS database.
- The quotient $\Delta\mathrm{Ti}_{k,max}^{RANS}/\Delta\mathrm{Ti}_{k,absmax}^{RANS}$ is then plotted against $\tilde{x}/\tilde{x}_{max}^{RANS}$ so that an empirical shape function is observed. This function is denoted $f_N^{RANS}(\tilde{x}/\tilde{x}_{max}^{RANS})$.
- For given C_T and Ti_k^0 values, the optimal value of m is chosen so as to minimize the quantity E_f defined as

$$E_f = \int_{\eta_1}^{\eta_2} |f_N^{RANS}(\eta) - f_N(\eta)|\, d\eta, \tag{2.42}$$

  where $d\eta = d(\tilde{x}/\tilde{x}_{max}^{RANS})$, $\eta_1 = 0$ and η_2 is so that the integration is performed over a downstream distance of $20D$.

As could have been expected, m is not a unique constant but takes slightly different values depending on C_T and Ti_k^0. Those values of m are stored in a look-up table. As will be observed in Fig. 2.8 (Sec. 2.4.2) for a wide variety of cases, good agreement is shown between the predictions f_N of Eq. 2.41 and the shape functions f_N^{RANS} recovered from the RANS database. Following the same logic as for ϵ_{pos} (Eq. 2.29) and ϵ_{amp} (Eq. 2.39), a measure of the quality of the estimations provided by f_N can be written as:

$$\epsilon_f(C_T, \mathrm{Ti}_k^0, \tilde{x}) = 100 \times \frac{f_N(\eta) - f_N^{RANS}(\eta)}{f_N^{RANS}(\eta)}, \tag{2.43}$$

with $\eta = \tilde{x}/\tilde{x}_{max}^{RANS}$. Attention should be paid to the fact that the ratio η is used as the argument of both f_N^{RANS} and f_N. This choice indeed allows to make sure that no modelling error of $\tilde{x}_{max}$ is implicitly contained in ϵ_f. In other words, ϵ_f defined in Eq. 2.43 reflects how close the empirical shape function f_N^{RANS} is to the theoretical Weibull shape used for f_N (Eq. 2.41). It should also be noted that, contrary to errors ϵ_{pos} and ϵ_{amp}, the error ϵ_f on the modelling of the empirical shape function f_N^{RANS} has an additional dependency of the downstream distance $\tilde{x}$.

Eventually, the methodology presented in this section allows to re-write the model introduced in Eq. 2.35 as

$$\boxed{\Delta\mathrm{Ti}_{k,max} = \lambda\, C_T \left(\frac{\tilde{x}}{\tilde{x}_{max}}\right)^m \exp\left(m\left(1 - \frac{\tilde{x}}{\tilde{x}_{max}}\right)\right) \quad \text{with} \quad \tilde{x}_{max} = \frac{\sqrt{1 - C_T}}{\psi\, \mathrm{Ti}_k^0}} \tag{2.44}$$

where $\lambda = 0.175$, $\psi = 2.03$ and for which the values of the parameter $m(C_T, \mathrm{Ti}_k^0)$ are stored in a look-up table. In general, it is advisable to replace a large look-up table by an empirical law derived from it to facilitate the use of the model. This can however only be done at the expense of additional errors introduced into the model, the impact of which needs to be accurately estimated through a sensitivity study. Such an analysis is performed in Sec. 2.4.3 and eventually supports the choice of a look-up table over an empirical relationship for the

modelling of the m parameter. Note that in the scope of this project, eight values of C_T are tested in the interval [0.1; 0.8], together with eight values of Ti_k^0 in [0.04; 0.4]. The resulting look-up table for m (App. 5.2) therefore only contains 64 elements, between which interpolation is recommended for greater accuracy.

2.4.2 Results

This section aims at evaluating the performances of the model developed for $\Delta\mathrm{Ti}_{k,max}$ using the alternative approach developed in Sec. 2.4.1. First, the results of the optimization process carried out to determine the optimal value of λ (Eq. 2.36 and Eq. 2.37) are discussed. In Fig. 2.7, only negligible variations of $\Delta\mathrm{Ti}_{k,absmax}^{RANS}$ with Ti_k^0 can be observed. Those slight fluctuations are essentially contained between the predictions of Eq. 2.36 (denoted "Model 1") and that of Eq. 2.37 (denoted "Model 2"). Although good agreement is shown in both cases, Eq. 2.37 is found to lead to a slightly smaller error, for which the optimal value of the scaling coefficient is $\lambda = 0.175$. Some representative values of the relative error ϵ_{amp} defined in Eq. 2.39 are summarized in Tab. 2.2.

Table 2.2: Relative error ϵ_{amp} [%] computed with Eq. 2.39 for representative flow conditions.

	$\mathrm{Ti}_k^0 = 0.05$	$\mathrm{Ti}_k^0 = 0.15$	$\mathrm{Ti}_k^0 = 0.30$
$C_T = 0.1$	-17.3	-37.6	-44.9
$C_T = 0.4$	4.0	-5.8	-8.4
$C_T = 0.8$	-1.9	-0.7	4.8

From Tab. 2.2, it appears clear that for common values of the thrust coefficient, very little relative error is introduced by the modelling of the peak amplitude (Eq. 2.37). One should however bear in mind that the sensitivity analysis discussed in Sec. 2.4.3 is necessary to show that the impact of any small error ϵ_{amp} on the final model (Eq. 2.44) remains limited.

Although the peak amplitude $\Delta\mathrm{Ti}_{k,absmax}^{RANS}$ and the corresponding downstream position $\tilde{x}_{max}$ are related, the physical interpretation of Fig. 2.7 differs from that of Fig. 2.5 discussed in Sec. 2.3.2. In this last section, it has been observed that an increase in C_T led to higher velocity gradients and therefore to a faster wake recovery, leading in turn to a reduction of the value of $\tilde{x}_{max}$. Larger values of the atmospheric turbulence intensity Ti_k^0 also appeared to further reduce $\tilde{x}_{max}$ by facilitating the mixing with the undisturbed flow. Contrary to the effect that an increase of C_T has on $\tilde{x}_{max}$, Fig. 2.7 explicitly shows that larger values of C_T lead to larger amplitudes of the turbulence intensity peak, $\Delta\mathrm{Ti}_{k,absmax}$. This is expected as the production of turbulent kinetic energy is enhanced by an increase of velocity gradients.

As mentioned above, the m parameter used to describe the family of shape functions (Eq. 2.41) depends on both C_T and Ti_k^0. The values of m are first obtained through the minimization of the absolute error defined in Eq. 2.42. These values are subsequently injected in Eq. 2.41 and the resulting shape functions are displayed in Fig. 2.8 for a set of representative

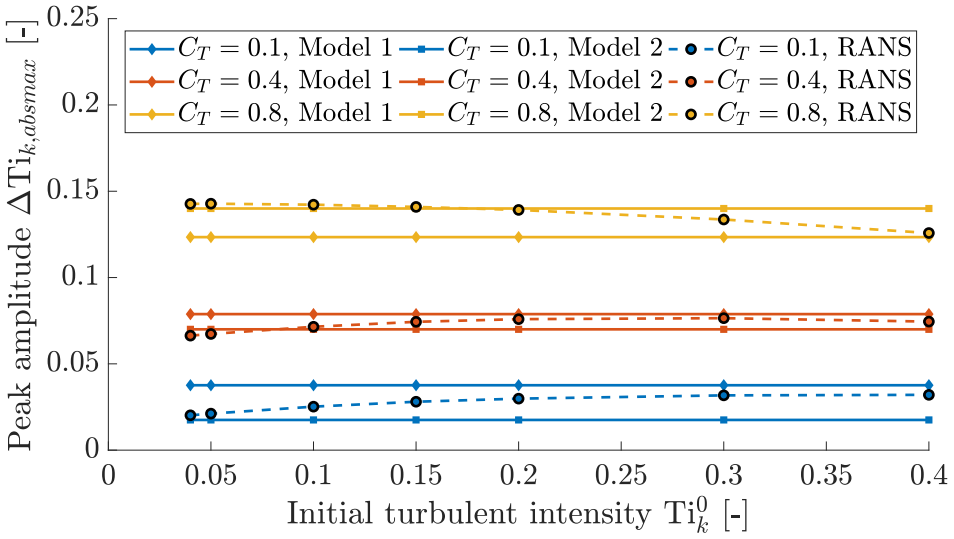

Figure 2.7: Comparison of the amplitude of the added turbulence intensity peak $\Delta \mathrm{Ti}_{k,absmax}$ as computed with Eq. 2.36 and Eq. 2.37, respectively denoted by "Model 1" and "Model 2". The quantity $\Delta \mathrm{Ti}_{k,absmax}^{RANS}$ is recovered from the RANS database and is used as the reference.

conditions. The corresponding relative error ϵ_f (Eq. 2.43) is computed at each downstream position, from which the maximum and minimum values of the relative error are recovered and shown in Tab. 2.3. The set of downstream distances over which the maximum and minimum values of ϵ_f are retrieved is however limited to the far wake region (*i.e.*, $\tilde{x} > \tilde{x}_{max}$). This choice has been made to avoid considering the cases for which $f_N << f_N^{RANS}$. Contrary to its empirical counterpart (f_N^{RANS}), the modelled shape function f_N indeed equals 0 at $\tilde{x} = 0$ and therefore shows a sharper evolution with downstream distances in the near wake.

Table 2.3: Relative error ϵ_f [%] computed with Eq. 2.43 for representative flow conditions. The maximum and minimum values of ϵ_f along $\tilde{x}$ are given for each tested combination of C_T and Ti_k^0.

(a) Maximum values of ϵ_f

	$\mathrm{Ti}_k^0 = 0.05$	$\mathrm{Ti}_k^0 = 0.15$	$\mathrm{Ti}_k^0 = 0.30$
$C_T = 0.1$	0.03	6.5	7.1
$C_T = 0.4$	1.5	6.1	8.0
$C_T = 0.8$	4.7	6.1	8.7

(b) Minimum values of ϵ_f

$\mathrm{Ti}_k^0 = 0.05$	$\mathrm{Ti}_k^0 = 0.15$	$\mathrm{Ti}_k^0 = 0.30$
-5.3	-1.5	-2.4
-4.6	-0.5	-3.4
-12.2	-7.6	-13.3

It is observed from Fig. 2.8 that f_N tends to overestimates f_N^{RANS} right after the peak of added turbulence intensity is reached. Tab. 2.3 further indicates that the amplitude of these overestimation increases with Ti_k^0 but does not significantly vary with C_T. By contrast, the model shows clear underestimation of f_N^{RANS} in the furthest part of the wake only, particularly at large C_T values. One can finally see from Fig. 2.8 that the global appearance of the empirical

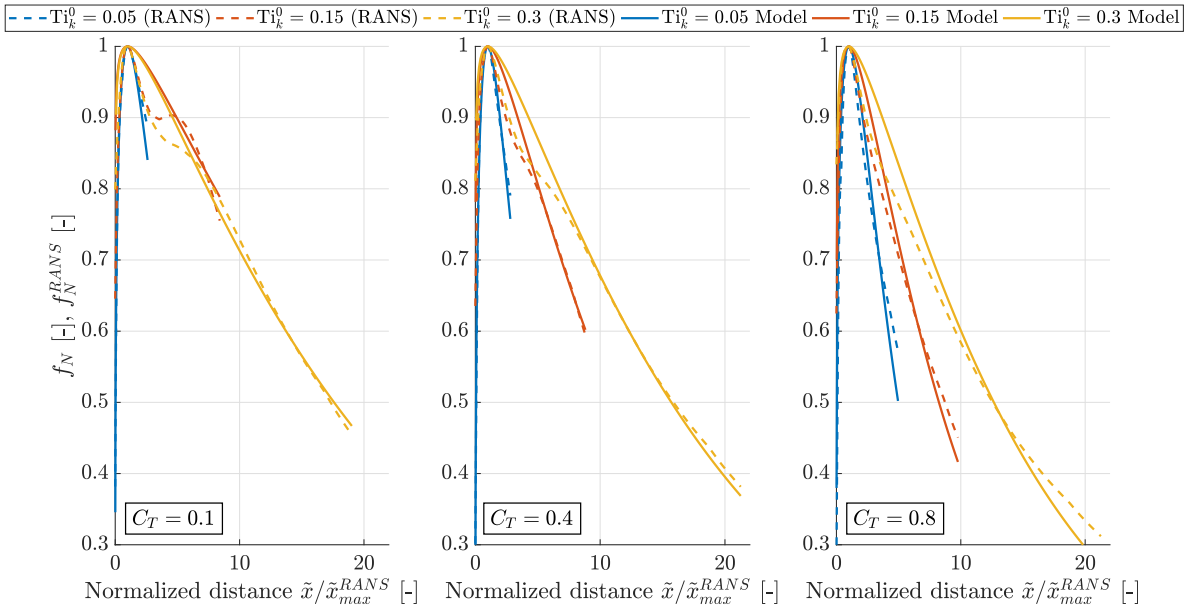

Figure 2.8: Comparison of the shape functions recovered from the RANS database (f_N^{RANS}) with the model predictions f_N computed by minimization of Eq. 2.42. Several representative values of C_T and Ti_k^0 are tested.

shape function f_N^{RANS} tends to deviate more from the theoretical Weibull profile (f_N) for low values of C_T. This is especially true for higher atmospheric turbulence intensities as the level of added turbulence is driven by an enhanced mixing and low velocity gradients, resulting in irregular empirical shape functions (*i.e.*, f_N^{RANS}). For larger thrust coefficients, the RANS simulations show that f_N^{RANS} resembles a Weibull profile more, for which acceptable estimations are provided by Eq. 2.41.

Unlike the first three models (Eq. 2.21, Eq. 2.23 and Eq. 2.32) for which the α, β and γ parameters were left undetermined, the alternative approach proposed in this section leads to the closed form expression Eq. 2.44. The performance of this new comprehensive model can therefore be compared to that of the existing models similarly to what has been done in Sec. 2.1.2. Note that the relative cumulative error ε defined in Eq. 2.14 is used again as an indicator of the fidelity of the model. Overall, Fig. 2.9 clearly shows that the new model developed in this section conducts to considerable improvement in a wide variety of situations. In particular, it can be seen from Fig. 2.9a, Fig. 2.9c and Fig. 2.9e that the model predictions almost perfectly overlap with the RANS data (represented by a continuous blue curve) provided that C_T is large enough. The near wake behavior also appears to be described with much higher fidelity than the existing models.

For values of the thrust coefficients smaller than 0.4, the new added turbulence intensity model fails to outperform the current models, especially for larger values of Ti_k^0. This could have been expected as Eq. 2.27 for $\tilde{x}_{max}$ (Tab. 2.1) and Eq. 2.37 for $\Delta\mathrm{Ti}_{k,absmax}$ ((Tab. 2.2)) simultaneously give relatively large discrepancies at low C_T values. In practice, it is however

very unlikely to encounter such small values of C_T so that the new model performs well in any standard conditions. It must also be emphasized that only moderate deterioration of the performance of the model is observed for increasing values of Ti_k^0. This great robustness is of the utmost importance as Eq. 2.44 is to be eventually combined with superpositions methods, *i.e.*, in conditions for which Ti_k^0 becomes larger as a result of the turbulence intensity added by the upstream turbines. For $\mathrm{Ti}_k^0 = 0.05$ and values of C_T larger than 0.1, it can be observed in Fig. 2.9b, that the error is essentially constant with C_T and substantially lower than that of the existing models.

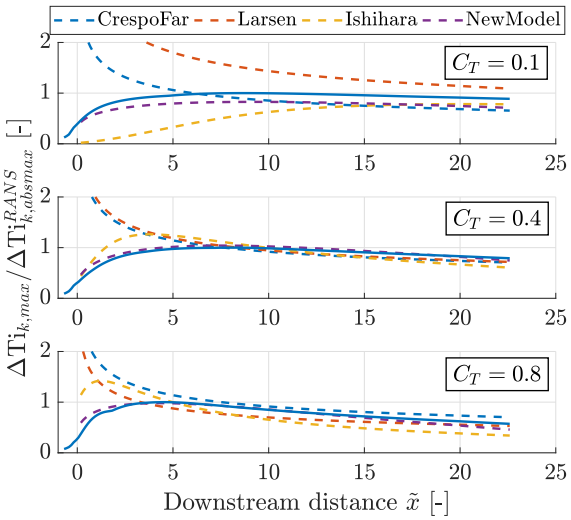

(a) $\mathrm{Ti}_k^0 = 0.05$ [-]

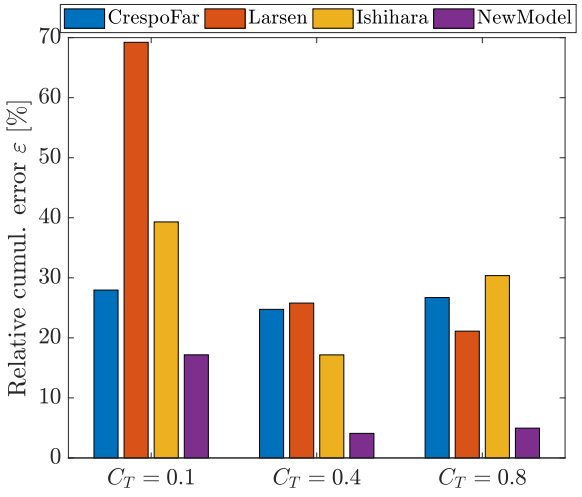

(b) $\mathrm{Ti}_k^0 = 0.05$ [-]

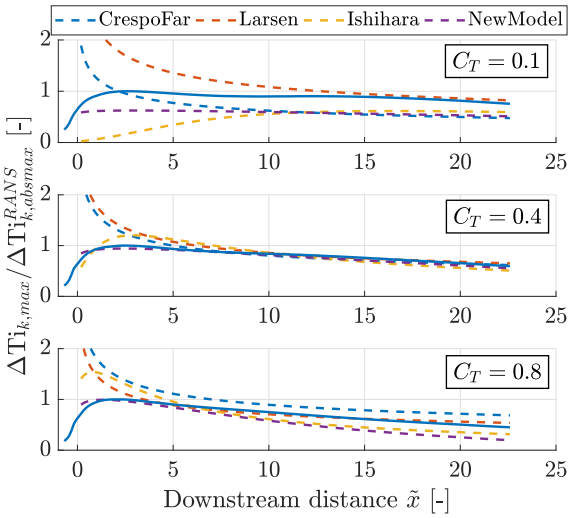

(c) $\mathrm{Ti}_k^0 = 0.15$ [-]

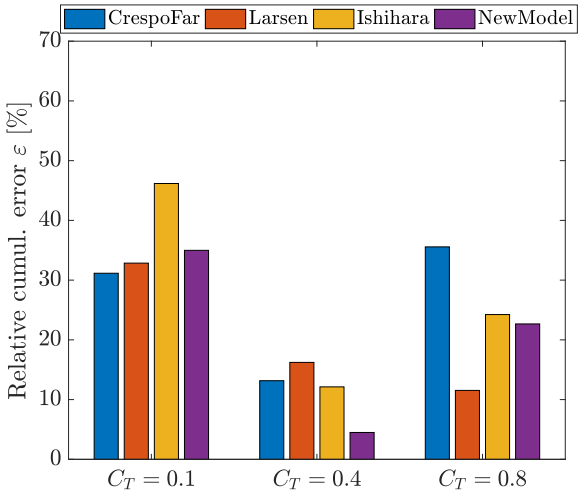

(d) $\mathrm{Ti}_k^0 = 0.15$ [-]

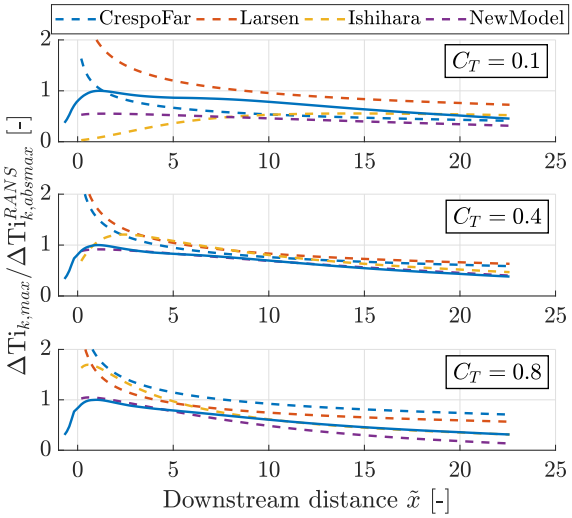

(e) $\mathrm{Ti}_k^0 = 0.30$ [-]

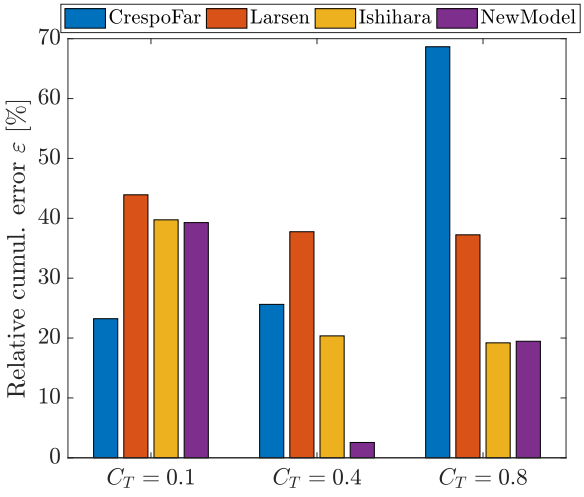

(f) $\mathrm{Ti}_k^0 = 0.30$ [-]

Figure 2.9: Normalized added turbulence intensity and relative cumulative error (Eq. 2.14) for different C_T and Ti_k^0. The continuous blue curves in Fig. 2.9a,2.9c,2.9e represent the RANS data.

As a conclusion, the alternative approach followed in this section results in a promising new model for the added turbulence intensity $\Delta\mathrm{Ti}_{k,max}$ (Eq. 2.44). A major improvement is shown in all the conditions that are to be met in practice. This new model is therefore to be implemented in the PyWake software in order to study the wake superposition effects. Although this model is based on physical considerations, it seems relevant to recall that the values of the parameters ψ (Eq. 2.27), λ (Eq. 2.37) and m (Eq. 2.41) are obtained through numerical optimization processes. As only a limited number of conditions are tested, the values of m are stored in a look-up table considerably smaller than the initial RANS database.

2.4.3 Sensitivity analysis

The sensitivity of the new one-dimensional model for the added turbulence intensity $\Delta\mathrm{Ti}_{k,max}$ (Eq. 2.35) is discussed in this section. In particular, the study is based on analytical developments and aims at evaluating the extent to which an error on $\tilde{x}_{max}$, $\Delta\mathrm{Ti}_{k,absmax}$ and f_N impacts $\Delta\mathrm{Ti}_{k,max}$. From the expression

$$\Delta\mathrm{Ti}_{k,max} = \Delta\mathrm{Ti}_{k,absmax}\, f_N\left(\tilde{x}/\tilde{x}_{max}\right) = \Delta\mathrm{Ti}_{k,absmax}\left(\frac{\tilde{x}}{\tilde{x}_{max}}\right)^m \exp\left(m\left(1-\frac{\tilde{x}}{\tilde{x}_{max}}\right)\right), \quad (2.45)$$

the analytical form of the error on the added turbulence intensity, *i.e.*, $d(\Delta\mathrm{Ti}_{k,max})$, can be written as a weighted sum, truncated to the first derivatives only:

$$d(\Delta\mathrm{Ti}_{k,max}) \simeq \frac{\partial\Delta\mathrm{Ti}_{k,max}}{\partial\Delta\mathrm{Ti}_{k,absmax}}\, d(\Delta\mathrm{Ti}_{k,absmax}) + \frac{\partial\Delta\mathrm{Ti}_{k,max}}{\partial f_N}\, d(f_N), \quad (2.46)$$

for which the two derivatives are trivially given by

$$\frac{\partial\Delta\mathrm{Ti}_{k,max}}{\partial\Delta\mathrm{Ti}_{k,absmax}} = f_N \quad \text{and} \quad \frac{\partial\Delta\mathrm{Ti}_{k,max}}{\partial f_N} = \Delta\mathrm{Ti}_{k,absmax}. \quad (2.47)$$

In Eq. 2.46, the error term $d(f_N)$ accounts for the discrepancy between the modelled shape function f_N evaluated at downstream positions $\tilde{x}/\tilde{x}_{max}$ and its empirical counterpart, evaluated at $\tilde{x}/\tilde{x}^{RANS}_{max}$. If f_N^{RANS} perfectly followed a Weibull shape of parameter m, assessing the impact of $d\tilde{x}_{max}$ and dm on $d(f_N)$ would require to evaluate:

$$d(f_N) = \frac{\partial f_N^{RANS}}{\partial\tilde{x}_{max}}\, d\tilde{x}_{max} + \frac{\partial f_N^{RANS}}{\partial m}\, dm. \quad (2.48)$$

However, in Sec. 2.4.2, Fig. 2.8 has explicitly shown that f_N^{RANS} deviates from the Weibull shape, leading to an inevitable relative error ϵ_f. Given that the derivatives of f_N^{RANS} with respect to $\tilde{x}_{max}$ and m cannot be obtained analytically, the following linear decomposition of $d(f_N)$ is assumed:

$$d(f_N) \simeq \frac{\partial f_N}{\partial\tilde{x}_{max}}\, d\tilde{x}_{max} + \frac{\partial f_N}{\partial m}\, dm + \epsilon_{f,abs} \quad (2.49)$$

in which the first term accounts for the error $d\tilde{x}_{max}$ on the position of the added turbulence intensity peak. The second and third terms are related to the error introduced when modelling

f_N^{RANS} as f_N and respectively represent the sensitivity of f_N to the m parameter and the remaining absolute error $\epsilon_{f,abs}$. This absolute error can simply be retrieved from the relative error ϵ_f as:

$$\epsilon_{f,abs} = (\epsilon_f/100)\, f_N^{RANS}. \tag{2.50}$$

Note that in expression Eq. 2.49, the error term dm denotes a discrepancy to the optimal value of m computed in Sec. 2.4.1 and stored in the look-up table. In the same section, the question arises as to whether it is possible to replace this look-up table by an analytical expression for the value of m. The answer to this question is discussed later in this section but can already be anticipated to strongly depend on the sensitivity of f_N with respect to m, *i.e.* the value of $(\partial f_N/\partial m)$ for a given set of flow conditions and downstream distances. The results of the analytical developments of the two derivatives in Eq. 2.49 read:

$$\begin{aligned} &\frac{\partial f_N}{\partial \tilde{x}_{max}} = A f_N \quad \text{where} \quad A = \frac{m}{\tilde{x}_{max}}\left(\frac{\tilde{x}}{\tilde{x}_{max}} - 1\right), \\ &\frac{\partial f_N}{\partial m} = B f_N \quad \text{where} \quad B = \ln\left(\frac{\tilde{x}}{\tilde{x}_{max}}\right) + 1 - \frac{\tilde{x}}{\tilde{x}_{max}}. \end{aligned} \tag{2.51}$$

Injecting Eq. 2.51, Eq. 2.49 and Eq. 2.47 into Eq. 2.46, the final form of the absolute error on the added turbulence intensity is:

$$d(\Delta \mathrm{Ti}_{k,max}) \simeq f_N\, d(\Delta \mathrm{Ti}_{k,absmax}) + \Delta \mathrm{Ti}_{k,absmax}\ (A f_N\, d\tilde{x}_{max} + B f_N\, dm + \epsilon_{f,abs}) \tag{2.52}$$

with A and B defined in Eq. 2.51. In this expression, the shape function f_N is by definition limited to a unitary value reached for $\tilde{x} = \tilde{x}_{max}$. Therefore, it is clear that an error $d(\Delta \mathrm{Ti}_{k,absmax})$ has an impact on $d(\Delta \mathrm{Ti}_{k,max})$ that is smaller or equal to $d(\Delta \mathrm{Ti}_{k,absmax})$ for any flow conditions and any downstream distances. Eq. 2.52 also shows that at $\tilde{x}_{max}$, since the values of A, B and $\epsilon_{f,abs}$ are equal to zero, the error on the final model $d(\Delta \mathrm{Ti}_{k,max})$ is solely dictated by the value of $d(\Delta \mathrm{Ti}_{k,absmax})$. At this stage of the sensitivity study, it is important to distinguish the different analyses that can be made on the basis of Eq. 2.52. First, this expression allows to evaluate the impact of the errors introduced by the modelling of $\tilde{x}_{max}$, $\Delta \mathrm{Ti}_{k,absmax}$ and f_N derived in Sec. 2.3.1 and Sec. 2.4.1. To this effect, $d\tilde{x}_{max}$ and $d(\Delta \mathrm{Ti}_{k,absmax})$ represent the absolute errors on the peak position ($\epsilon_{pos,abs}$) and on the peak amplitude ($\epsilon_{amp,abs}$) of the added turbulence intensity. Those last two quantities can easily be computed from ϵ_{pos} and ϵ_{amp} in Eq. 2.29 and Eq. 2.39 following the same reasoning as for $\epsilon_{f,abs}$ (Eq. 2.50). As the sensitivity of the model to the selected value of m is not evaluated in this part of the analysis, dm reduces to 0. Finally, the reference values (*i.e.*, the RANS generated values) $\tilde{x}_{max}^{RANS}$ and $\Delta \mathrm{Ti}_{k,absmax}^{RANS}$ are injected into Eq. 2.52. This results in the following form:

$$d(\Delta \mathrm{Ti}_{k,max}) \simeq f_N^{RANS}\, \epsilon_{amp,abs} + \Delta \mathrm{Ti}_{k,absmax}^{RANS}\, A f_N\, \epsilon_{pos,abs} + \Delta \mathrm{Ti}_{k,absmax}^{RANS}\, \epsilon_{f,abs}, \tag{2.53}$$

where the use of $f_N(\tilde{x}/\tilde{x}_{max})$ if preferred over f_N^{RANS} in the second and third terms for consistency with the assumption formulated to derive Eq. 2.49. Eventually, the results of Eq. 2.53 are represented against $\tilde{x}$ in Fig. 2.10 for four different conditions. The combinations of C_T and

Ti_k^0 are summarized in Tab. 2.4 and correspond to either conditions commonly met in practice (case C) or cases for which large discrepancies have been observed in Fig.2.9 (cases A, B and D).

Table 2.4: Summary of the tested conditions.

Case	A	B	C	D
C_T	0.1	0.1	0.8	0.8
Ti_k^0	0.05	0.3	0.05	0.3

Contrary to an empirical sensitivity study for which only the total error $d(\Delta\mathrm{Ti}_{k,max})$ could possibly be retrieved for a given set of conditions, the analytical development carried out in this section allows to clearly assess the sensitivity of the overall model to $\Delta\mathrm{Ti}_{k,absmax}$, $\tilde{x}_{max}$ and f_N separately. In Fig. 2.10, the first, second and third terms of Eq. 2.53 are expressed as percentages of $\Delta\mathrm{Ti}_{k,max}^{RANS}$ and denoted by T_1, T_2 and T_3 respectively. The square markers indicate the resulting values of ϵ_{tot}, *i.e.*, of the relative error on $\Delta\mathrm{Ti}_{k,max}$.

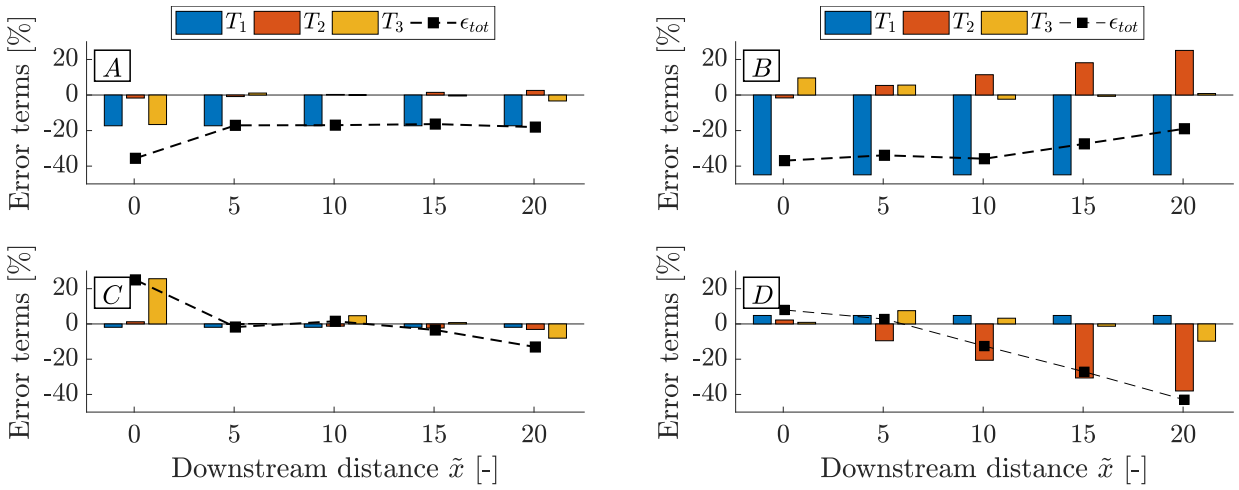

Figure 2.10: Analysis of the evolution of the relative error ϵ_{tot} [%] with downstream distance $\tilde{x}$ under different values of C_T and Ti_k^0 detailed in Tab. 2.4. T_1, T_2 and T_3 denote the three terms of Eq. 2.53 as percentages of $\Delta\mathrm{Ti}_{k,max}^{RANS}$, the square markers show the resulting values of ϵ_{tot}.

For all the four tested cases, the predicted trend of the total relative error on $\Delta\mathrm{Ti}_{k,max}$ represented in Fig. 2.10 are shown to agree with the values of the relative error deduced from Fig. 2.9. Those relative errors are summarized in Tab. 2.5 to facilitate the comparison. Despite slight discrepancies between the relative error empirically retrieved from Fig. 2.9 and the value predicted by Eq. 2.53, it clearly appears in Tab. 2.5 that the assumption made to linearize $d(f_N)$ (Eq. 2.49) holds for all the tested cases. One could point out a single exception: at the position of the rotor, *i.e.* at the first node of the grid used in EllipSys, the analytical development seems

Table 2.5: Comparison between the relative error ([%]) on $\Delta \mathrm{Ti}_{k,max}$ empirically retrieved from Fig.2.9 and the relative error ϵ_{tot} ([%]) computed by Eq. 2.53 and indicated by the square markers in Fig.2.10. For each case, the empirical and the analytical relative errors are given in the upper and lower lines respectively.

(a) Case A

$\tilde{x}=0$	$\tilde{x}=5$	$\tilde{x}=10$	$\tilde{x}=15$	$\tilde{x}=20$
-9.4	-16.8	-17.1	-16.8	-18.3
-35.6	-17.1	-17.0	-16.4	-18.5

(b) Case B

$\tilde{x}=0$	$\tilde{x}=5$	$\tilde{x}=10$	$\tilde{x}=15$	$\tilde{x}=20$
-37.2	-39.7	-41.4	-37.4	-33.1
-36.9	-33.9	-35.8	-27.5	-19.0

(c) Case C

$\tilde{x}=0$	$\tilde{x}=5$	$\tilde{x}=10$	$\tilde{x}=15$	$\tilde{x}=20$
70.3	-1.9	0.8	-4.1	-13.7
25.0	-1.76	1.5	-3.4	-13.1

(d) Case D

$\tilde{x}=0$	$\tilde{x}=5$	$\tilde{x}=10$	$\tilde{x}=15$	$\tilde{x}=20$
16.4	-2.5	-20.3	-35.1	-49.6
7.9	2.8	-12.6	-27.1	-43.0

to underestimate the value of the relative error on $\Delta \mathrm{Ti}_{k,max}$.

For cases A and B, Fig. 2.10 indicates that the model respectively underestimates by about 20% and 40% the actual value of $\Delta \mathrm{Ti}^{RANS}_{k,absmax}$ observed in Fig. 2.9a and Fig. 2.9e. From Fig. 2.10, it appears that this is mainly due to the error ϵ_{amp} on the amplitude of the maximum added turbulence intensity. For case B, the effect of ϵ_{pos} through T_2 can be seen to counterbalance T_1. In case C, Fig. 2.10 shows that the new model for the added turbulence intensity introduces an overestimation with respect to $\Delta \mathrm{Ti}^{RANS}_{k,max}$ in the near wake, followed by a slight underestimation in the far wake. This indeed seems to be the case as observed in Fig. 2.9a. Moreover, Fig. 2.10 allows to realize that the term T_3 in Eq. 2.53 is the main responsible for both the overestimation in the near wake and the underestimation observed in the far wake.

Contrary to cases A and B, cases C and D are combinations of C_T and Ti^0_k for which the effect of an error on the modelling of the peak position $\tilde{x}_{max}$ matters. In Fig. 2.10, case D, it is interesting to notice that the effects of ϵ_{amp} and ϵ_{pos} through T_1 and T_2 again seem to offset each other, at a distance of about $5D$ behind the rotor. Beyond this point, the error on the modelling of the peak position dominates and displays a decreasing trend. This trend is furthermore linear, as could have been expected from the A term in Eq. 2.51. In the far wake for case D, the large values of T_2 are partially justified by the important relative errors ϵ_{pos} computed in Sec. 2.3.2 and shown in Tab. 2.1. More generally, it can be concluded, by comparison of Fig. 2.10 with the values of ϵ_{pos} (Tab. 2.1), ϵ_{amp} (Tab. 2.2) and ϵ_f (Tab. 2.3), that the maximum along $\tilde{x}$ of the relative error on $\Delta \mathrm{Ti}_{k,max}$ is essentially given by the value of either ϵ_{pos}, ϵ_{amp} or ϵ_f depending on the flow conditions. In other words, the new model for the added turbulence intensity never amplifies the modelling errors made on $\tilde{x}_{max}$, $\Delta \mathrm{Ti}_{k,absmax}$ or f_N. For that reason, the following expression for the bound on the total error ϵ_{tot} is proposed:

$$|\epsilon_{tot}(C_T, \mathrm{Ti}^0_k, \tilde{x})| \leqslant \max(\epsilon_{pos}, \epsilon_{amp}, \epsilon_f), \tag{2.54}$$

It is crucial to highlight that the validity of this empirical expression is challenged in some rare cases for which two of the three relative errors ϵ_{amp}, ϵ_{pos} and ϵ_f have large amplitudes that add up. Therefore, one should keep in mind that Eq. 2.54 has no mathematical basis and simply provides a quick estimate of the probable total relative error ϵ_{tot} under a given set of conditions.

In light of this result, a sensitivity analysis can be further applied to the absolute error terms $d(\tilde{x}_{max})$ and $d(\Delta \mathrm{Ti}_{k,absmax})$ to identify the impact of a calibration errors on ψ and λ. From the expressions Eq. 2.27 and Eq. 2.37, the absolute errors $d(\tilde{x}_{max})$ and $\Delta \mathrm{Ti}_{k,absmax}$ can be decomposed as:

$$d(\tilde{x}_{max}) = \frac{\partial \tilde{x}_{max}}{\partial \psi}\, d\psi = -\frac{\sqrt{1-C_T}}{\psi^2\, \mathrm{Ti}_k^0}\, d\psi \tag{2.55}$$

$$d(\Delta \mathrm{Ti}_{k,absmax}) = \frac{\partial \Delta \mathrm{Ti}_{k,absmax}}{\partial \lambda}\, d\lambda = C_T\, d\lambda. \tag{2.56}$$

Moreover, Eq. 2.55 can be re-written as $d(\tilde{x}_{max}) = -(\tilde{x}_{max}/\psi)\, d\psi$, for which Fig. 2.5 can advantageously be consulted to retrieve the values of $\tilde{x}_{max}$. It is clear that the highest sensitivity to ψ is reached with $C_T = 0.1$ and $\mathrm{Ti}_k^0 = 0.05$, for which $\tilde{x}_{max}^{RANS} = 8.69$ is estimated to be $\tilde{x}_{max} = 9.35$ by Eq. 2.27 with $\psi = 2.03$. Under those conditions, one can investigate the maximum numerical step $d\psi$ that can be used to determine the optimal value of ψ in the optimization process carried out in Sec. 2.3.1. Similarly for the optimization process of λ (Sec. 2.4.1), $C_T = 0.8$ leads to the highest sensitivity in Eq. 2.56 and this condition is therefore used to determine the suitable numerical step $d\lambda$. The relative errors on the values of the peak position $\tilde{x}_{max} = 9.35$ and the peak amplitude $\Delta \mathrm{Ti}_{k,absmax} = 0.14$, modelled with the optimal parameters $\psi = 2.03$ and $\lambda = 0.175$ are given in Tab. 2.6 for different numerical steps $d\psi$ and $d\lambda$.

Table 2.6: Sensitivity of the modelling of the peak position and amplitude to the calibration of ψ and λ. The results are given in terms of the relative errors ([%]) on the modelled peak position and amplitude (*i.e.*, $\tilde{x}_{max}$ and $\Delta \mathrm{Ti}_{k,absmax}$) for different numerical steps $d\psi$ and $d\lambda$ respectively.

(a) Numerical steps for ψ

Step $d\psi$	0.1	0.01	0.001
Rel. Error	-4.9	-0.5	-0.05

(b) Numerical steps for λ

Step $d\lambda$	0.1	0.01	0.001
Rel. Error	57	5.7	0.6

If one wants to limit the calibration error on the modelled values of $\tilde{x}_{max}$ and $\Delta \mathrm{Ti}_{k,absmax}$ to less than 1%, Tab. 2.6 seems to indicate that the numerical steps $d\psi = 0.01$ and $d\lambda = 0.001$ ought to be selected. Attention should be drawn to the fact that the relative errors on $\tilde{x}_{max}$ and $\Delta \mathrm{Ti}_{k,absmax}$, denoted by "Rel. Error" in Tab. 2.6, are different quantities than the relative error ϵ_{pos} and ϵ_{amp} defined in Eq. 2.29 and Eq. 2.39. As a matter of fact, it can be shown that, for the flow conditions of interest ($C_T = 0.1$ and $\mathrm{Ti}_k^0 = 0.05$), a small calibration error $d\psi = 0.1$ would be beneficial as it would reduce the value of ϵ_{pos} from 7.6% (Tab. 2.1) to 2.3%. Considering the evolution of ϵ_{pos} with $d\psi$ when investigating the effect of a calibration error

appears misleading and the relative error on $\tilde{x}_{max}$ should therefore be preferred.

A key element to bear in mind is that the sensitivity analysis of the model has so far been carried out assuming that the value of the parameter m in Eq. 2.45 is equal to the optimal value determined in Sec. 2.4.1 so that $dm = 0$ throughout the analysis. As recalled earlier in this section, it is interesting to study the impact that a deviation from the optimal value of m would have on ϵ_{tot}. The objective here is to determine if the information contained in the look-up table could be reliably summarized in an analytical expression. This would indeed facilitate the implementation and, in general, allow the use of the model without having to generate or download the look-up table. It is however likely that if a simple analytical expression to summarize the look-up table exists, it introduces a deviation dm from the optimal value contained in the table. In view of the relative errors obtained in Tab. 2.1 and Tab. 2.2 when modeling $\tilde{x}_{max}$ and $\Delta \mathrm{Ti}_{k,absmax}$, it seems reasonable to assume a relative error with respect to the look-up table value between -20% and +20%. Assuming that all terms in Eq. 2.53 remain unchanged, the term

$$T_4 = \Delta \mathrm{Ti}^{RANS}_{k,absmax}\, B\, f_N(\tilde{x}/\tilde{x}_{max}) \tag{2.57}$$

can be added to the right-hand side of the equation to account for the effect of dm on ϵ_{tot}. For each combination of C_T and Ti^0_k, the relative errors ϵ^-_{tot} and ϵ^+_{tot} are then computed, respectively for a relative discrepancy on the value of m of -20% and of $+20\%$. The resulting values of ϵ_{tot} are eventually shown in Fig. 2.11. Worth mentioning is that, with respect to Fig. 2.10, the scale of the axes has been modified and the three terms T_1, T_2, T_3 removed for clarity.

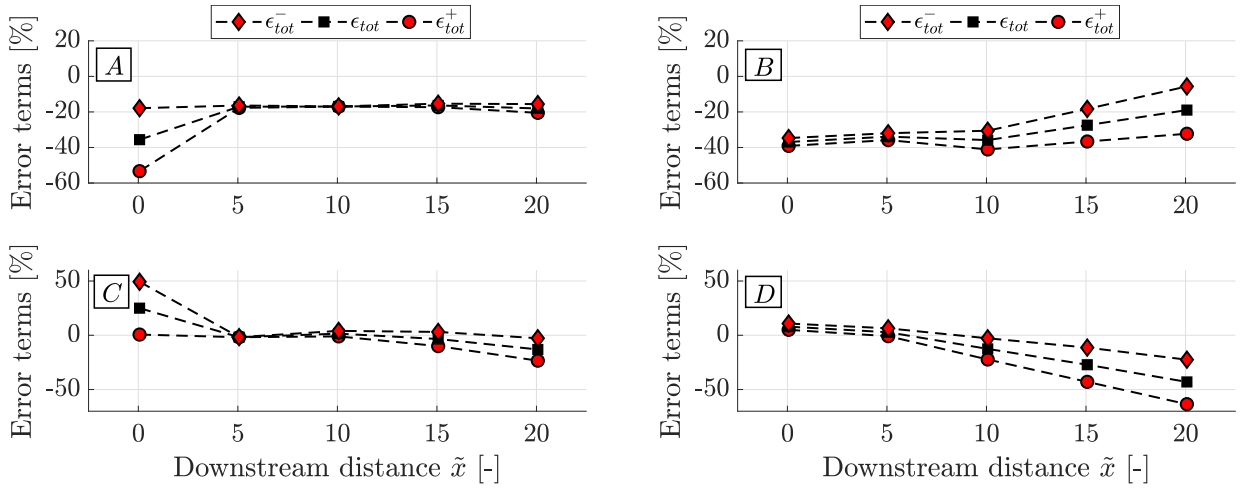

Figure 2.11: Analysis of the evolution of the relative errors ϵ^-_{tot}, ϵ_{tot} and ϵ^+_{tot} with downstream distance $\tilde{x}$ under different values of C_T and Ti^0_k detailed in Tab. 2.4. The relative errors ϵ^-_{tot} and ϵ^+_{tot} are computed for a relative error on m of -20% and of $+20\%$ respectively.

For the standard operational and flow conditions represented by case C (*i.e.*, $C_T = 0.8$ and $\mathrm{Ti}^0_k = 0.05$), Fig. 2.11 explicitly shows that a modelling error on m would have little impact on the the global relative error ϵ_{tot} between $\tilde{x} = 5$ and $\tilde{x} = 10$ behind the rotor. Before and

after this region, it can be seen that large discrepancies are introduced by the deviation dm with respect to the optimal value of m. The resulting relative errors on the model appear to be as large as $\epsilon_{tot} \simeq 50\%$ in the near wake and about $\epsilon_{tot} \simeq -25\%$ in the far wake. At large incoming turbulence intensities and usual values of the thrust coefficient (i.e., case D), it is observed that a relative error of $+20\%$ on m would lead to a relative error of up to $\epsilon_{tot} = -65\%$ in the far wake. Similar results are shown at low values of the thrust coefficients *i.e.*, cases A and B, for which the relative error of $+20\%$ on m again tends to increase the resulting relative error on the global model. By contrast, a relative difference of -20% on m appears to reduce the amplitude of ϵ_{tot} in most situations. One idea that stems from this observation would be to replace the look-up table by an analytical expression, the predictions of which never exceed the reference values contained in the look-up table. However, this would lead to large errors in the near wake region as shown in Fig. 2.11 at $\mathrm{Ti}_k^0 = 0.05$ and $C_T = 0.8$. Given the high sensitivity of the added turbulence model to the value of the m parameter, no substitute to the look-up table is further studied in the scope of this work. At this stage of the model development, it is indeed advisable to prioritize the options that lead to the lowest possible error, in this case the use of the m look-up table.

As a conclusion, the thorough sensitivity analysis carried out in this section first allowed to shed light on the origin of the relative error ϵ_{tot} on the added turbulence model. In particular, four different sets of flow conditions have been investigated. It was shown that, for all the tested conditions, the values of the relative errors on the peak position $\tilde{x}_{max}$, on the peak amplitude $\Delta\mathrm{Ti}_{k,absmax}$ and on the shape function f_N were never amplified by the model. For most conditions Eq. 2.54 was observed to provide a good estimation of the bound of the relative error met along $\tilde{x}$. The sensitivity analysis then allowed to justify the choice of the numerical steps $d\psi$ and $d\lambda$ used in the optimization processes in Sec. 2.3.1 and Sec. 2.4.1. Finally, the question of whether the lookup table for parameter m could be replaced by a more convenient expression was investigated. From this last analysis, it appeared that such an expression would likely have a non-negligible impact on the reliability of the added turbulence model. For that reason, the decision was made not to investigate further attempts to replace the m look-up table by an analytical law in the scope of this work.

Chapter 3

Single wake modelling: Determination of the two-dimensional profiles of the velocity deficit and the added turbulence intensity.

3.1 Modelling of the two-dimensional velocity deficit profile

3.1.1 Initial form of the Bastankhah and Porté-Agel velocity deficit model

As stated in Sec. 1.4, the development of a comprehensive two-dimensional single wake model requires to study both the velocity deficit and the added turbulence intensity profiles. In this section, the focus is placed on the modelling of the velocity deficit profile and its evolution with downstream distance under different flow conditions. It is worth remembering that the main purpose of this section is to eventually propose a velocity deficit model that could be used as an alternative to the RANS look-up table introduced in Sec. 1.3.

In contrast to the added turbulence models for which the literature provides only a very limited amount of work to date, many velocity deficit models have been studied over the past decades. Therefore, a good starting point in the development of a velocity deficit model would be to compare the existing models to the look-up table RANS data. Similar to what was done in Section Sec. 2.1.2 when comparing added turbulence models, several deficit models could be tested against the RANS predictions. However, it seems that among the models introduced in Sec. 1.2.1, the LES-validated Bastankhah and Porté-Agel model [15] is the most suitable in the context of this work. At hub height, this two-dimensional model gives:

$$\frac{\Delta U}{U_\infty} = \left(1 - \sqrt{1 - \frac{C_T}{8\,(\sigma/D)^2}}\right) \exp\left(-\frac{y^2}{2\sigma^2}\right). \tag{3.1}$$

In this expression, D denotes the diameter of the rotor, U_∞ the undisturbed flow and ΔU the velocity deficit caused by the turbine operating at a thrust coefficient C_T. As explained earlier in Sec. 1.2.1, the velocity deficit tends to decrease as the downstream distance x increases due to the wake recovery phenomenon. Therefore, the evolution of the standard deviation σ with x is modelled by Bastankhah and Porté-Agel [15][1] as

$$\sigma = k\,x + \varepsilon\,D \quad \text{with} \quad k \simeq \alpha_1 I + \alpha_2 \quad \text{and} \quad \varepsilon = 0.2 \times \left(\frac{1+\sqrt{1-C_T}}{2\sqrt{1-C_T}} \right)^{0.5}, \tag{3.2}$$

where α_1 and α_2 are two coefficients that have been calibrated over the range $0.06 < I < 0.15$ at $C_T = 0.8$. From this calibration, the values are set to $\alpha_1 = 0.38$ and $\alpha_2 = 0.004$. Note that the notation I is equivalent to Ti_u and refers to the incoming streamwise turbulence intensity defined in Eq. 1.7. Attention should also be paid to the fact the standard deviation σ, that characterises the width of the wake, is assumed to grow linearly as one moves away from the rotor. In particular, the wake expansion coefficient k is a key parameter in Bastankhah and Porté-Agel [15] model as it impacts both the deficit amplitude and the growth of the wake. For this purpose, it seems natural that the parameter k takes larger values for increasing levels of initial streamwise turbulence I. Moreover, under the strong assumption that the wake profile is axisymmetric, the crosswind distance y in Eq. 3.1 can be replaced by the radial distance r. Doing so, Eq. 3.1 together with Eq. 3.2 then describe a three-dimensional axisymmetric wake. In the rest of this section, the discussion is however carried out based on the two-dimensional velocity deficit profile at hub height provided by Eq. 3.1.

In view of comparing the performance of Bastankhah and Porté-Agel [15] deficit model to the predictions of EllipSys stored in the look-up table, two quantities of interest are defined. First, the characteristic wake half-width $r_{1/2}$ as defined in Lingkan and Buxton [19], *i.e.* half the lateral distance between two points with a value that is half of the center-line amplitude, can be computed from a Gaussian profile of standard deviation σ as:

$$r_{1/2} = \sigma\sqrt{2\ln(2)}. \tag{3.3}$$

This simple way of characterizing the width of the wake has been extensively used in the literature (Bastankhah and Porté-Agel [38], Qian and Ishihara [24]). The second parameter of interest discussed in this section is the center-line deficit ΔU_{max}, *i.e.* the amplitude of the Gaussian curve of the velocity deficit. In Bastankhah and Porté-Agel [15], it is evident that this quantity is related to Eq. 3.1 as:

$$\Delta U_{max} = U_\infty \left(1 - \sqrt{1 - \frac{C_T}{8\,(\sigma/D)^2}} \right). \tag{3.4}$$

For any given combination of C_T and Ti_k^0 values, the predictions of Bastankhah and Porté-Agel [15] are computed according to Eq. 3.2, Eq. 3.3 and Eq. 3.4. It is noteworthy to mention

[1]The relationship between I and k was anticipated by Bastankhah and Porté-Agel [15] but explicitly formulated in the work of Niayifar and Porté-Agel [17]

that the value of the initial streamwise turbulence intensity Ti_u^0 (denoted I in Eq. 3.2) should be retrieved from Ti_k^0 using the standard ratios of atmospheric turbulence, *i.e.*, $\mathrm{Ti}_u^0 = 1.25 \times \mathrm{Ti}_k^0$, as discussed in Sec. 1.3. It has been observed that, if this step were to be omitted, the fidelity of the Bastankhah and Porté-Agel [15] model would be significantly impacted. In parallel, the RANS values of the wake half-width ($r_{1/2}^{RANS}$) and of the deficit amplitude (ΔU_{max}^{RANS}) are extracted from the look-up table for the same flow conditions. However, it important to keep in mind that the RANS data have been generated in EllipSys over a discrete grid, as explained in Sec. 1.3. Therefore, for a given downstream distance, it is likely that no grid point is located at the very particular lateral position where half of the deficit amplitude is reached. The resulting half-width $r_{1/2}^{RANS}$ would thus be computed from the lateral position of the node at which the deficit is the closest to half of the maximum deficit amplitude. In other words, one can anticipate the value of $r_{1/2}^{RANS}$ to be inevitably marred by an error related to the spatial step used to generate the grid. Even though the impact of this error on the value of $r_{1/2}^{RANS}$ has not been further investigated, a more robust alternative is proposed. The idea of this second approach is, for all tested conditions and downstream distances, to fit a Gaussian law of standard deviation $\sigma^{RANS}(C_T, \mathrm{Ti}_k^0, x)$ and amplitude $\Delta U_{max}^{RANS}(C_T, \mathrm{Ti}_k^0, x)$ to the RANS data points. In order to retrieve the optimal value of these two parameters, different amplitudes $\Delta U'_{max}$ and standard deviations σ' are considered. For each tested pair of U'_{max} and σ', an error

$$\varepsilon_{fit} = \sum_{i=-N/2}^{N/2} |\Delta U'_{max} \exp\left(\frac{-y_i^2}{2(\sigma')^2}\right) - \Delta U^{RANS}(y_i)| \tag{3.5}$$

is computed over a set of $N+1$ lateral grid points. The quantity ΔU^{RANS} denotes the velocity deficit at hub height stored in the RANS look-up table. The pair σ^{RANS} and ΔU_{max}^{RANS} is then defined as the one for which the minimum value of ε_{fit}, denoted ε_{fit}^{min}, is obtained. Eventually, the value of the optimal standard deviation σ^{RANS} is converted into the wake half-width $r_{1/2}^{RANS}$ using Eq. 3.3.

In Fig. 3.1, the values of the wake half-widths, computed from Bastankhah and Porté-Agel [15] are compared to the ones extracted from the RANS look-up table. The results are normalized by the rotor radius $D/2$ and plotted against the normalized downstream distance $\tilde{x} = x/D$ for three values of Ti_k^0 at three different operating conditions. In general, Fig. 3.1 shows excellent agreement for all thrust coefficients provided that the incoming turbulence intensity is low. This is by no means a surprise given the range of streamwise turbulence intensity ($0.06 < I < 0.15$ or equivalently $0.048 < \mathrm{Ti}_k^0 < 0.12$) over which the Bastankhah and Porté-Agel [15] model has been calibrated. At $\mathrm{Ti}_k^0 = 0.05$, Fig. 3.1 clearly shows evidence of the linear growth of the wake, for which the expansion coefficient k defined in Eq. 3.2 provides an excellent estimation. This linear behavior however tends to be less pronounced as Ti_k^0 increases. In particular, for $C_T = 0.1$ and large Ti_k^0, the values of the wake half-width $r_{1/2}^{RANS}$ extracted from the RANS look-up table become unpredictable and irregular. This observation can be easily explained by the very low amplitude of the deficit observed for the same conditions in Fig.3.2. Indeed, as explained several times throughout this work, strong incoming turbulence favors wake recovery and therefore the rapid disappearance of the wake. This is all the more pronounced when the velocity gradients at the rotor are low, i.e. for low values of

C_T. Therefore, the irregular cases pointed out above are justified by the extreme flatness of the velocity deficit, for which no clear value of the standard deviation can be determined. To a lesser extent, the same explanation applies to Fig. 3.2, in which the amplitude is observed to slightly fluctuate for $C_T = 0.1$. At $C_T = 0.8$, the momentum extracted by the turbine is maximum and leads to large velocity gradients in the wake. In addition, if there is only little mixing with the undisturbed flow, *e.g.* for $\mathrm{Ti}_k^0 = 0.05$, it is possible that the Bastankhah and Porté-Agel [15] model predicts complex values of the velocity deficit in the near wake. In this situation, the spurious values are set to the theoretical maximum deficit, *i.e.*, $\Delta U_{max} = U_\infty$. However, this assumption corresponds to a full blockage of the flow and is clearly not verified in practice. In general, it can be concluded from Fig.3.2 that the predictions of the Bastankhah and Porté-Agel [15] model should not be trusted blindly in the near wake.

Although the analysis of Fig. 3.1 and Fig. 3.2 allows to assess the performances of the Bastankhah and Porté-Agel [15] model in a wide variety of conditions, no information on the quality of the Gaussian fitting can be retrieve from those graphs. Therefore, the RANS data points and the corresponding fitted Gaussian curves are represented in Fig. 3.3, together with the two-dimensional velocity deficit profile predicted by Eq. 3.1. The excellent estimations of both the wake half-width and the deficit amplitude provided by Bastankhah and Porté-Agel [15] are notable for $\tilde{x} \geqslant 3$ in Fig. 3.3a. Below this distance, a top-hat profile, symptomatic of the near wake region behind a rotor operating at high thrust coefficients, is clearly observed. In particular, the portion of the wake located close to the axis of the rotor appears to be subject to fewer velocity deficit. In practice, this is justified by the fact that very little momentum is dissipated by the viscous forces at the hub compared to the momentum deficit caused by the blades. It is however possible that the low deficit observed at $\tilde{x} = 1$ in Fig. 3.3a is slightly underestimated since the hub is simply modelled as a circular hole at the center of the force actuator disk used in EllipSys. In other words, no viscous friction with the surface of the hub is accounted for in the RANS simulations, causing the air to freely flow through the central section of the actuator disk. Even though the top-hat profile is rapidly smoothed by the diffusion of momentum as $\tilde{x}$ increases, the fitted Gaussian curve does not provide a reliable modelling of the near wake in Fig. 3.3a. At $C_T = 0.8$ and $\mathrm{Ti}_k^0 = 0.3$, Fig. 3.3b shows large discrepancies between the modelled profiles and the actual RANS values. This result appears to be consistent with the important modelling errors that have been observed in both Fig. 3.1 and Fig. 3.2 for $C_T = 0.8$ and $\mathrm{Ti}_k^0 = 0.3$. Contrary to the top-hat velocity deficit profile shown in the near wake in Fig. 3.3a, the large initial turbulence intensity $\mathrm{Ti}_k^0 = 0.3$ allows to recover a Gaussian curve faster as evidenced in Fig. 3.3b. In the same figure, the wake recovery phenomenon enhanced by the large value of Ti_k^0 can clearly be observed.

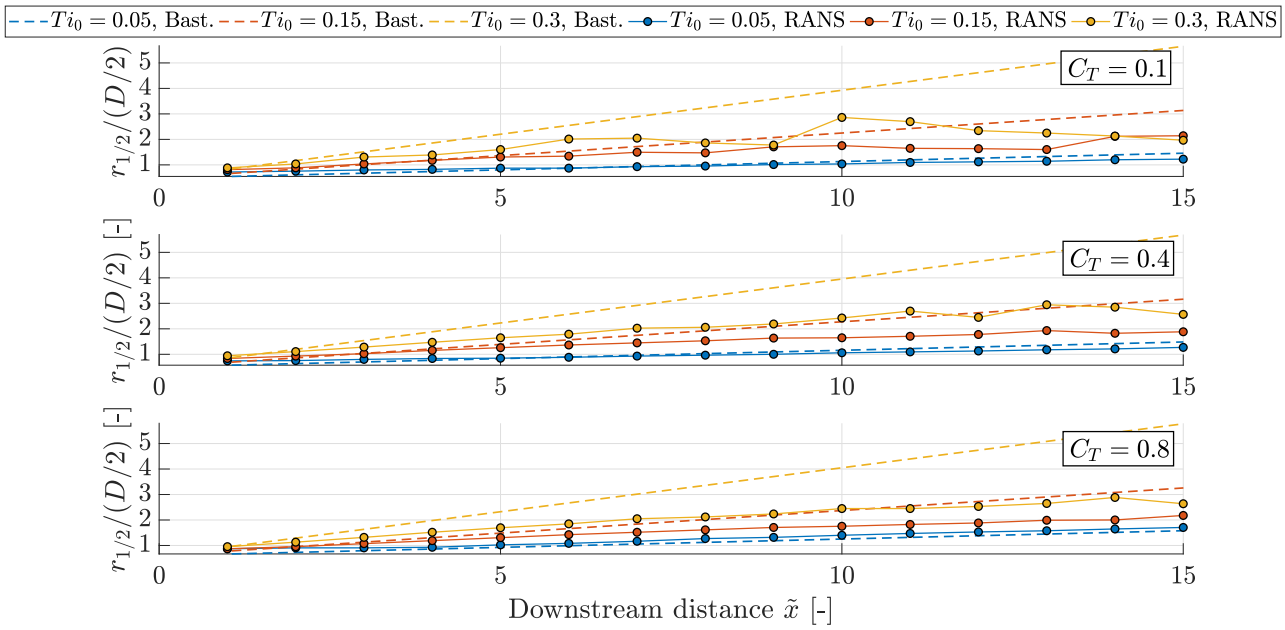

Figure 3.1: Comparison of the streamwise evolutions of the wake half-width $r_{1/2}$ derived from Eq. 3.2 and the wake half-width $r_{1/2}^{RANS}$ recovered from the RANS look-up table under different flow conditions.

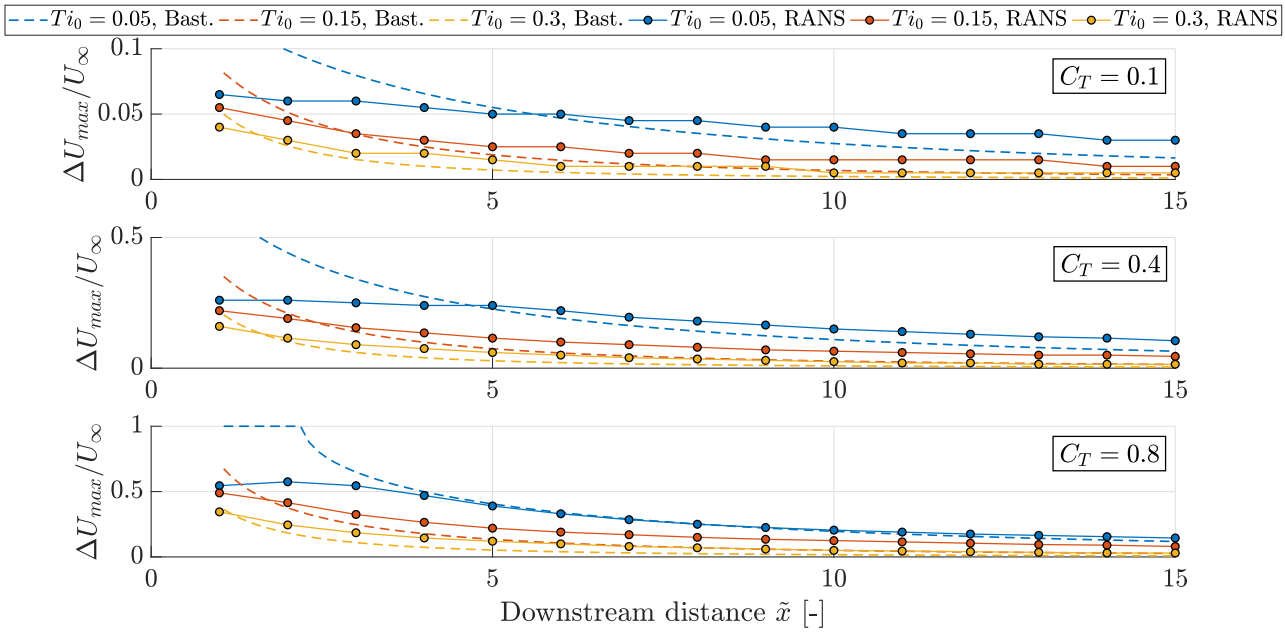

Figure 3.2: Comparison of the streamwise evolutions of the amplitude of the velocity deficit ΔU_{max} derived from Eq. 3.4 and the amplitude ΔU_{max}^{RANS} recovered from the RANS look-up table under different flow conditions. The scale of the vertical axis is adapted in each case for readability.

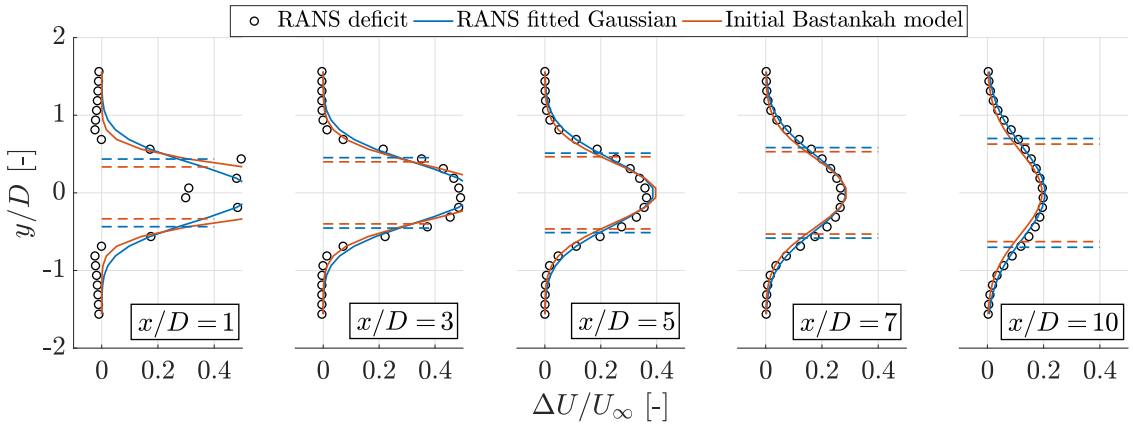

(a) $C_T = 0.8$ and $\mathrm{Ti}_k^0 = 0.05$ [-]

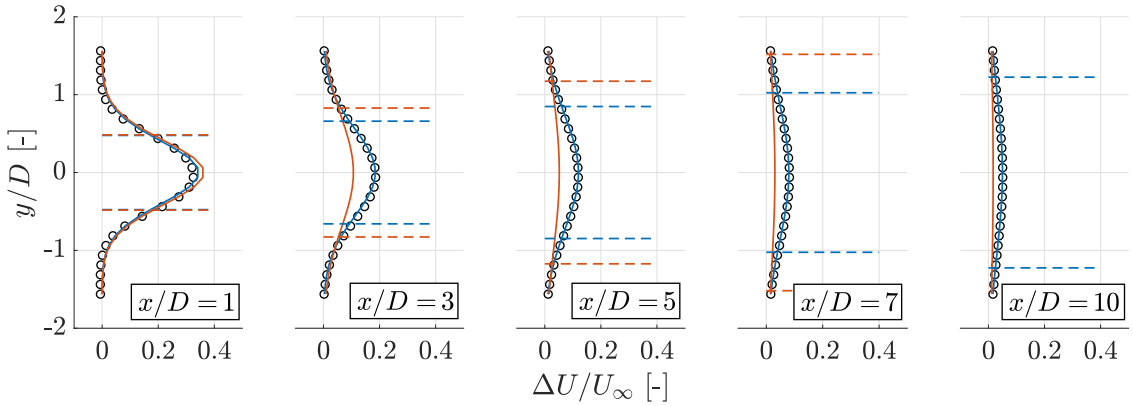

(b) $C_T = 0.8$ and $\mathrm{Ti}_k^0 = 0.30$ [-]

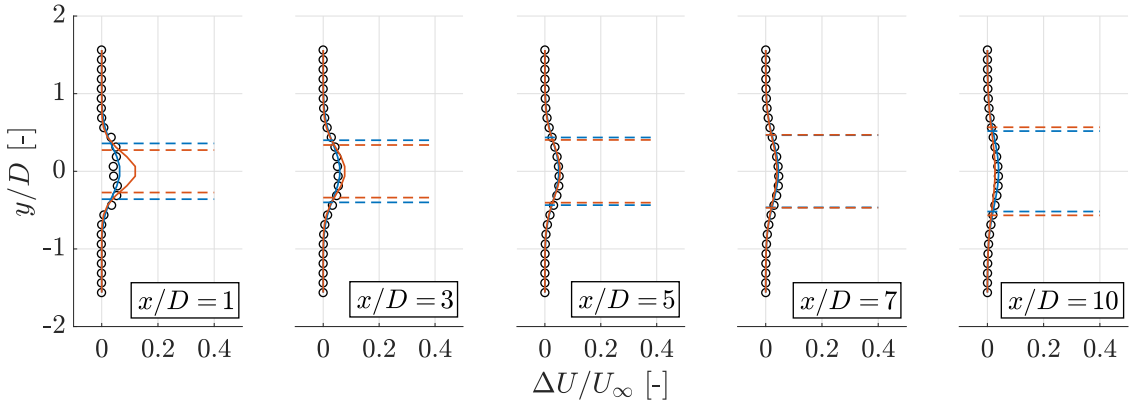

(c) $C_T = 0.1$ and $\mathrm{Ti}_k^0 = 0.05$ [-]

Figure 3.3: Streamwise evolution of the two-dimensional velocity deficit profile under different flow conditions. The predictions of the initial Bastankhah and Porté-Agel [15] model are compared to the Gaussian curve fitted to the RANS data. Both the modelled wake half-width $r_{1/2}$ and the RANS wake half-width $r_{1/2}^{RANS}$ are represented as dashed lines in the figure.

Eventually, the academic situation in which a turbine would operate at $C_T = 0.1$ is discussed based on the results of Fig. 3.3c. As expected, the rotor is shown to have very little impact on the flow. It can be observed that the low velocity gradients do not allow an efficient diffusion of momentum from the undisturbed flow towards the wake. Indeed, in contrast to the case represented in Fig. 3.3a for the same value of $\mathrm{Ti}_k^0 = 0.05$, Fig. 3.3c shows a significantly slower recovery of the wake. Despite small velocity gradients, the deficit profile still appears to be irregular in the near wake due to the little mixing with the undisturbed flow ($\mathrm{Ti}_k^0 = 0.05$). As soon as the profile becomes reasonably Gaussian ($\tilde{x} > 3$), Eq. 3.1 provides an excellent approximation of it, suggesting that the Bastankhah and Porté-Agel [15] model can be reliably used over a large range of C_T values.

It should be remembered, that the model discussed in this section is intended to be used in parallel with superposition methods, for which the incoming turbulence intensity of a downstream turbine is the turbulence in the wake of the upstream turbines. Therefore, it is necessary to ensure that the results of the single wake velocity deficit model remain reliable even for large values of incoming turbulence. Moreover, the initial calibration of the parameters $\alpha_1 = 0.38$ and $\alpha_2 = 0.004$ was performed with respect to the streamwise turbulence intensity I and therefore requires the use of the conversion $I = 1.25 \times \mathrm{Ti}_k^0$, suggested by the standard ratio of atmospheric turbulence (Eq. 1.8). This ratio being roughly assumed equal to one in Sec. 1.3, the streamwise incoming turbulence of the downstream turbines cannot be precisely determined.For those two reasons, the decision was made to re-calibrate the values of the α_1 and α_2 parameters with respect to the RANS data set so as to express Eq. 3.2 directly in terms of Ti_k^0.

3.1.2 Re-calibration of the Bastankhah and Porté-Agel velocity deficit model

Before going any further into the development of the calibration process of α_1 and α_2, it is important to recall that the assumption of a Gaussian velocity deficit profile is not always verified. In particular, the analysis of the RANS data set carried out in Sec. 3.1.1 showed that a Gaussian curve generally fails to describe the velocity deficit top-hat profile observed in the near wake. In this region, the wake half-width $r_{1/2}^{RANS}$ and the amplitude ΔU_{max}^{RANS}, computed as the parameters of the fitted Gaussian law (Eq. 3.5), are spurious data that should thus not be accounted for when re-calibrating α_1 and α_2. Furthermore, the wake recovery phenomenon is so that the amplitude of the velocity deficit becomes negligible at some point in the far wake. It was shown in Fig. 3.3 that the downstream position where it occurs strongly depends on the flow conditions. Beyond this downstream position, Fig. 3.1 and Fig. 3.2 have shown that the values of $r_{1/2}^{RANS}$ and ΔU_{max}^{RANS} tend to fluctuate and should therefore be neglected in the re-calibration process.

In light of these considerations, the region $\tilde{x}_0 < \tilde{x} < \tilde{x}_f$ in which the re-calibration can be performed should be clearly identified prior to investigating different values of α_1 and α_2. First, the maximum downstream distance $\tilde{x}_f$ of the domain of interest is arbitrarily defined as the first downstream position at which the amplitude $\Delta \mathrm{U}_{max}^{RANS}$ reaches a value lower than 5% of

the undisturbed flow velocity U_∞. Then, the lower bound $\tilde{x}_0$ is selected as the first downstream position for which the following expression is verified:

$$\varepsilon_{fit}^{min}(C_T, \mathrm{Ti}_k^0, \tilde{x}_0) \leqslant \Delta U_{max}^{RANS}(C_T, \mathrm{Ti}_k^0, \tilde{x} = 1), \tag{3.6}$$

where ε_{fit}^{min} is the sum along the lateral direction of the errors between the RANS data points and the corresponding fitted Gaussian (Eq. 3.5). In other words, for each tested combination of C_T and Ti_k^0, the downstream distances of interest are those for which the quantity ε_{fit}^{min} does not exceed the deficit amplitude computed one diameter behind the rotor. Alternatively, the expression

$$\varepsilon_{fit}^{min}(C_T, \mathrm{Ti}_k^0, \tilde{x}_0) \leqslant \Delta U_{max}^{RANS}(C_T, \mathrm{Ti}_k^0, \tilde{x} = \tilde{x}_0) \tag{3.7}$$

was proposed but appeared to be too restrictive in all the situations for which the amplitude of the deficit is small. Using the definition of $\tilde{x}_0$ provided by Eq. 3.6, the calibration procedure of α_1 and α_2 over $C_T \in [0.1; 0.8]$ and $\mathrm{Ti}_k^0 \in [0.04; 0.4]$ can be summarized as follows:

- First, a pair of tested values α_1^i and α_2^j is selected.
- For each combination of C_T, Ti_k^0 and $\tilde{x}$, the standard deviation following the Bastankhah and Porté-Agel [15] model is recovered:

$$\sigma^{ij}/D = k^{ij}\,\tilde{x} + \varepsilon \quad \text{with} \quad k^{ij} \simeq \alpha_1^i \mathrm{Ti}_k^0 + \alpha_2^i, \tag{3.8}$$

  where ε is the parameter defined in Eq. 3.2. Attention is drawn to the fact that the wake expansion coefficient k^{ij} is now defined as a function of Ti_k^0. This contrasts with the initial definition of k provided in Eq. 3.2 and for which the streamwise turbulence intensity Ti_u was used.

- The values of the standard deviation $\sigma^{RANS}(C_T, \mathrm{Ti}_k^0, \tilde{x})$ retrieved from the fitted Gaussian laws are then used to compute the quantity ε_σ defined as:

$$\varepsilon_\sigma(\alpha_1^i, \alpha_2^j) = \sum_{C_T} \left(\sum_{\mathrm{Ti}_k^0} \left(\sum_{\tilde{x}=\tilde{x}_0(C_T, \mathrm{Ti}_k^0)}^{\tilde{x}_f(C_T, \mathrm{Ti}_k^0)} |\sigma^{ij} - \sigma^{RANS}| \right) \right). \tag{3.9}$$

  The procedure is then repeated for all the tested pairs of α_1^i and α_2^j.

- Eventually, the pair of calibrated parameters for which the quantity ε_σ is minimum is retained.

In practice, this procedure can easily be implemented using multi-dimensional matrix operations. The resulting values of the re-calibrated coefficients α_1 and α_2 (initially equal to 0.380 and 0.0040, respectively) are found to be:

$$\alpha_1 = 0.264 \quad \text{and} \quad \alpha_2 = 0.0126. \tag{3.10}$$

Similarly to what was done in Sec. 3.1.1, the performance of this re-calibrated model can be evaluated and compared to that of the original Bastankhah and Porté-Agel [15] model. At

this point, it is worth recalling that the objective is to obtain a model of the velocity deficit as a function of Ti_k^0, the predictions of which have to remain faithful to the RANS data even for strong incoming turbulence intensities. As it has been said before, the calibration of the parameters α_1 and α_2 is performed on the interval $C_T \in [0.1; 0.8]$ so that the re-calibrated model is general enough to replace all the cases contained in the look-up table. In Niayifar and Porté-Agel. [17]), it is however specified that the wake expansion coefficient k depends not only on the atmospheric turbulence level but also on the operating conditions (*i.e.*, the C_T value) of the turbine. For this reason, Niayifar and Porté-Agel al. [17] emphasize the need to determine in the future a law for k that is both a function of Ti_k^0 and C_T. In this work, the initial form of the expression of k is kept for the sake of simplicity and the impact of the different values of C_T is thus accounted for through the re-calibration of α_1 and α_2.

Given the form of Eq. 3.1, it is clear that any modelling error on σ will impact both the predicted wake half-width and the amplitude of the velocity deficit. It is therefore difficult to distinguish whether an error in the re-calibrated model is due to the form of the analytical expression Eq. 3.1 or to an inaccuracy in the modelled value of σ. This distinction can nevertheless be made by studying in parallel the amplitude ΔU^R defined by:

$$\frac{\Delta U^R}{U_\infty} = \left(1 - \sqrt{1 - \frac{C_T}{8\,(\sigma^{RANS}/D)^2}}\right) \exp\left(-\frac{y^2}{2(\sigma^{RANS})^2}\right). \tag{3.11}$$

In this expression, referred to as the unbiased Bastankhah and Porté-Agel model, the standard deviation of the fitted Gaussian is used to remove the effect of any modeling error on σ. As a result, it can be expected that any discrepancy observed between the fitted Gaussian and the unbiased Bastankhah and Porté-Agel model is due to the analytical form of the model.

The results of the calibration procedure are explicitly shown in Fig. 3.4a and Fig. 3.4b for the common operating regime $C_T = 0.8$. To facilitate the analysis of these two figures, the relative error with respect to the RANS data is calculated for the original Bastankhah and Porté-Agel [15] model, for its unbiased version, and for the re-calibrated model. These models are respectively denoted by "I.B.", "U.B." and "C.B.". The values of the relative errors are summarized in Tab. 3.1 for three downstream distances and three initial turbulence levels. Note that for model "U.B." in Tab. 3.1a, the relative error is by definition zero as the RANS fitted values of the wake half-width are used as such in the unbiased Bastankhah and Porté-Agel model. Eventually, as discussed earlier, the RANS data $r_{1/2}^{RANS}$ and ΔU_{max}^{RANS} recovered from the fitted Gaussian laws cannot be fully trusted out of the region $\tilde{x}_0 < \tilde{x} < \tilde{x}_f$. The representation of the RANS data and of the unbiased model (Eq. 3.11) is therefore limited to the reliable interval of downstream distances.

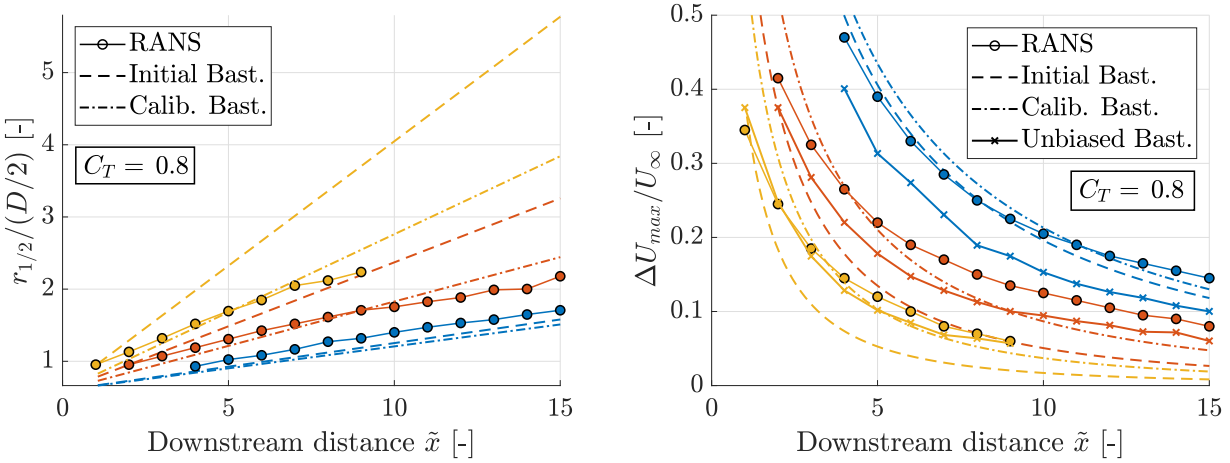

(a) Wake half-width

(b) Velocity deficit amplitude

Figure 3.4: Streamwise evolution of the wake half-width $r_{1/2}$ (a) and of the amplitude of the velocity deficit (b) for $C_T = 0.8$. In both figures, the initial Bastankhah and Porté-Agel [15] model and its re-calibrated version are compared to the RANS fitted parameters $r_{1/2}^{RANS}$ and ΔU_{max}^{RANS}. The amplitudes computed with the unbiased model (Eq. 3.11) are also displayed in figure (b). For both (a) and (b), the blue, red and yellow curves are obtained for an incoming turbulence $\mathrm{Ti}_k^0 = 0.05$, $\mathrm{Ti}_k^0 = 0.15$ and $\mathrm{Ti}_k^0 = 0.30$ respectively.

Table 3.1: Relative error [%] on the wake half-width (a) and on the deficit amplitude (b) with respect to the RANS fitted parameters $r_{1/2}^{RANS}$ and ΔU_{max}^{RANS} at $C_T = 0.8$. For both (a) and (b), "I.B.", "C.B." and "U.B" respectively denote the initial (Eq. 3.1), the re-calibrated, and the unbiased (Eq. 3.11) Bastankhah and Porté-Agel models. Three values of the atmospheric turbulence intensities are tested together with three different downstream distances.

(a) Wake half-width

Ti_k^0	Model	$5D$	$10D$	$15D$
0.05	I.B.	-10	-11	-7
	C.B.	-12	-14	-12
	U.B.	0	0	0
0.15	I.B.	14	35	49
	C.B.	-7	4	12
	U.B.	0	0	0
0.3	I.B.	37	NA	NA
	C.B.	-1	NA	NA
	U.B.	0	0	0

(b) Velocity deficit amplitude

Ti_k^0	Model	$5D$	$10D$	$15D$
0.05	I.B.	4	-4	-18
	C.B.	11	4	-10
	U.B.	-20	-25	-31
0.15	I.B.	-39	-60	-67
	C.B.	-5	-31	-41
	U.B.	-19	-24	-25
0.3	I.B.	-56	NA	NA
	C.B.	-14	NA	NA
	U.B.	-15	NA	NA

From Fig. 3.4a for $\mathrm{Ti}_k^0 = 0.30$ and $\mathrm{Ti}_k^0 = 0.15$, the re-calibrated linear growths are observed

to be significantly closer to the fitted RANS values. The same conclusion holds for the re-calibrated deficit amplitudes as seen in Fig. 3.4b. In a more quantitative manner, Tab. 3.1 shows a considerable reduction of the relative error for C.B., for the case $\mathrm{Ti}_k^0 = 0.15$ at all downstream distances. This was expected as the original calibration does not account for values of I larger than 0.15 (*i.e.* values of Ti_k^0 larger than 0.12). However, it is obvious that this re-calibration cannot simultaneously maintain the excellent performance of the original model observed in Fig. 3.3a for the conditions $\mathrm{Ti}_k^0 = 0.05$. Therefore, Fig. 3.4a shows that calibrating the model over a larger number of flow conditions leads, at $\mathrm{Ti}_k^0 = 0.05$, to slightly larger discrepancies for C.B..This is also reflected in Tab. 3.1a for all tested distances. The relative error obtained for the re-calibrated model remains nevertheless low and thus allows to obtain reliable estimations of the wake half-width over a larger set of incoming turbulence intensities. Similar conclusions can be drawn for the other values of C_T over which the re-calibration has been performed.

In Fig. 3.4b, an unexpected result must be highlighted. Indeed, the unbiased Bastankhah model (Eq. 3.11) in the case $\mathrm{Ti}_k^0 = 0.05$ seems to underestimate the amplitude of the deficit, whereas this same model appears to be in good agreement with the RANS data for the case $\mathrm{Ti}_k^0 = 0.30$. This seems to suggest that the form of the analytical relation proposed by Bastankah and Porté-Agel to link the standard deviation σ to the amplitude of the deficit ΔU_{max} leads to a slight under-prediction of this amplitude, at least in the case $\mathrm{Ti}_k^0 = 0.05$. However, this relation is derived from well-established physical concepts and has shown excellent results when used with a LES data set in Bastankhah and Porté-Agel [15] for $C_T = 0.8$ and $\mathrm{Ti}_k^0 \simeq 0.05$. If the analytical form of this law is not an inherent source of significant error, then it should allow to recover the amplitude ΔU_{max}^{RANS} from the knowledge of the input σ^{RANS}. The origin of this paradox is unclear but seems to be related to the high sensitivity of Eq. 3.1 with respect to σ. Indeed, a slight positive deviation introduced on the value of σ has been observed to lead to a significant underestimation of the corresponding amplitude. Mathematically, this is shown by the expression:

$$d(\Delta U_{max}) \simeq \frac{\partial \Delta U_{max}}{\partial(\sigma/D)}\, d(\sigma/D) = \frac{-\sqrt{2}\, C_T}{4\sqrt{8\,(\sigma/D)^6 - C_T\,(\sigma/D)^4}}\, d(\sigma/D), \tag{3.12}$$

from which it is clear that the sensitivity increases strongly when σ is small, i.e. for low values of Ti_k^0. It is therefore likely that the RANS data σ^{RANS} and U_{max}^{RANS} are in fact subject to a small error compared to a higher fidelity reference, *e.g.*, a set of LES data generated under the same conditions. As a result of Eq. 3.12, the error on σ^{RANS} is strongly amplified when using the unbiased Bastankhah model (Eq. 3.11), causing the discrepancy observed in Fig. 3.4b and Tab. 3.1b for $\mathrm{Ti}_k^0 = 0.05$. Worth mentioning is the fact that this explanation remains hypothetical and should be confirmed by comparing σ^{RANS} and ΔU_{max}^{RANS} with their LES equivalent generated for $C_T = 0.8$ and $\mathrm{Ti}_k^0 = 0.05$. It should be noted that the excellent results obtained by the initial model of Bastankhah and Porté-Agel [15] for the case $\mathrm{Ti}_k^0 = 0.05$ seem to confirm this theory. Indeed, these results are based on the initial calibration performed on a LES data set, specifically for the case $C_T = 0.8$ and over a reduced interval of Ti_k^0 values. The high fidelity of this calibration is shown explicitly in Niayifar et

al.[17]. Hence, it is possible that the wake half-width predicted by the initial Bastankhah and Porté-Agel model˜[**egroup**]BastankhahPorteAgel and slightly lower than $r_{1/2}^{RANS}$ is in reality more reliable than the RANS fitted wake half-width. This explanation would therefore justify the excellent performances of the initial Bastankhah and Porté-Agel model [15] observed in Fig. 3.4b for $\mathrm{Ti}_k^0 = 0.05$.

Eventually, the results of this re-calibration can be assessed in terms of the two-dimensional velocity deficit in Fig. 3.5. Similarly to Fig. 3.4a and Fig. 3.4b, the fitted Gaussian and the corresponding unbiased Bastankhah and Porté-Agel model (Eq. 3.11) is only shown in the interval of downstream distances used in the re-calibration process, *i.e.* $\tilde{x}_0 < \tilde{x} < \tilde{x}_f$. In Fig. 3.5a, it is clear that the beginning of this interval coincides with the end of the so-called top-hat profile ($\tilde{x} > 3$). From the same figure, one can observe the slight overestimation of the deficit amplitude induced by the re-calibrated values of α_1 and α_2 (Eq. 3.10). Moreover, a sensitivity interval is represented in light grey in Fig. 3.5. It is computed following Eq. 3.1, in which $\sigma = \sigma^{RANS} \pm d(\sigma)$ with $d(\sigma)$ equal to 10% the value of σ. Since the computation of the sensitivity interval involves σ^{RANS}, it is shown only in the region where σ^{RANS} is considered reliable, *i.e.* $\tilde{x}_0 < \tilde{x} < \tilde{x}_f$. This representation thus visually supports the high sensitivity of Eq. 3.1 with respect to the parameter σ predicted by Eq. 3.12 earlier in this section. For the conditions $C_T = 0.8$ and $\mathrm{Ti}_k^0 = 0.3$ (Fig. 3.5b), the re-calibrated model does lead to significant improvements for $\tilde{x} > 1$. Below this downstream distance, the wake half-width predicted by the re-calibrated model is barely lower than the RANS data (Fig. 3.4a) but this small discrepancy is strongly amplified by the high sensitivity to σ. Attention should be paid to the case $\tilde{x} = 10$ in Fig. 3.5b, for which the wake is considered fully recovered and therefore disregarded by the re-calibration procedure. Finally, Fig. 3.5c essentially shows that the re-calibration has no significant effect on the model if the thrust coefficient is as low as $C_T = 0.1$. In general, the initial Bastankhah and Porté-Agel model [15] was however observed to be slightly outperformed by its re-calibrated version for all the C_T values between 0.1 and 0.8.

To sum up, a method to reliably retrieve the wake half-width and the deficit amplitude from the velocity field generated in EllipSys was investigated in Sec. 3.1.1. The Bastankhah and Porté-Agel model [15] was then studied as an alternative to the current look-up table model of the velocity deficit. Good agreement was shown between the model (Eq. 3.1) and the RANS fitted data in the conditions for which the model was initially calibrated. In order to extend the range of atmospheric turbulence intensities over which the velocity deficit model matches the RANS data, a re-calibration of the Bastankhah and Porté-Agel model was carried out in Sec. 3.1.2. This re-calibration first allowed to re-write the expression of the wake expansion coefficient k (Eq. 3.2) as a linear function of Ti_k^0, instead of Ti_u^0. Although at the expense of slightly larger amplitude errors for the case $\mathrm{Ti}_k^0 = 0.05$, significant improvements were observed for the re-calibrated model in the event of larger incoming turbulence intensities.

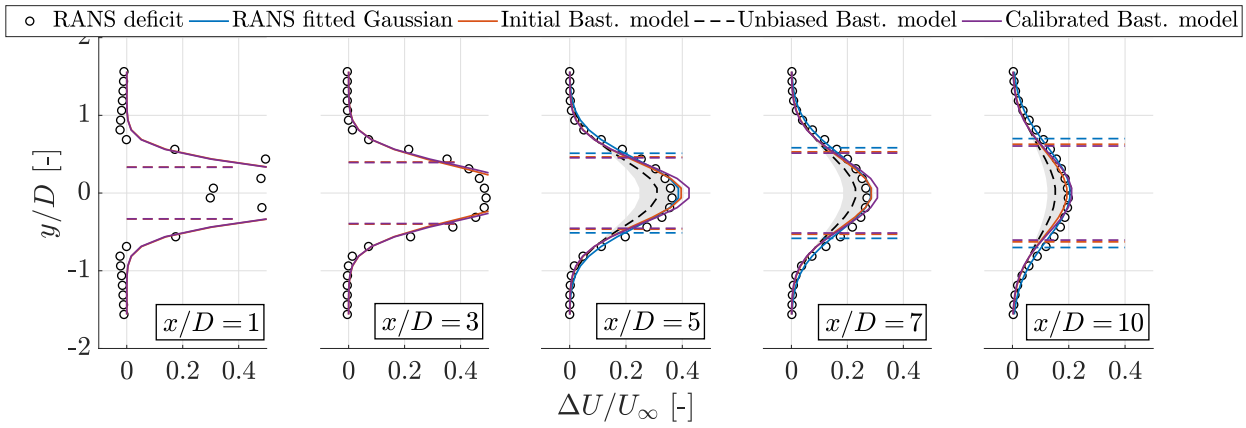

(a) $C_T = 0.8$ and $\mathrm{Ti}_k^0 = 0.05$ [-]

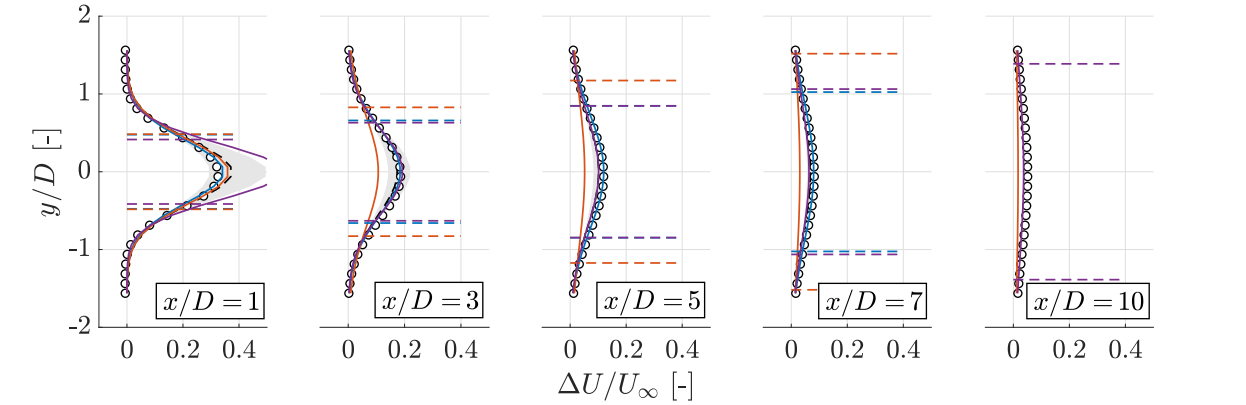

(b) $C_T = 0.8$ and $\mathrm{Ti}_k^0 = 0.30$ [-]

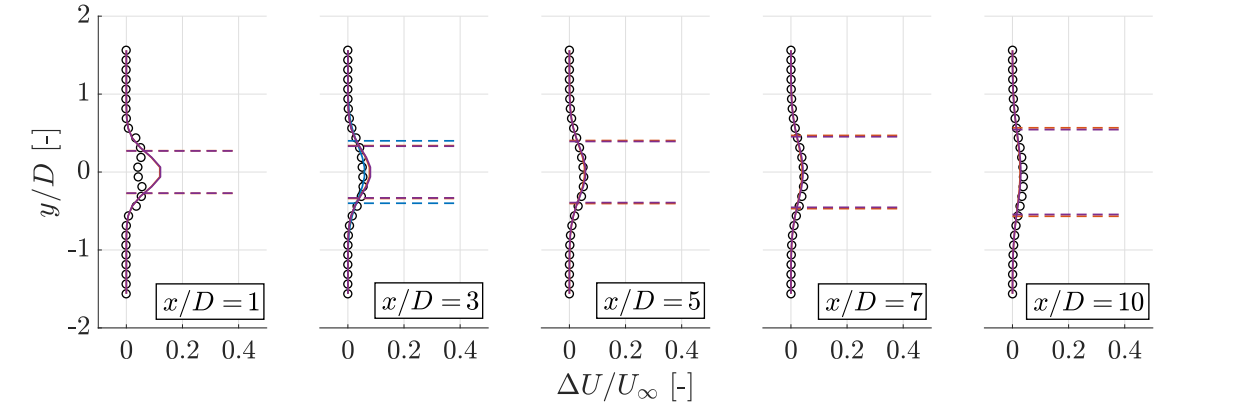

(c) $C_T = 0.1$ and $\mathrm{Ti}_k^0 = 0.05$ [-]

Figure 3.5: Streamwise evolution of the two-dimensional velocity deficit profile under different flow conditions. The predictions of the initial (Eq. 3.1), the unbiased (Eq. 3.11) and the re-calibrated Bastankhah and Porté-Agel models are compared to the Gaussian curve fitted to the RANS data. The initial and the unbiased models are only displayed in the calibration range $\tilde{x}_0 < \tilde{x} < \tilde{x}_f$. A sensitivity interval on σ ($\pm 10\%$) is also shown in this region. The wake half-widths are represented as dashed lines in the figure.

3.1.3 Validity of the axisymmetric velocity deficit assumption

As mentioned earlier in Sec. 3.1.1, the two-dimensional profile of the velocity deficit can easily be generalized in three dimensions under the assumption of an axisymmetric wake. In fact, the PyWake software, in which the model is to be implemented[2], relies on the assumption that the wake is axisymmetric in order to compute the three-dimensional wake and the incoming flow conditions of the downstream turbines. For that reason, it is interesting to assess the validity of this assumption by comparing the predictions of the model to the RANS velocity deficit field, as shown in Fig. 3.6 for $C_T = 0.8$ and $\mathrm{Ti}_k^0 = 0.05$.

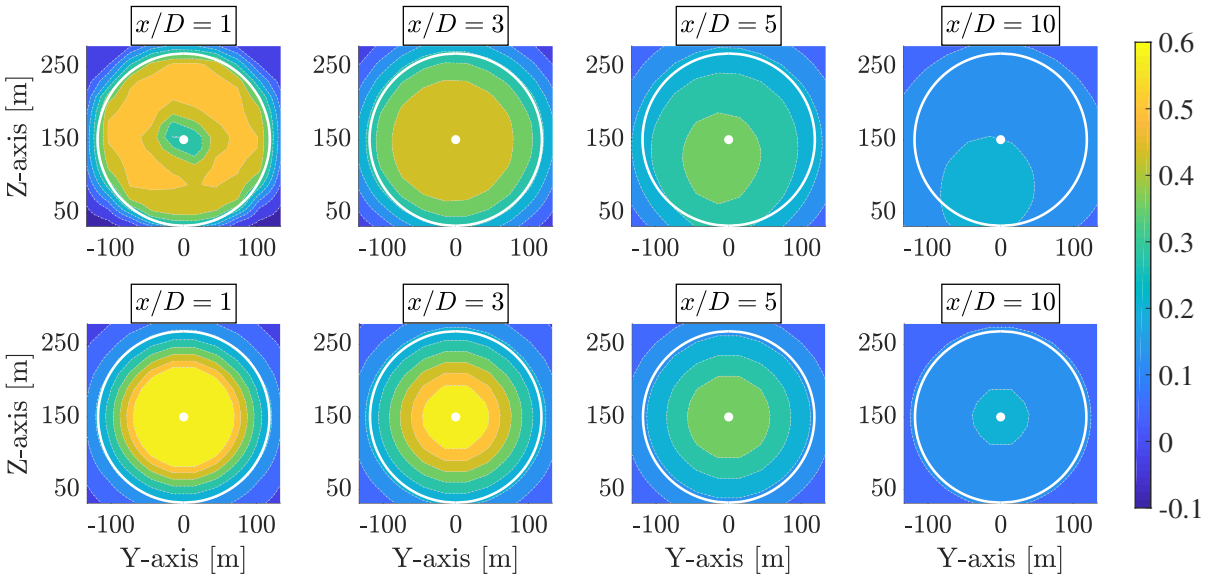

Figure 3.6: Velocity deficit ($\Delta U/U_\infty$) fields in vertical cuts at increasing downstream distances for $C_T = 0.8$ and $\mathrm{Ti}_k^0 = 0.05$. The predictions of the re-calibrated Bastankhah model (lower row) are compared to the RANS data generated by EllipSys (upper row). The perimeter and rotor center are shown in white in the figures.

In the RANS velocity field shown in Fig. 3.6, only slight deviations from an axisymmetric wake are observed for $\tilde{x} \geqslant 5$. In this region, the ground induced boundary layer acts as an additional source of velocity deficit close to the ground so that the total deficit is larger in the lower part of the rotor. Below $\tilde{x} < 5$, the boundary layer still exists but its impact appears to be compensated by the blockage effect of the rotor on the flow. As a matter of fact, the RANS velocity deficit field at $\tilde{x} = 1$ in Fig. 3.6 shows a very clear acceleration, i.e. negative deficit values, of the flow around the turbine. This effect is particularly marked in the lower zone of the figure, since the flow is confined between the ground and the rotor, and therefore accelerates more due to the nozzle effect. As expected, Fig. 3.6 at $\tilde{x} = 1$ shows a strong over-estimation of the deficit amplitude predicted by the re-calibrated Bastankhah and Porté-Agel model. From Fig. 3.4b, it should be recalled that the predicted deficit at the center of the rotor reaches a

[2]since the initial Bastankhah and Porté-Agel model [15] is already included in the software, only the values of the re-calibrated coefficients α_1 and α_2 need to be modified.

unitary value, even though the scale is limited to $\Delta U/U_\infty = 0.6$ for readability. By contrast, the RANS velocity deficit field at $\tilde{x} = 1$ in Fig. 3.6 exhibits interference due to the presence of the hub. Attention should be paid to the fact that EllipSys represents the hub as a central void in the force actuator disk, as mentioned in Sec. 3.1.1. The momentum of the undisturbed air flowing through the center of the disk however quickly diffuses towards the edge of the rotor to such an extent that a Gaussian profile is effectively recovered less than three diameters behind the turbine.

The discussion carried out in this section only focuses on the flow conditions $C_T = 0.8$, $\mathrm{Ti}_k^0 = 0.05$ for brevity. Nevertheless, the same conclusions were seen to hold, although to a different extent, in all the other tested conditions. In particular, the blockage effect tends to disappear when the turbine has little impact on the flow, *i.e.* for low values of the thrust coefficient. The hub interference also seem to vanish more rapidly under high atmospheric turbulent intensity levels, due to the enhanced mixing. To conclude, Fig. 3.6 shows evidence that assuming the velocity deficit field to be axisymmetric is essentially equivalent to neglecting the hub interference, the blockage effect and the presence of the boundary layer. For that reason, the use of the axisymmetric wake assumption for the velocity deficit is retained in the scope of this work.

3.2 Modelling of the two-dimensional added turbulence intensity profile

3.2.1 Generalization of the new one-dimensional model to higher dimensions

In Sec. 1.2, the two-dimensional turbulence intensity profile was introduced. Contrary to the velocity deficit profile, for which the largest deficit is observed along the axis of the rotor, the presence of significant velocity gradients leads to increased turbulence intensity levels at the edge of the wake. Therefore, the simple Gaussian curve proposed in Frandsen [11] appears ill-suited to reliably reflect the physics behind the actual profile of the turbulence intensity in the wake of a wind turbine. Following the approach presented in Lingkan and Buxton [19], a two-term Gaussian function is used to represent the added turbulence intensity profile at each location downstream of the rotor. Assuming that both Gaussian terms have the same amplitude $C_*(x)$ and the same standard deviation $\sigma_*(x)$, the analytical form of the horizontal profile at hub height reads:

$$\Delta \mathrm{Ti}_k(x, y) = C_*(x) \left(\exp\left(-\frac{(y - y_c)^2}{2\,\sigma_*^2} \right) + \exp\left(-\frac{(y + y_c)^2}{2\,\sigma_*^2} \right) \right). \tag{3.13}$$

In this expression, the position of the center-line y_c of each Gaussian term is considered to coincide with the rotor edge, *i.e.* $y_c = D/2$. Lingkan and Buxton [19] justify this assumption based on observations from experimental and numerical studies. It is important to specify that the standard deviation σ_* in Eq. 3.13 is in general different from that of the simple Gaussian

function used to describe the velocity deficit (Eq. 3.1). The wake half-width defined with respect to the added turbulence intensity is denoted $r^*_{1/2}$ and can naturally be written as:

$$r^*_{1/2} = \sigma_* \sqrt{2\,\ln(2)} + y_c, \tag{3.14}$$

with $y_c = D/2$, as proposed by Lingkan and Buxton [19]. Under the axisymmetric wake assumption, replacing the lateral distance y at hub height by the radial distance r allows to re-write Eq. 3.13 in a three dimensional form. Note that the validity of this assumption will later be seen to be challenged by the presence of the ground boundary layer.

Similar to the procedure applied in Sec. 3.1.1, the first step towards the determination of a reliable two-dimensional profile consists in recovering the values of $\sigma_*^{RANS}(C_T, \mathrm{Ti}_k^0, x)$ and $C_*^{RANS}(C_T, \mathrm{Ti}_k^0, x)$ from the values of the added turbulence intensities stored in the RANS look-up table. This is done by fitting the two-term Gaussian law Eq. 3.13 to the set of RANS data for all the considered combinations of C_T, Ti_k^0 and x. In each case, the fitting error

$$\varepsilon_{fit} = \sum_{i=-N/2}^{N/2} \left| C'_* \left(\exp\left(\frac{-(y_i - y_c)^2}{2(\sigma'_*)^2} \right) + \exp\left(\frac{-(y_i + y_c)^2}{2(\sigma'_*)^2} \right) \right) - \Delta\mathrm{Ti}_k^{RANS}(y_i) \right| \tag{3.15}$$

is evaluated for a large number of pairs of C'_* and σ'_* over a set of $N+1$ lateral grid points. Note that in this expression, $\Delta\mathrm{Ti}_k^{RANS}$ refers to the value of the added turbulence intensity stored in the RANS look-up table at hub height. The optimal values of the fitted parameters σ_*^{RANS} and C_*^{RANS} are finally selected such that the fitting error ε_{fit} is minimum.

In Chapter 2, emphasis was placed on the determination of a new model for the amplitude of the added turbulence intensity. The modelling of the corresponding wake half-width has therefore not been considered so far but is a key element in the determination of a two-dimensional profile. In Sec. 1.2.1, the expression Eq. 1.3 proposed by Nygaard [10] for the wake growth was introduced. This model, used in parallel to the Frandsen model (Eq. 1.17) for the amplitude of the added turbulence intensity, appeared to outperform the results obtained under the classical linear wake growth assumption. Moreover, Eq. 1.3 accounts for the local level of turbulence intensity in the wake at each position downstream of the rotor, contrary to Eq. 3.2, in which only the level of turbulence at the rotor position matters. For that reason, Eq. 1.3 seems particularly well-suited to model the evolution of the wake half-width $r^*_{1/2}$ and that of the corresponding standard deviation σ_* (Eq. 3.14) that has to be used in Eq. 3.13. The wake growth TurbOPark model [10] combined to the new model for the amplitude of the added turbulence intensity (Eq. 2.44) leads to the following expression:

$$\frac{dD_w}{dx} = A \sqrt{(\mathrm{Ti}_k^0)^2 + (\lambda\, C_T)^2 \left(\frac{\tilde{x}}{\tilde{x}_{max}} \right)^{2m} \exp\left(2m \left(1 - \frac{\tilde{x}}{\tilde{x}_{max}} \right) \right)}, \tag{3.16}$$

where $D_w = 2\, r^*_{1/2}$ is the diameter of the wake and A a calibration coefficient. The expression of $\tilde{x}_{max}$ and the value of λ are unchanged with respect to Eq. 2.44. Several comments can be made on the form of Eq. 3.16. First of all, considering the local value of the total turbulence

(Ti_k) in the wake and not only the incoming turbulence (Ti_k^0) requires to introduce a method of superposition in the model. Following the recommendation of Nygaard [10], a quadratic superposition method (Tab. 1.1b) is chosen to evaluate the total level of turbulence in the wake. As will be further discussed later in this work, the superposition methods are imperfect and inevitably introduce errors in the modelling of the level of total turbulence intensity Ti_k in the wake. This error is expected to in turns affect the computed value of $r_{1/2}^*$ through Eq. 3.16. Moreover, the right-hand side term of Eq. 3.16 has to be integrated with respect to x to isolate the wake half-width, from which the two-dimensional profile can subsequently be deduced (Eq. 3.14 and Eq. 3.13). All the attempts made so far to perform the integration of Eq. 3.16 analytically have however proved unsuccessful. Although the potential benefit brought by the combination of Eq. 1.3 and the new added turbulence intensity model (Eq. 2.44) is worth further investigation, the decision was made to use a linear law for the streamwise evolution of $r_{1/2}^*$ in the scope of this project. The analytical form proposed by Bastankhah and Porté-Agel [15] for the standard deviation defined with the velocity deficit (σ) is re-written as:

$$\sigma_* = k^* x + \varepsilon\, D \quad \text{with} \quad k^* = \alpha_1^*\, \mathrm{Ti}_k^0 + \alpha_2^* \quad \text{and} \quad \varepsilon = 0.2 \times \left(\frac{1 + \sqrt{1 - C_T}}{2\sqrt{1 - C_T}} \right)^{0.5}. \tag{3.17}$$

Note that this relation assumes that both standard deviations, σ and σ_*, are equal at $x = 0$. Following the methodology introduced in Sec. 3.1.2 for the re-calibration of α_1 and α_2, the calibrated values of α_1^* and α_2^* over $C_T \in [0.1; 0.8]$ and $\mathrm{Ti}_k^0 \in [0.04; 0.4]$ are found to be:

$$\alpha_1^* = 0.248 \quad \text{and} \quad \alpha_2^* = 0.0114. \tag{3.18}$$

Unlike the velocity deficit profile, for which a Gaussian function was suitable in the interval $\tilde{x}_0 < \tilde{x} < \tilde{x}_f$ only, the added turbulence intensity profile appears to be well modelled by a two-term Gaussian function in both the near and far wakes. For that reason, the interval of downstream distances over which the calibration of α_1^* and α_2^* is performed is given by $0 < \tilde{x} < \tilde{x}_f$. The value of $\tilde{x}_f$ is defined for each flow condition as the distance at which the amplitude of the added turbulence intensity (C_*^{RANS}) becomes lower than 0.1%. The two results in Eq. 3.18 appear to be very close to the re-calibrated values $\alpha_1 = 0.264$ and $\alpha_2 = 0.0126$ obtained in Sec. 3.1.2. Hence, modelling σ^* with Eq. 3.17 leads to very little distinction between the wake growth defined with the velocity deficit and that defined with the added turbulence intensity. The importance of this distinction is however highlighted in Lingkan and Buxton [19] and therefore seems to point out imperfections in the modeling of σ^* with Eq. 3.17.

The comparison between the RANS fitted values (σ_*^{RANS}) and the modelled values (σ_*, Eq. 3.17) of the standard deviation is shown in Fig. 3.7. First, it is clear that the offset introduced by $y_c = D/2$ in Eq. 3.14 leads to a significantly larger wake than the one observed in Fig. 3.1. In general, this suggests that the region influenced by the turbulence intensity added by an upstream turbine is wider than the zone in which a velocity deficit is sensed. In contrast to the wake half-width $r_{1/2}^{RANS}$ defined by the velocity deficit and shown in Fig. 3.1, no strong fluctuation of the values of $(r_{1/2}^*)^{RANS}$ is observed in Fig. 3.7. This shows evidence that a two-term Gaussian function provides a more robust fitting than a single term Gaussian curve in the regions where the wake has almost fully recovered. The only notable irregularities in Fig. 3.7

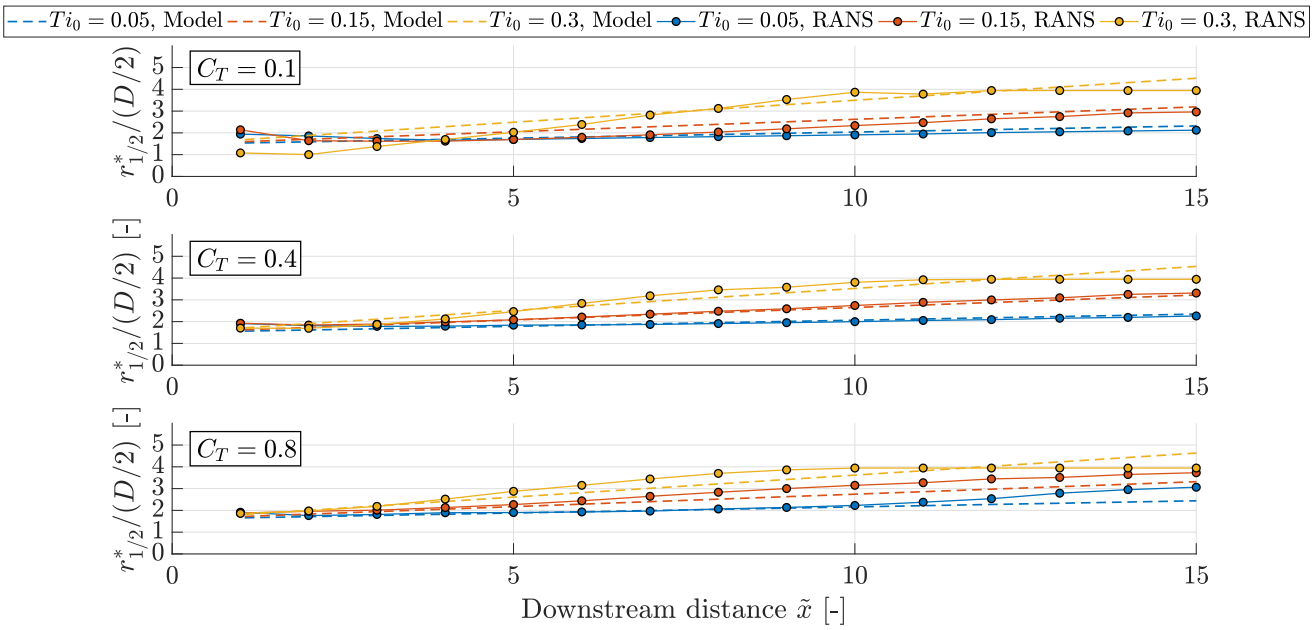

Figure 3.7: Comparison of the streamwise evolutions of the wake half-width $r^*_{1/2}$ derived from Eq. 3.17 and the wake half-width $(r^*_{1/2})^{RANS}$ recovered from the RANS look-up table under different flow conditions.

are observed at downstream distances less than $3D$ for the case $C_T = 0.1$, $\mathrm{Ti}^0_k = 0.3$. Under such conditions, EllipSys predicts a spurious local decrease of the turbulent kinetic energy, k, for a large portion of the profile. The corresponding values of the added turbulence intensity are automatically set to 0 at those locations for consistency with physics. As a result, the two-term Gaussian was observed to reduce to two narrow peaks of incorrect standard deviation and amplitude. Still, those very specific cases correspond to theoretical flow conditions that would hardly be met in practice and will therefore be disregarded in the rest of this analysis.

From Fig. 3.7, it clearly appears that the wake growth as defined by the added turbulence intensity is non-linear. This observation is in agreement with Lingkan and Buxton [19], in which the scaling $r^*_{1/2} \sim x^{1/2}$ seems to be the most appropriate. Nevertheless, approximating the evolution of $r^*_{1/2}$ with a linear function (Eq. 3.17) seems to introduce little errors in the model. For the operating regimes $C_T = 0.1$, $C_T = 0.4$ and $C_T = 0.8$, the relative error on σ_* with respect to σ^{RANS}_* is given in Tab. 3.2a under different turbulent inflow conditions. Note that this quantity is by definition (Eq. 3.14) larger than the corresponding relative error on $r^*_{1/2}$ and is of greater interest in the scope of this analysis due to its direct impact on $\Delta\mathrm{Ti}_k$ (Eq. 3.13). This is in contrast to the standard deviation σ of the Gaussian velocity deficit distribution (Eq. 3.1), for which the relative error given in Tab. 3.1a is the same as for the wake half-width $r_{1/2}$. In Tab. 3.2a, the maximum relative error introduced by the modelling of σ^{RANS}_* as σ_* is 52% for $C_T = 0.1$ and $\mathrm{Ti}^0_k = 0.15$ at $\tilde{x} = 5$. In general, the relative error computed with $C_T = 0.1$ under any turbulent incoming intensities is found to be larger than that computed with more common values of the thrust coefficient, *i.e.* $C_T = 0.8$ and $C_T = 0.4$. Eventually, for

Table 3.2: Relative error [%] on the standard deviation σ_* (a) and on the C_* coefficient (b) with respect to the RANS fitted parameters σ_*^{RANS} and C_*^{RANS} at $C_T = 0.1$, $C_T = 0.4$ and $C_T = 0.8$. Three values of the atmospheric turbulence intensities are tested together with three different downstream distances.

(a) Standard deviation σ_*

Ti_k^0	C_T	$5D$	$10D$	$15D$
0.05	0.1	9	15	18
	0.4	-6	7	7
	0.8	-2	-5	-30
0.15	0.1	52	22	12
	0.4	0.02	-5	-4
	0.8	-7	-19	-15
0.3	0.1	46	-12	20
	0.4	4	-10	21
	0.8	-13	-11	24

(b) Coefficient C_*

Ti_k^0	C_T	$5D$	$10D$	$15D$
0.05	0.1	-1	-6	-8
	0.4	7	-2	-1
	0.8	-12	-7	9
0.15	0.1	-13	-34	-34
	0.4	6	4	4
	0.8	-8	-12	-29
0.3	0.1	-40	-31	-33
	0.4	6	12	10
	0.8	9	-12	-34

those two operating regimes, the relative error on the standard deviation essentially remains between $\pm 20\%$.

In order to tackle the comparison of the amplitudes of the two-dimensional profile, as predicted by the new model (Eq. 2.44) and as recovered from the RANS look-up table, it should be emphasised that Eq. 3.13 reduces to

$$C_*(x) = \frac{\Delta \mathrm{Ti}_k(x, y_c)}{1 + \exp\left(-2\, y_c^2/\sigma_*^2\right)} \tag{3.19}$$

for $y = y_c$. It is indeed crucial to bear in mind that the amplitude $\Delta \mathrm{Ti}_{k,max}$ predicted by the new model (Eq. 2.44) differs, by definition, from the C_* coefficient in Eq. 3.13. Therefore, if the values of $\Delta \mathrm{Ti}_{k,max}$ and σ_* are respectively modelled with Eq. 2.44 and Eq. 3.17, the corresponding C_* coefficient can be computed from Eq. 3.19 and used to generate the two-dimensional added turbulence intensity profile. Eventually, the evolution of the modelled C_* coefficient is compared in Fig. 3.8 to that of the C_*^{RANS} coefficient, retrieved from the two-term Gaussian function fitted to the RANS data. The corresponding relative error is summarized in Tab. 3.2b under different combinations of flow conditions and downstream distances.

In Fig. 3.8, large fluctuations are observed in the near wake for flow conditions $C_T = 0.1$ and $\mathrm{Ti}_k^0 = 0.3$. In this situation, the predictions of the two-term Gaussian function collapse into two spurious peaks and should therefore be disregarded as already mentioned in the analysis of Fig. 3.7. From Fig. 3.8 and Tab. 3.2b, it appears that the modelled values of the C_* coefficient in common operating conditions ($C_T = 0.8$) are at most marred by a relative error

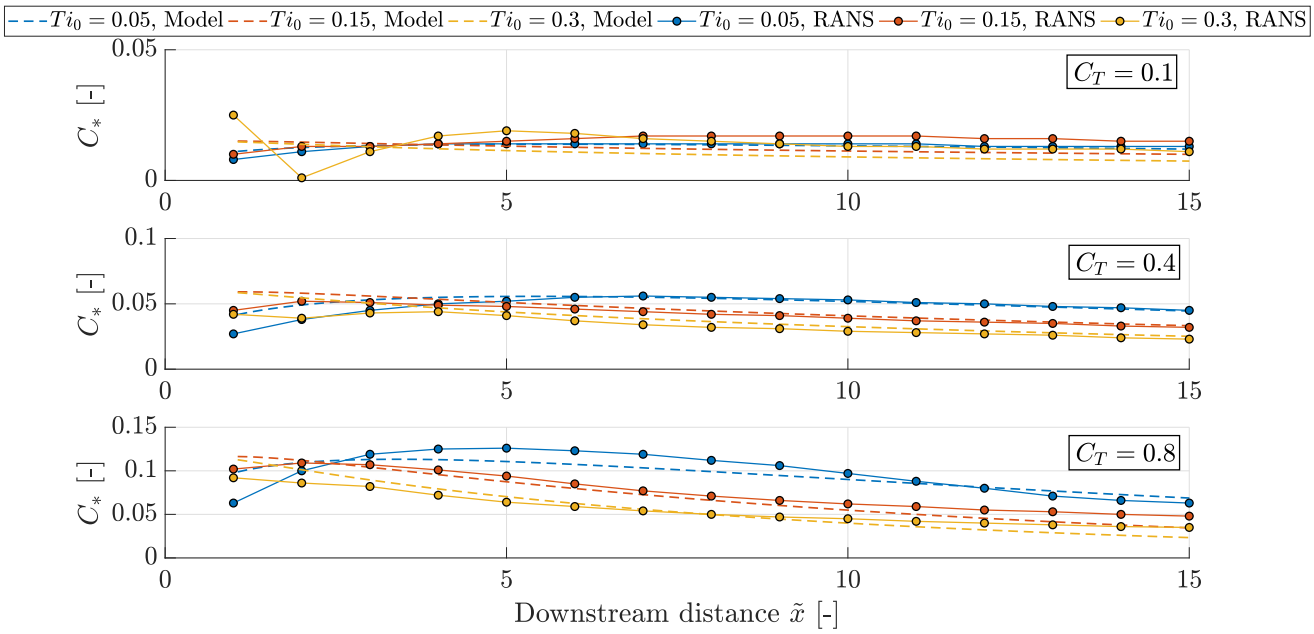

Figure 3.8: Comparison of the streamwise evolutions of the C_* coefficient derived from the new model Eq. 3.19 and the amplitude C_*^{RANS} recovered from the RANS look-up table at hub height under different flow conditions. The scale of the vertical axis is adapted in each case for readability.

of about 30%, reached $15D$ behind the rotor. This error however never exceeds $\pm 20\%$ for downstream distances lower than $10D$. Similarly to what has been observed for the modelling of the standard deviation σ_* in Tab. 3.2a, the largest discrepancies between C_* and C_*^{RANS} are obtained for a thrust coefficient $C_T = 0.1$, *i.e.*, rarely met in practice. For all the tested conditions (except the spurious case $C_T = 0.1$, $\mathrm{Ti}_k^0 = 0.30$), Fig. 3.8 shows that the model systematically over-estimates the values of the C_* coefficient in the first portion of the near wake. Two different explanations can justify this observation.

First, it should be recalled that the modelled values of the C_* coefficient depend on the quality of the one-dimensional model for $\Delta\mathrm{Ti}_{k,max}$ (Eq. 2.44). Since Fig. 2.9 showed that $\Delta\mathrm{Ti}_{k,max}$ tends to slightly over-estimate the values of $\Delta\mathrm{Ti}_{k,max}^{RANS}$ in the very near wake for $C_T = 0.8$, it is by no mean a surprise to observe the same behavior in Fig. 3.8 under $C_T = 0.8$. Few, if any, over-estimation of $\Delta\mathrm{Ti}_{k,max}^{RANS}$ is however visible in the near wake (Fig. 2.9) for values of C_T lower than 0.8. Hence, this suggests that the positive discrepancies observed between the modelled values of C_* and the RANS reference C_*^{RANS} in the near wake of Fig. 3.8 must have a different origin than a simple over-estimation of $\Delta\mathrm{Ti}_{k,max}$ with respect to $\Delta\mathrm{Ti}_{k,max}^{RANS}$.

Second, observations of the RANS turbulence intensity field in vertical cuts at different downstream distances showed that the tendency of C_* to over-estimate C_*^{RANS} is related to the presence of the boundary layer in the RANS simulations. As will be shown in Sec. 3.2.2, this phenomenon induces a deviation from the axisymmetric flow assumption made to derive the

two-dimensional added turbulence intensity profile. In particular, higher levels of turbulence intensities are generated at the top of the rotor, *i.e.*, where the velocity gradients are more pronounced. As the downstream distance increases, the turbulent kinetic energy diffuses towards the lower part of the rotor and allows to reduce the relative difference between the maximum added turbulence intensities, respectively obtained over the whole rotor and at hub height. It can therefore be concluded that, particularly for small downstream distances, the maximum value of the added turbulence intensity over the whole rotor is larger than the corresponding maximum value found at hub height. For that reason, the values of $\Delta\mathrm{Ti}_{k,max}^{RANS}$ (Eq. 1.24), based on which the new model for $\Delta\mathrm{Ti}_{k,max}$ was calibrated in Sec. 2.4.1, over-estimate by definition the values of the maximum recovered from the look-up table at hub height. This eventually results in the positives discrepancies between C_* and C_*^{RANS} noticed in Fig. 3.8 for small downstream distances behind the rotor. Note that attempts have been made to re-calibrate all the parameters, *i.e.*, ψ (Eq. 2.27), λ (Eq. 2.37) and the look-up table for m (Eq. 2.41) of the new model for the added turbulence intensity based on the maximum value $\Delta\mathrm{Ti}_{k,max}^{RANS}$ at hub height. However, while the maximum over the whole rotor evolves progressively with distance, the one specifically recovered at hub height fluctuates much more. Therefore, no suitable choice of parameters ψ, λ and m could be made. Still, one should keep in mind that C_* significantly over-estimates C_*^{RANS} in a small portion of the near wake only, in which it is beyond dispute that no downstream wind turbine would ever be placed.

Finally, for larger downstream distances, Fig. 2.9 showed that the modelled added turbulence intensity $\Delta\mathrm{Ti}_{k,max}$ under-predicts $\Delta\mathrm{Ti}_{k,max}^{RANS}$, which in turns leads to the slight under-prediction of C_*^{RANS} observed in Fig. 3.8.

Following the analyses of Fig. 3.7 and Fig. 3.8 for the modelling of σ_* and C_* respectively, the two-dimensional added turbulence intensity profiles (Eq. 3.13) can be plotted in Fig. 3.9 for a variety of flow conditions. In Fig. 3.7 and Fig. 3.8, both σ_* and C_* were seen to be marred by a modelling error of greater or lesser importance depending on the situation. In order to distinguish the impact on the profile of both modelling errors, a sensitivity study is carried out in parallel with the profile analysis. From Eq. 3.13, the total error on $\Delta\mathrm{Ti}_k$ due to small discrepancies dC_* and $d\sigma_*$ can be linearized as:

$$d(\Delta\mathrm{Ti}_k) \simeq \underbrace{\frac{d\Delta\mathrm{Ti}_k}{dC_*}\,dC_*}_{S_1} + \underbrace{\frac{\Delta\mathrm{Ti}_k}{d\sigma_*}\,d\sigma_*}_{S_2}\,. \tag{3.20}$$

In Eq. 3.20, the S_1 and S_2 terms respectively account for the impact of a modelling error on the amplitude (Eq. 3.19) and on the standard deviation (Eq. 3.17). It should be emphasized that both S_1 and S_2 depend on C_T and Ti_k^0 as well as on the downstream and the lateral distances, x and y. Hence, for the sake of conciseness, the focus is placed on the sensitivity at the lateral positions $y = \pm y_c$ and $y = 0$. The analytical form of S_1 can trivially be derived from Eq. 3.13 and be written as:

$$S_1(y = \pm y_c) = \left(1 + \exp\left(\frac{-2\,y_c^2}{\sigma_*^2}\right)\right) dC_* \quad \text{and} \quad S_1(y = 0) = 2\,\exp\left(\frac{-y_c^2}{2\,\sigma_*^2}\right) dC_* \tag{3.21}$$

at the lateral positions of interest. Similarly, the analytical development of S_2 leads to the expression

$$S_2 = C_* \left(\exp\left(-\frac{(y-y_c)^2}{2\,\sigma_*^2} \right) \frac{(y-y_c)^2}{\sigma_*^3} + \exp\left(-\frac{(y+y_c)^2}{2\,\sigma_*^2} \right) \frac{(y+y_c)^2}{\sigma_*^3} \right) d\sigma_*, \tag{3.22}$$

from which $S_2(y \pm y_c)$ and $S_2(y=0)$ read:

$$S_2(y=\pm y_c) = C_* \exp\left(\frac{-2\,y_c^2}{\sigma_*^2} \right) \frac{4\,y_c^2}{\sigma_*^3}\, d\sigma_* \quad \text{and} \quad S_2(y=0) = C_* \exp\left(\frac{-y_c^2}{2\,\sigma_*^2} \right) \frac{2\,y_c^2}{\sigma_*^3}\, d\sigma_*. \tag{3.23}$$

From Tab. 3.2, it was concluded that both the relative error on σ_* and on C_* rarely exceed $\pm 20\%$ under realistic flow conditions. Therefore, the terms $S_1(y=\pm y_c)$, $S_1(y=0)$ (Eq. 3.21) and $S_2(y=\pm)$, $S_2(y=0)$ (Eq. 3.23) are represented in Fig. 3.9 for $dC_* = \pm 0.2 \times C_*$ and $d\sigma_* = \pm 0.2 \times \sigma_*$. Several elements in Fig. 3.9 can then be discussed.

First, it appears that the $\pm 20\%$ sensitivity interval S_2 is barely visible at $y = y_c = D/2$, suggesting that an error introduced by the modelling of σ_* has only little impact on the edge values of the predicted two-dimensional profile. On the contrary the sensitivity with respect to σ_* is much more pronounced at the center of the wake, as illustrated by the larger sensitivity interval S_2 at $y = 0$ in Fig. 3.9a. It can however be observed that the center-line value of the two-dimensional $\Delta \mathrm{Ti}_k$ profile becomes less sensitive to σ_* as the two separate peaks of the two-term Gaussian function merge. This can clearly be seen in Fig. 3.9b, for which the large atmospheric turbulence intensity ($\mathrm{Ti}_k^0 = 0.30$) enhances the wake recovery and therefore leads to a single peak profile faster downstream. Indeed, if the velocity deficit quickly recovers behind the rotor, the strong velocity gradients, *i.e.* the source of turbulent kinetic energy (TKE) in the wake, are quickly attenuated, reducing the TKE production accordingly. Without a sufficient source of turbulent energy, the dissipation mechanism rapidly dominates. For that reason, the amplitude of the added turbulent intensity profile at $\tilde{x} = 10$ in Fig. 3.9b appears weaker than at the same downstream position in Fig. 3.9a, even though higher levels of added turbulence intensity are initially observed at $\tilde{x} = 1$ in Fig. 3.9b.

In addition, the sensitivity with respect to C_* does not significantly vary with the downstream nor the lateral distances. In other words, a modelling error on C_* tends to introduce a regular offset between the modelled profile and the two-term fitted Gaussian. An example of a constant offset along the lateral distance can be observed at $\tilde{x} = 5$ in Fig. 3.9a, for which Tab.3.2b shows that the error on σ_* (-2%) is negligible compared to that on C_* (-12%). Comparing Fig. 3.9a and Fig. 3.9b, it can be noticed that both S_1 and S_2 show little variation when Ti_k^0 increases. By contrast, when smaller values of the thrust coefficient are considered (Fig. 3.9c), the amplitude of the added turbulence intensity decreases (Eq. 2.37) and both S_1 and S_2 decline accordingly. As a result of the sensitivity analysis, one can be convinced that any small modelling error on σ_* or C_* is not significantly amplified by Eq. 3.13 and therefore does not lead to substantially larger error on the two-dimensional added turbulence intensity profile.

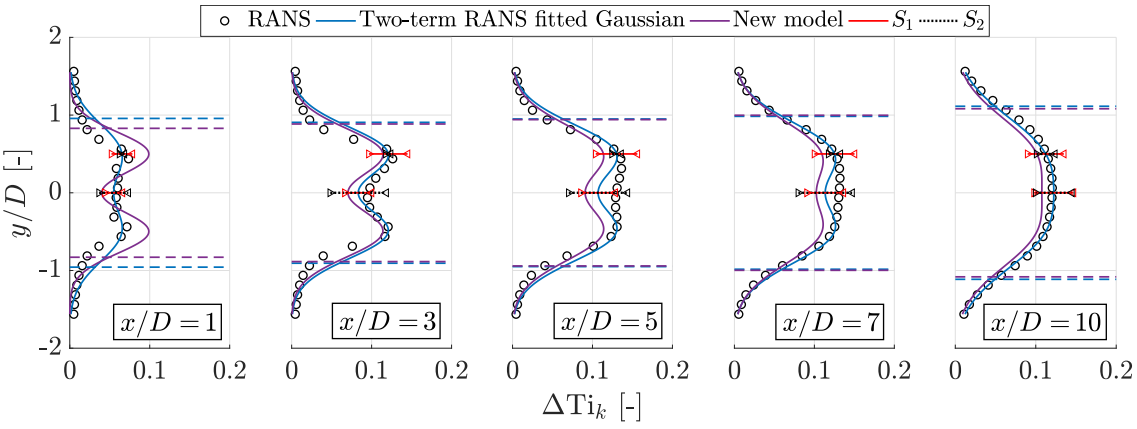

(a) $C_T = 0.8$ and $\mathrm{Ti}_k^0 = 0.05$ [-]

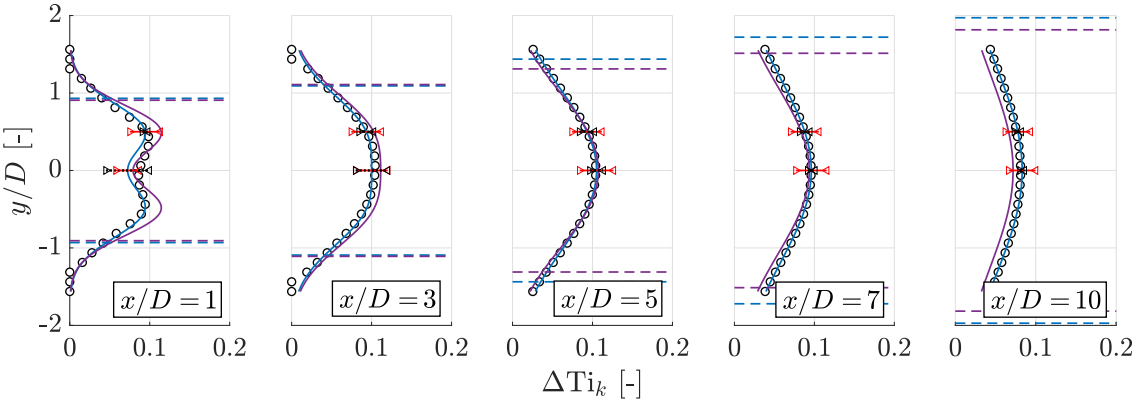

(b) $C_T = 0.8$ and $\mathrm{Ti}_k^0 = 0.30$ [-]

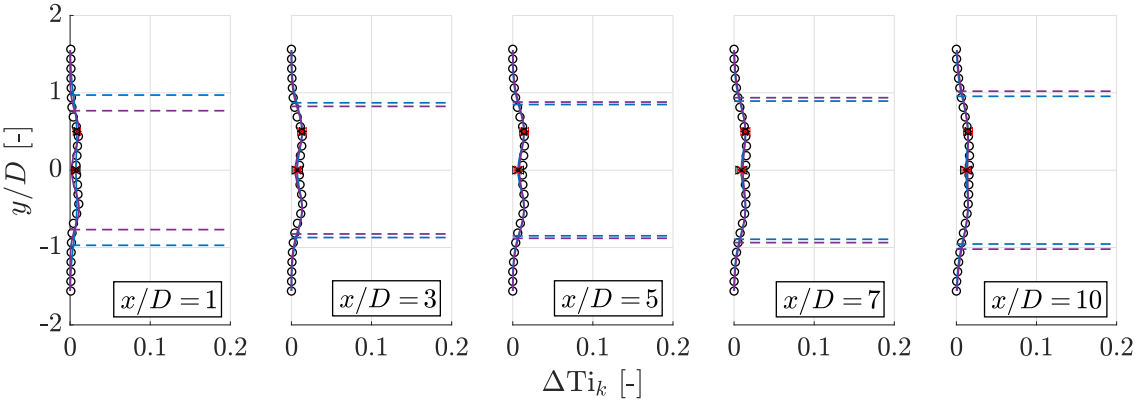

(c) $C_T = 0.1$ and $\mathrm{Ti}_k^0 = 0.05$ [-]

Figure 3.9: Streamwise evolution of the two-dimensional added turbulence intensity profile at hub height under different flow conditions. The predictions of the new model are compared to the two-term Gaussian curve fitted to the RANS data. The two terms S_1 ans S_2 of the sensitivity interval (Eq. 3.20) are shown at $y = 0$ and $y = D/2$. The wake half-widths $r^*_{1/2}$ and $(r^*_{1/2})^{RANS}$ are represented as dashed lines in the figure.

Lingkan and Buxton [19] experimentally shows that a two-term Gaussian function is adequate to describe the profile of added turbulence intensity in the case $C_T \simeq 0.72$, $\mathrm{Ti}_k^0 = 0.04$. An important result of this section is undoubtedly the evidence that the two-term Gaussian function suggested by Lingkan and Buxton [19] is also sufficiently modular to describe the profile of added turbulence intensity in a wide variety of cases. This observation is particularly interesting in a context where the current models implemented in PyWake do not allow a faithful representation of the physics behind the added turbulence intensity profile. By contrast, in Fig. 3.9, it was shown that the two-term fitted Gaussian is suitable to represent the production of turbulent kinetic energy localized around the wake perimeter. Moreover, the tendency of the two peaks to become one from a certain downstream distance, due to turbulent energy diffusion, is naturally modelled by a two-term Gaussian function. The dissipation mechanism also appeared to be well accounted for as evidenced by the decreasing amplitude shown in Fig. 3.9b. Eventually, Fig. 3.9 visually demonstrated that introducing a modelling of the parameters σ_* and C_* still allows to obtain excellent estimations of the profile in all the tested situations.

3.2.2 Validity of the assumption of an axisymmetric added turbulence intensity field

Similarly to Sec. 3.1.3, in which the assumption of an axisymmetric velocity deficit field has been discussed, this section aims at assessing the validity of the axisymmetric assumption applied to the added turbulence intensity profile. The comparison between the added turbulence intensity field as predicted by the new model and as generated by EllipSys is shown in Fig. 3.10 for flow conditions $C_T = 0.8$ and $\mathrm{Ti}_k^0 = 0.05$. Overall, it appears that the axisymmetric generalization of the two-dimensional added turbulence intensity profile provides a good estimate of the corresponding RANS data. Still, some elements stand out from Fig. 3.10 and are worth discussing.

As mentioned in Sec. 3.2.1 and depicted in Fig. 3.10 for $\tilde{x} \geqslant 3$, the presence of the boundary layer leads to higher velocity gradients and therefore to an increased production of turbulent kinetic energy at the top of the rotor. This turbulence is then diffused towards the lower part of the rotor, as demonstrated by the displacement of the maximum of added turbulence intensity towards the rotor center. It is important to specify that, in practice, the homogenization of the added turbulence intensity levels along the azimuthal direction is enhanced by the non-zero tangential velocity of the flow. Indeed, the rotating component of the flow adds a tangential convection mechanism to the diffusion of the turbulent kinetic energy. Comparing Fig. 3.10 to Fig. 3.6, it can be observed that the boundary layer introduces more asymmetry into the added turbulence intensity field than into the velocity deficit field. Based on the observation of Fig. 3.10 at $\tilde{x} = 5$, one could however argue that the boundary layer simultaneously reduces the gradients in the lower part of the wake, so that the average turbulent kinetic energy produced over the rotor is close to the average computed under the axisymmetric assumption.

Moreover, two physical characteristics, omitted by the new model for the added turbulence intensity, can be seen at $\tilde{x} = 1$ (Fig. 3.10). First, the blockage effect briefly discussed in Sec. 3.1.3 appears to reinforce the velocity gradients in the lower part of the wake, consequently

balancing the effect of the boundary layer. As a result, the production of turbulent kinetic energy is maximum at the bottom of the rotor over the portion of the near wake subjected to significant blockage, *i.e.* for $\tilde{x} < 3$. Furthermore, irregularities in the RANS added turbulence intensity field are visible close to the center of the wake at $\tilde{x} = 1$. Worth recalling is that the analysis of the velocity deficit field carried out in Sec. 3.1.3 showed evidence of undisturbed air flowing through the central section of the force actuator disk. Therefore, the irregularities in the added turbulence intensity field observed at $\tilde{x} = 1$ originate from the effect of the velocity gradients between this undisturbed air and the rest of the flow through the rotor. This local source of turbulent kinetic energy however vanishes as soon as the velocity field becomes homogeneous around the center, *i.e.* for $\tilde{x} > 1$ as shown in Fig. 3.6.

To sum up, Fig. 3.10 in general shows good agreement between the RANS data and the modelled added turbulence intensity field. However, it is observed that the atmospheric boundary layer introduces significant asymmetry in the turbulence field. As suggested by the works of Qian and Ishihara [24] and Tian et al. [25], future improvements to the model could include a weighting term for the velocity profile as a function of the vertical position.

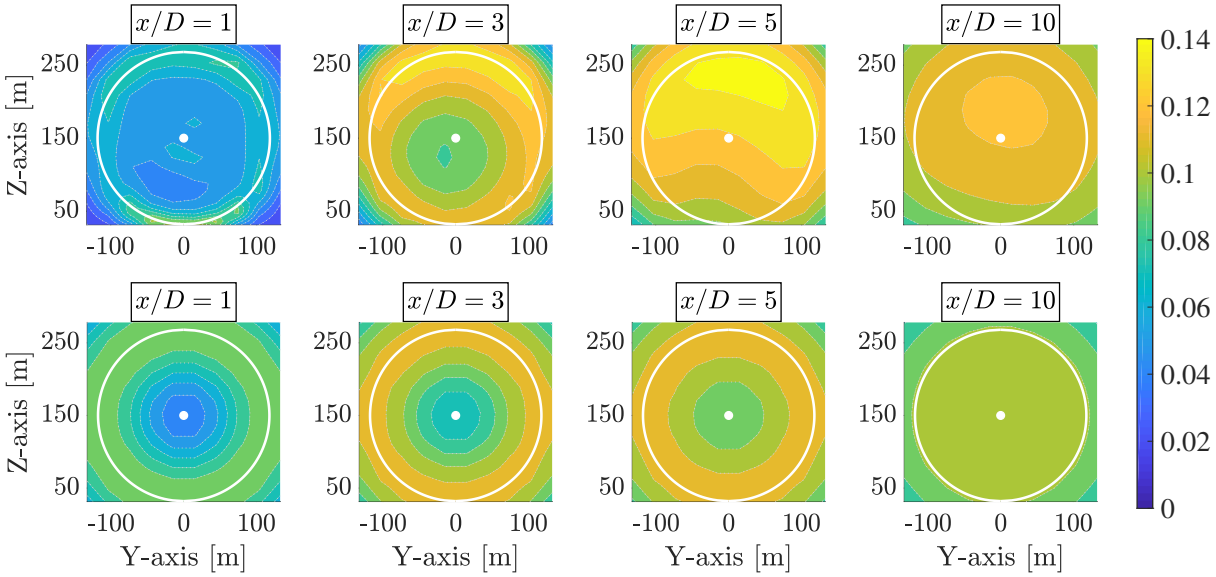

Figure 3.10: Added turbulence intensity ($\Delta \mathrm{Ti}_k$) field in vertical cuts at increasing downstream distances for $C_T = 0.8$ and $\mathrm{Ti}_k^0 = 0.05$. The predictions of the new model (lower row) are compared to the RANS data generated by EllipSys (upper row). The perimeter and rotor center are shown in white in the figures.

Chapter 4

Performance assessment of the new model in a multiple-wake configuration

4.1 Overview

In this fourth and final chapter, the performance of the new full wake model, *i.e.* combining both the velocity deficit (Sec. 3.1.2) and the added turbulence intensity (Sec. 3.2.1) models, are assessed and discussed. Although both the velocity deficit and the added turbulence intensity single-wake models have shown promising results over a wide variety of flow conditions, the reliability of the new wake model predictions is not yet guaranteed in the case of a full wind farm. Therefore, the main purpose of this section is to investigate whether the wake model developed through this work can effectively replace the use of the RANS look-up table in a multiple-wake situation.

In the scope of this work, the analysis is limited to the academic case of a one-dimensional array of five wind turbines under realistic flow conditions. First, the main features of the PyWake software are described in Sec. 4.2 and details are addressed on the implementation of the new wake model. As will be shown later, PyWake is a very modular tool that allows to study different combinations of velocity deficit and added turbulence intensity models. Among all the possibilities offered in this software, two are compared to the new full wake model developed earlier. In each case, the different superposition methods introduced in Sec. 1.2.2 are examined and the corresponding performances are discussed. In this analysis, the results of a RANS simulation performed over the whole column of wind turbines are used as the reference case against which the models are tested.

4.2 Modelling of a one-dimensional array of wind turbines

4.2.1 Tested configuration

This section aims at summarizing the main characteristics of the tested configuration. First and foremost, the rotor diameter D and the hub height z_H of a 15MW generic wind turbine are

defined and specified in PyWake. Moreover, realistic values of the wind farm inflow conditions, *i.e.*, the free stream velocity U_∞ and the level of atmospheric turbulence intensity Ti_k^0, are selected. In order to maximize the impact of the upstream turbines on the local inflow conditions of the next turbine, the wind direction is chosen perfectly aligned with the column of wind turbines, *i.e.* $\angle U_\infty = 270°$. Worth mentioning is that the actual inflow velocity field in a wind farm depends on many factors such as the period of the year, the time of the day and the orientation. In PyWake, it is possible to account for these dependencies by modelling the probability density function of the wind speed with a Weibull distribution, the parameters of which depend on the angular sector of interest. In practice, wind turbines in a wind farm are generally placed at a distance of three to ten diameters from one another. Hence, a moderate spacing $S = 5D$ is retained in this case study. A brief summary of the main characteristics listed above in given in Tab. 4.1.

Table 4.1: Main characteristics of the tested configuration. NbWT stands for the Number of Wind Turbines in the columnar layout.

Wind turbine		Inflow conditions			Site	
D [m]	z_H [m]	U_∞ [m/s]	Ti_k^0 [-]	$\angle U_\infty$ [°]	NbWT	S [m]
236	150	10	0.05	270	5	$5D$

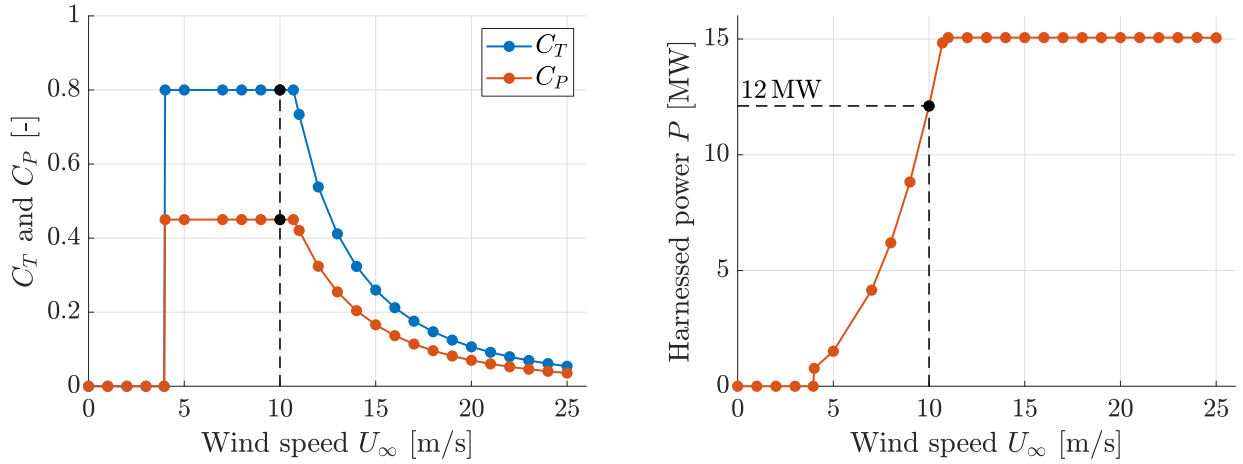

(a) Thrust and power coefficients

(b) Power

Figure 4.1: Thrust and power coefficients curves (a) and power curve (b) of the tested turbine. The operating point is marked by a black dot in the figures.

In general, the evolution of the thrust and power coefficients as a function of wind speed depends essentially on the design of the blades and the way the turbine is monitored. For the generic turbine used in this section, the C_T and C_P curves are shown in Fig. 4.1a and the corresponding power curve is depicted in Fig. 4.1b. Below the so-called cut-in speed, *i.e.* $U_\infty^{CI} \simeq 4\,\mathrm{m/s}$, too little kinetic energy can be harnessed from the wind and the rotation of the

blades is prevented by hydraulic brakes. For wind speeds larger than U_∞^{CI}, the power coefficient, and consequently the thrust coefficient, are kept constant by automatically adjusting the pitch angle or the rotation speed of the blades. The corresponding power thus increases with the cube of the wind speed in this region, as evidenced by the definition of C_P introduced in Sec. 1.1 (Eq. 1.1). Above the rated wind speed ($U_\infty^R \simeq 11\text{m/s}$), the so-called rated power is reached, *i.e.* the maximum power that the generator can handle, and the pitch controller ensures that this value is not exceeded. In this region, both the thrust and power coefficients decrease as a result of Eq. 1.1. Note that in practice, a cut-out speed $U_\infty^{CO} \simeq 22\,\text{m/s}$ is defined, above which the blades are feathered for safety reasons. In the configuration of interest, the inflow velocity $U_\infty = 10\,\text{m/s}$ corresponds to a thrust coefficient $C_T = 0.8$ and a generated power $P = 12\,\text{MW}$. Given that the inflow wind speed is below the rated speed, it can be pointed out from Fig. 4.1a that all the downstream turbines will also operate at $C_T = 0.8$ because they always perceive an incoming velocity slower or equal to $U_\infty = 10\,\text{m/s}$.

4.2.2 PyWake implementation of the new wake model

PyWake [9] is an objected-oriented code implemented in the Python programming language and designed to offer a powerful tool for wind farm flow modeling and power assessment. The rapidity and the great versatility of this software are two of its principal assets. The first one because the vectorized implementation enables to simultaneously consider different wind speeds and directions, allowing very fast estimations of the annual energy production (AEP) of a whole wind farm. The second as PyWake offers a multitude of different building blocks that can be arranged in a large number of combinations. For any of these combinations, it is however crucial for the user to be aware of the physics represented by the model and the underlying assumptions.

Fig. 4.2 depicts a schematic overview of the main building blocks used in this case study. Note that in this figure, the elements newly implemented in PyWake in the scope of this work are marked with an asterisk symbol. In each block, the title corresponds to the name of the base class implemented in PyWake. The content of the block refers to key elements that are to be discussed. The objects used to set up the tested configuration are represented in pale green. The different parameters detailed in Sec. 4.2.1 are given as inputs to these objects. Moreover, the main blocks involved in the wake superposition process are shown in light blue. Note that in the *SuperpositionModel* object, the methods *LinearSum*, *SquaredSum* and *MaxSum* respectively refer to "Method A", Method B"" and Method "C" introduced in Tab. 1.1a. Similarly for the *AddedTurbSuperpositionModel* object, the methods *LinearSum*, *FullSquaredSum* and *MaxSum* respectively correspond to "Method A", Method "D" and Method "C" shown in Tab. 1.1b. In addition, the single-wake velocity deficit and added turbulence intensity models are depicted in grey in Fig. 4.2. This grey rectangle essentially represents the blocks for which each turbine is considered in a stand-alone configuration. Worth mentioning is that additional options for single-wake modelling are available in PyWake and could be added to this grey frame. Among those, the possibility to include the *BlockageDeficitModel* and *DeflectionModel* blocks should be mentioned. While the latter would be of little interest in this case study[1], the former is ex-

[1]There is no misalignment between the direction of the incoming wind and the column of wind turbines.

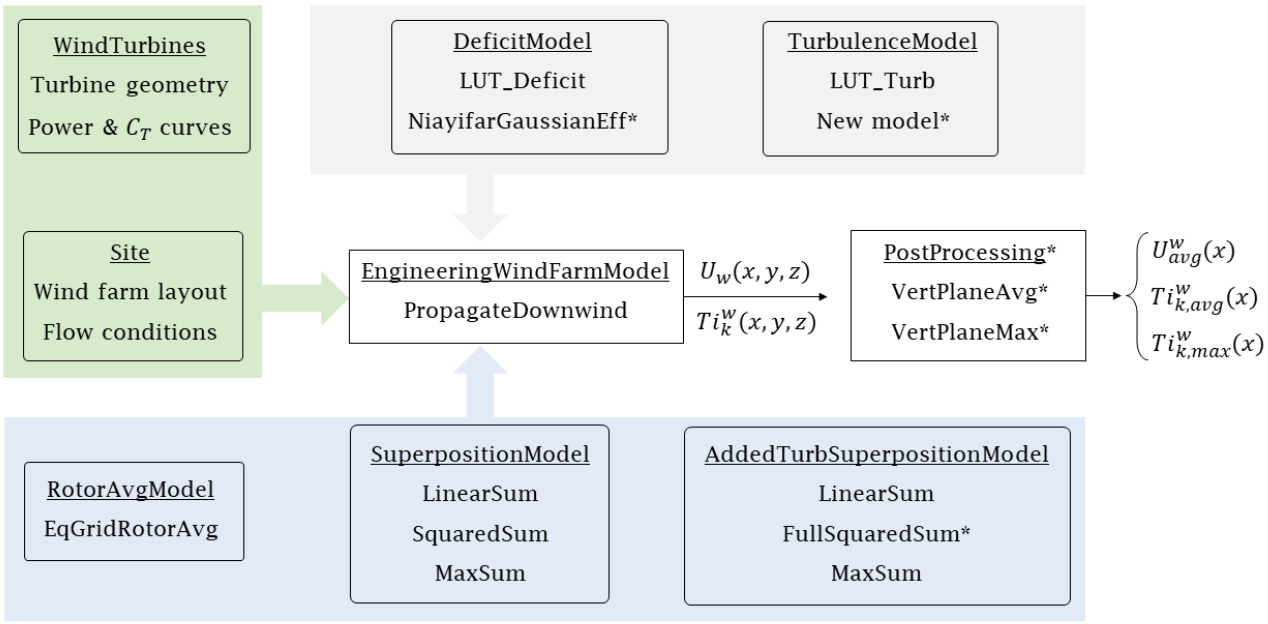

Figure 4.2: Summary of the main building blocks implemented in PyWake. New elements added in the scope of this project are marked with an asterisk symbol.

pected to improve the fidelity of the results and could therefore be investigated in future works. As can be seen in Fig. 4.2, the core of the simulation is the central *EngineeringWindFarmModel* block. In particular, this object features the *PropagateDownwind* class in which a loop over the wind turbines indices, denoted by i, is implemented. A very brief insight of the algorithm used in PyWake is given hereafter.

First, it is important to specify that the variables involved in the flow field computation are in general four-dimensional vectors. For example, *deficit_ijlk* and *add_turb_ijlk* respectively represent the velocity deficit and the added turbulence intensity caused by the i^{th} turbine and computed at each grid point j, for each wind direction l and inflow speed k. At each iteration i in the loop, *deficit_ijlk* and *add_turb_ijlk* are recovered from *DeficitModel* and *TurbulenceModel*. Superpositions methods are then employed in *SuperpositionModel* and *AddedTurbSuperpositionModel* to compute the effective wind speed and the turbulence intensity level at each grid node j in the combined wake of all the upstream turbines. Then, the *RotorAvgModel* object identifies the grid points j located right upstream of the $(i+1)^{th}$ rotor. The local inflow speed u_0^{i+1} perceived by this turbine is computed in *RotorAvgModel* as an average of the effective velocities found at some of the j points of interest. The local level of incoming turbulence intensity is recovered similarly. The new inflow conditions being known, the next iteration begins. Although several rotor averaging methods are available in PyWake, only the so-called *EqGridRotorAvg* is considered in this analysis. The rationale behind this

choice is clarified in Sec. 4.2.3. Eventually, the effective velocity and turbulence intensity in the combined wakes, respectively denoted $U(x, y, z)$ and $\mathrm{Ti}_k(x, y, z)$, are obtained at all points of the three-dimensional domain. In order to facilitate the analysis of the results, an additional *PostProcessing* block is implemented. At each downstream position, this block allows to recover the average over the rotor area of both the velocity field and the turbulence intensity field, *i.e.* $U_{avg}(x)$ and $\mathrm{Ti}_{k,avg}(x)$. In addition, the maximum values of U and Ti_k over the rotor sections are retrieved and respectively denoted $U_{max}(x)$ and $\mathrm{Ti}_{k,max}$.

A few additional points can be made with regard to Fig. 4.2. In the *DeficitModel* block, the object *NiayifarGaussianEff* is simply the re-calibrated version of the Niayifar and Porté-Agel [17] model, following the results of Sec. 3.1.2. In the same block, the *LUT_Deficit* object is the RANS look-up table model of the single-wake deficit that is intended to be replaced by *NiayifarGaussianEff*. Likewise, *LUT_Turb* is the RANS look-up table single-wake model of the added turbulence intensity, of which *New model* is expected to be an efficient alternative. Note that in PyWake, *New model* is referred to as *THD2023TurbulenceModel*. Attention should finally be paid to the fact that the PyWake grid differs in general from that used in EllipSys to generate the look-up table, the two grids being linked by interpolation methods.

4.2.3 Rotor average model

In the previous sections, the error introduced by the single-wake modelling of the velocity deficit and of the added turbulence intensity has been assessed and discussed. However, superimposing these single-wake models in PyWake leads to additional sources of error. First of all, it should be recalled that all the superposition methods are inherently marred by errors as they mainly rely on mathematical expressions, the physical meaning of which is still disputed. Furthermore, in PyWake, the inflow speed of a downstream turbine is reduced to a single value, thus erasing the differences in speed observed at different points on the rotor. The same applies to the inflow turbulent intensity. As mentioned in section Sec. 4.2.2, this single value is defined as an average of the speeds (*resp.* turbulence intensities) calculated at some grid points of interest encompassed by the downstream rotor. Therefore, it is important to investigate the minimum number of grid points required to ensure that the inflow conditions of a downstream turbine are computed in a reliable manner.

Besides, the *PostProcessing* block shown in Fig. 4.2 also involves the averaging of the quantities $U(x, y, z)$ and $\mathrm{Ti}_k(x, y, z)$ over the rotor area at any downstream position x. In order to allow a fair comparison between the output values, $U_{avg}(x)$ and $\mathrm{Ti}_{k,avg}(x)$, and the corresponding results of the full RANS simulation of the whole array, the averaging methods used in both cases should be similar. The velocity and turbulence intensity fields generated by EllipSys are treated in Matlab and the results of the full RANS simulation are averaged over the sampled points shown in red in Fig. 4.3a. These results are referred to as the "Reference" quantities in the rest of this work. The grid used in EllipSys, both to generate the RANS look-up table and to simulate the whole array, is depicted in dotted lines in Fig. 4.3a. Note that, given the variable spacing of the grid, a weighted average is used to compute the reference values for velocity and turbulent intensity.

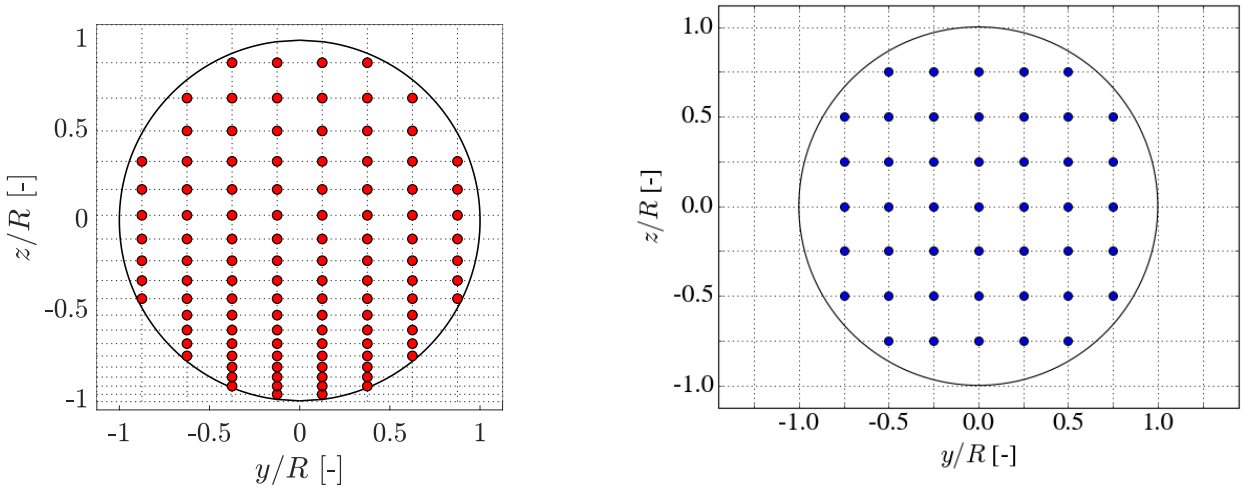

(a) EllipSys

(b) PyWake

Figure 4.3: Sampled points over the rotor area in EllipSys (a) and in PyWake for *EqGridRotorAvg(N = 7)* (b). For each case, the calculation grid is shown in the figure.

In PyWake, defining a grid identical to the one used by EllipSys is certainly the most natural way to ensure that the rotor is sampled in the same manner in both approaches. The large number of sampling points (Fig. 4.3a) however resulted in unmet memory requirements, causing this option to be discarded. Hence, a coarser mesh is selected in PyWake, together with an informed choice of averaging method. Among the existing options, the Circular Gauss Integration [39] method and the Polar Grid method sample the rotor cross-section uniformly and therefore seem recommendable. In the scope of this project, the cartesian averaging method *EqGridRotorAvg* is however preferred to faciliate the implementation of the *PostProcessing* block (Fig. 4.2). This approach defines a set of $N \times N$ equidistant cartesian points over the rotor section and discards those outside this area as shown in Fig. 4.3b for *EqGridRotorAvg(N = 7)*. It is interesting to notice that, in general, these local $N \times N$ grid points do not need to coincide with the points of the three-dimensional domain over which the flow is visualized. This feature offers the user the possibility to create smooth flow maps over highly refined grids while maintaining a reasonable number of sampling points over the rotor sections. Still, in this analysis, given that the $LUT\_Deficit$ and LUT_Turb single-wake models can only be used over a coarse grid to satisfy the memory requirements, the decision was made to use the same spacing for the $N \times N$ local averaging grid and the three-dimensional grid over the domain.

In light of the previous paragraph, the question as to which value of N must be selected should be addressed. In order to answer this question, a convergence analysis of the N parameter is carried out for a stand-alone wind turbine. First, the weighted averages of ΔU^{EpS} and $\Delta \mathrm{Ti}_k^{EpS}$ are computed over the EllipSys grid (Fig. 4.3a) at $\tilde{x} = 5$. The resulting scalar values are denoted ΔU_{avg}^{EpS} and $\mathrm{Ti}_{k,avg}^{EpS}$, respectively. Then, the corresponding PyWake quantities, *i.e.* using $LUT\_Deficit$ and LUT_Turb over the $N \times N$ grid (Fig. 4.3b), are recovered and denoted

ΔU_{avg}^{PyW} and $\mathrm{Ti}_{k,avg}^{PyW}$. A wide range of values of N is tested and the relative errors $\epsilon_{\Delta U}$ [%] and $\epsilon_{\Delta \mathrm{Ti}}$ [%] are computed in each case:

$$\epsilon_{\Delta U} = 100 \times \frac{\Delta U_{avg}^{PyW} - \Delta U_{avg}^{EpS}}{\Delta U_{avg}^{EpS}} \quad \text{and} \quad \epsilon_{\Delta \mathrm{Ti}} = 100 \times \frac{\Delta \mathrm{Ti}_{k,avg}^{PyW} - \Delta \mathrm{Ti}_{k,avg}^{EpS}}{\Delta \mathrm{Ti}_{k,avg}^{EpS}}. \tag{4.1}$$

The evolution of the relative errors with N is shown in Fig. 4.4a. Note that only the cases of interest are studied here, *i.e.* $C_T = 0.8$ with $\mathrm{Ti}_k^0 = 0.05$, $\mathrm{Ti}_k^0 = 0.15$ and $\mathrm{Ti}_k^0 = 0.30$. Three representative values of the inflow turbulence intensity are considered so as to assess the quality of the rotor averaging method in the event of high turbulence intensity levels caused by the upstream turbines. Eventually, the discussion is enriched with the analysis of Fig. 4.4b, showing the evolution of the ratio of the sampled area A_S over the actual rotor area A_R. In this figure, the sampled area corresponds to the cartesian area, *i.e.* the sum of all the square cells, strictly encompassed by the rotor.

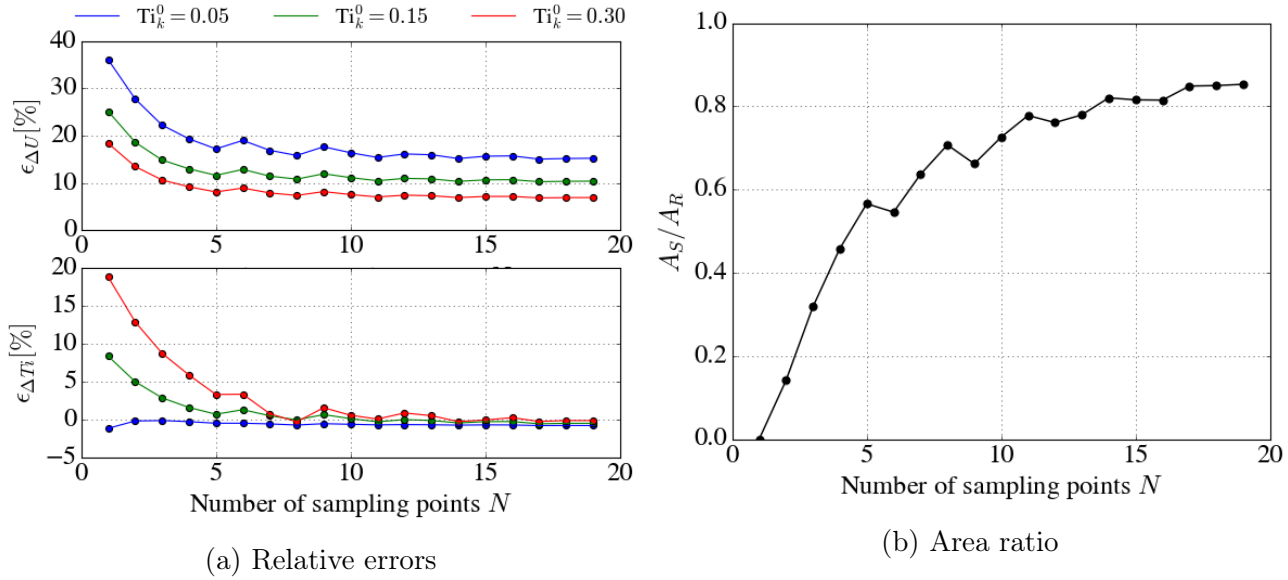

(a) Relative errors

(b) Area ratio

Figure 4.4: Convergence analysis in terms of the relative errors $\epsilon_{\Delta U}$, $\epsilon_{\Delta \mathrm{Ti}}$ for three levels of inflow turbulence intensity (a) and in terms of the area ratio (b).

As could have been expected, both $\epsilon_{\Delta U}$ and $\epsilon_{\Delta \mathrm{Ti}}$ drastically decrease as N increases. All the curves in Fig. 4.4a essentially flatten after $N = 7$, with the exception of minor fluctuations. In the lower figure of Fig. 4.4a, it can be seen that the added turbulence intensity computed over the $N \times N$ PyWake grid overestimates more the value of $\Delta \mathrm{Ti}_{k,avg}^{EpS}$ at larger Ti_k^0 values. The exact opposite observation can be made in the upper figure of Fig. 4.4a, for which ΔU^{PyW} overestimates ΔU^{EpS} more for smaller values of Ti_k^0. In the same figure, a persistent error remains, even for finely discretized PyWake grids.

The explanation behind these observations can be clarified in light of Fig. 4.4b. From this figure, it appears clear that substantial discrepancies remain between the sampled area and the actual rotor area, whatever the degree of refinement of the PyWake grid. Logically enough, the non-sampled portions of the disk are always located close to the rotor edges, especially at the topmost, bottommost, leftmost and rightmost parts as shown in Fig. 4.3b. It can therefore be concluded that the *EqGridRotorAverage* tends to disregard the values of ΔU^{PyW} and $\Delta \mathrm{Ti}_k^{PyW}$ located in these regions when computing the rotor averages, ΔU_{avg}^{PyW} and $\Delta \mathrm{Ti}_{k,avg}^{PyW}$. As a result of the Gaussian-like distribution of the velocity deficit over the rotor section, *EqGridRotorAverage* filters out the regions of low velocity deficits, consequently overestimating the value of the rotor average, *i.e.*, $\epsilon_{\Delta U} > 0$. As shown in Fig. 4.4a, this effect is reduced for partially recovered velocity deficit profiles, *i.e.* for large values of Ti_k^0. The relative error on the deficit however never reaches zero as the velocity deficit profile retains a Gaussian shape at $\tilde{x} = 5$, in all the tested conditions.

By contrast, the added turbulence intensity profile at $\tilde{x} = 5$ resembles a two-term Gaussian function for low values of Ti_k^0 as shown in Fig. 3.9a. If the average is performed with $N = 1$ sampling point under $\mathrm{Ti}_k^0 = 0.05$, only the central value of the added turbulence intensity profile is accounted for, thus under-estimating the value of $\Delta \mathrm{Ti}_{k,avg}^{EpS}$. For higher values of the inflow turbulence intensity at $\tilde{x} = 5$, Fig. 3.9b indicates that the maximum occurs at the rotor center, leading to an over-prediction of the average and a positive relative error $\epsilon_{\Delta \mathrm{Ti}}$. Eventually, the value $N = 7$, for which the grid is depicted in Fig. 4.3b, is retained. This choice indeed allows to limit both relative errors (Eq. 4.1) while maintaining reasonable memory requirements. Even though the relative error on the deficit is only slightly less than 20%, it should be recalled that the corresponding relative error on the total velocity field is significantly lower. As a matter of fact, this value has been estimated to be less than 3% of the wake velocity, confirming the choice $N = 7$.

4.3 Results and discussion

The objective of this last section is twofold. First, it aims at assessing the quality of the new wake model used as an alternative to the RANS look-up table model in a multiple-wake situation. To do so, the predictions of the new wake model (*NiayifarGaussianEff + THD2023TurbulenceModel*) are compared to that of the RANS look-up table model (*LUT_Deficit + LUT_Turb*) for the test configuration described in Sec. 4.2.1. The second purpose is more general, and concerns the identification of relevant superposition methods in the case of a columnar configuration of wind turbines. To this end, the RANS look-up table wake model is compared to the Reference values obtained with the full RANS simulation of the whole array. A summary of the tested combinations of velocity deficit and added turbulence intensity models in given in Tab. 4.2. In this table, the new wake model and the RANS look-up table model are respectively referred to as "Model 1" and "Model 3". An additional option, denoted "Model 2", is also considered and consists in an in-between solution. In this wake model, the memory intensive RANS look-up table is only used for the velocity deficit, together with the newly developed added turbulence intensity model.

Table 4.2: Summary of the tested combinations of single-wake velocity deficit and added turbulence models.

Name	Deficit model	Added turbulence model
Model 3	*LUT_Deficit*	*LUT_Turb*
Model 2	*LUT_Deficit*	*THD2023TurbulenceModel*
Model 1	*NiayifarGaussianEff*	*THD2023TurbulenceModel*
Reference	Full RANS simulation	

In the rest of this section, several superposition methods are tested, both for the velocity deficit and the added turbulence intensity. Among those introduced in Tab. 1.1 (Sec. 1.2.2), all except "Method E" are discussed. This method is indeed expected to give similar results to "Method C" and is therefore not studied any further. Tab. 4.3 shows the correspondence between the methods defined in Tab. 1.1 and the names used in the current section to refer to them.

Table 4.3: Correspondence between the superposition methods introduced in Tab. 1.1 and their given names in the current analysis.

(a) Velocity deficit

Method in Tab. 1.1a	Name
A	*LinearSum(U)*
B	*SquaredSum(U)*
C	*MaxSum(U)*

(b) Added turbulence intensity

Method in Tab. 1.1b	Name
A	*LinearSum(Ti)*
B	*SquaredSum(Ti)*
C	*MaxSum(Ti)*
D	*FullSquaredSum(Ti)*

4.3.1 Superposition methods for added turbulence intensity

In the first part of this case study, the focus is on the analysis of the added turbulence intensity superposition methods. A key element to bear in mind is that the velocity deficit superposition methods have an impact on the turbulence intensity field only through varying the thrust coefficient C_T. Given that all the turbines in the array operate in their constant C_T region (Sec. 4.2.1), the selected deficit superposition method has no effect on the turbulence intensity field, such that the turbulence superposition methods in Tab. 4.3b are all tested in parallel to the *LinearSum(U)* method. The corresponding results are shown in Fig. 4.5 for the average and the maximum turbulence intensity in the combined wake, *i.e.* $\mathrm{Ti}_{k,avg}$ and $\mathrm{Ti}_{k,max}$ respectively. As mentioned earlier in Sec. 4.2.3, the average of the Reference turbulence intensity is computed over the EllipSys grid while that of Model 1, Model 2 and Model 3 (Tab. 4.2) are recovered from the *PostProcessing* block (Fig. 4.2) with $N = 7$.

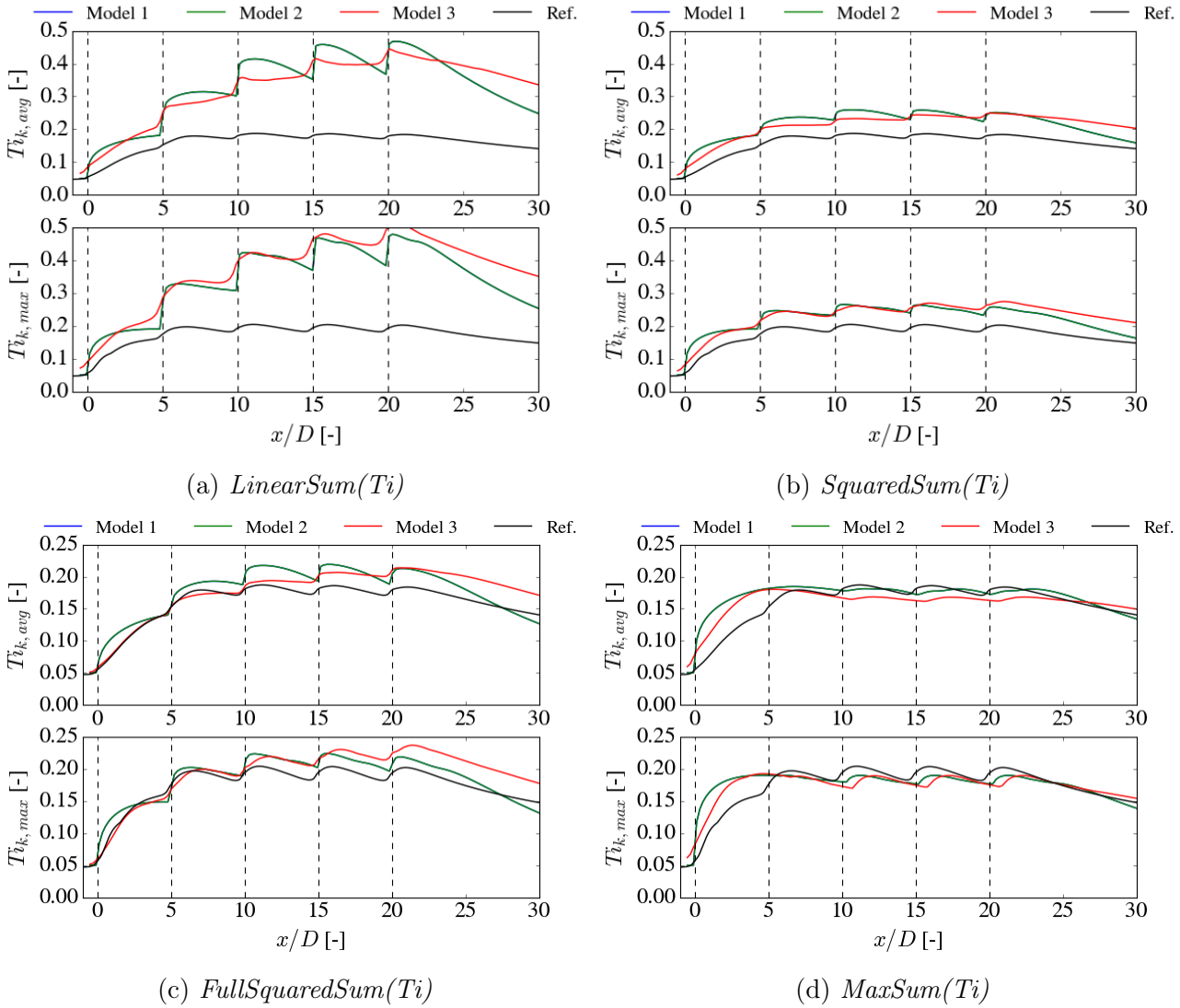

(a) *LinearSum(Ti)*

(b) *SquaredSum(Ti)*

(c) *FullSquaredSum(Ti)*

(d) *MaxSum(Ti)*

Figure 4.5: Comparison of the four turbulence superposition methods listed in Tab. 4.3b in terms of the maximum and averaged values of the wake turbulence intensity. *LinearSum(U)* is the velocity deficit superposition method used in each case. The position of each of the five turbines in the array is indicated by a black vertical dotted line.

First and foremost, the excellent agreement observed between Model 2 and Model 3 for all the superposition methods must be highlighted. This shows evidence that the errors introduced during the single-wake modelling step do not drastically increase as a result of the superposition process. Note that in Fig. 4.5, the curves of Model 2 overlap that of Model 1 since the turbulence field does not depend, in the case studied, on the velocity deficit model employed. From Fig. 4.5a, it appears clear that using a linear superposition method to compute the turbulence intensity field leads to a considerable overestimation of the Reference values, both for $\mathrm{Ti}_{k,avg}$ and $\mathrm{Ti}_{k,max}$. This overestimation can be halved by selecting the *SquaredSum(Ti)* method, as shown in Fig. 4.5b. Further reduction of the discrepancies between the modelled

and the Reference values can be obtained with the *FullSquaredSum(Ti)* (Fig. 4.5c). This is an important result of this section, as it seems to support the hypothesis that the turbulent kinetic energies add up in a combined wake (Eq. 1.13). In view of the definition chosen in Sec. 1.2.2 for the added turbulence intensity (Eq. 1.12), it is also not surprising to observe a better fit with *FullSquaredSum(Ti)* than with *SquaredSum(Ti)*. Note that the axes scale is modified in Fig. 4.5c and Fig. 4.5d for readability. In Fig. 4.5c, Model 2 seems to provide a slightly better approximation of the Reference curve for $\mathrm{Ti}_{k,max}$ than for $\mathrm{Ti}_{k,avg}$. This may be due to the fact that the new turbulence model has been precisely calibrated on the basis of the maximum added turbulence intensity values over the rotor section, as explained in Sec. 3.2.1.

Eventually, Fig. 4.5d shows that the closest match can be achieved for both $\mathrm{Ti}_{k,avg}$ and $\mathrm{Ti}_{k,max}$ using *MaxSum(Ti)*. In the wake of the first upstream wind turbine, *MaxSum(Ti)* however reduces to *LinearSum(Ti)*, leading to the significant overestimation observed in Fig. 4.5d for $\tilde{x} \leqslant 5$. A path worth exploring would be to enrich the analysis with Method E (Tab. 1.1b), for which *FullSquaredSum(Ti)* is recovered below $\tilde{x} = 5$. In the scope of this study, it is disputable as to which of the *FullSquaredSum(Ti)* method or the *MaxSum(Ti)* method should be retained. As introduced in Sec. 1.2.3, it is shown in Lingkan and Buxton [19] that the most upstream turbine seems to have dominant effects for spacings as large as $\tilde{x} = 5$. The same study however demonstrates that *FullSquaredSum(Ti)* leads to fewer discrepancies if the spacing is reduced to $\tilde{x} = 3$. In light of these results, future works could tackle the investigation of the minimum spacing below which the effect of all the upstream turbines must be accounted for. This study could then be used to determine a hybrid superposition method, consisting of *FullSquaredSum(Ti)* below the critical distance and *MaxSum(Ti)* above it.

4.3.2 Superposition methods for velocity deficit

Contrary to Sec. 4.3.1, in which the velocity field had no influence of the turbulence intensity field, the analysis of the velocity deficit superposition methods also depends on the turbulence superposition method used. Indeed, Ti_k affects the wake expansion coefficient k (Eq. 3.2) and therefore impacts the recovery of the velocity deficit in the wake. For that reason, the velocity deficit superposition methods listed in Tab. 4.3a are tested together with *FullSquaredSum(Ti)* and *MaxSum(Ti)*. The resulting values of U_{avg} are depicted in Fig. 4.6 for each single-wake models summarized in Tab. 4.2.

Fig. 4.6 clearly shows that, although minor differences can be noticed between the velocity fields computed with different turbulence superposition methods, the choice of the velocity deficit superposition method is much more decisive. Similarly, the choice of the single-wake velocity deficit model (either *NiayifarGaussianEff* or *LUT_Deficit*) has more impact on the total velocity field than the choice of the single-wake added turbulence model (*THD2023TurbulenceModel* or *LUT_Turb*). For that reason, Model 2 and Model 3 are barely distinguishable from one another. In Fig. 4.6, the *LinearSum(U)* method clearly stands out (Fig. 4.6a and Fig. 4.6b). Combined with either *FullSquaredSum(Ti)* or *MaxSum(Ti)*, the *LinearSum(U)* method indeed allows to recover excellent estimations of the Reference velocity field. The corresponding discrepancies are observed to be significantly smaller than for

Fig. 4.6c, Fig. 4.6d, Fig. 4.6e and Fig. 4.6f. As mentioned in Sec. 1.2.3, Lissaman [31] suggests that *LinearSum(U)* can be seen as a first order approximation of the conservation of momentum. Additionally, the accurate modelling of the turbulence intensity field allows to reliably account for the recovery of the velocity deficit. Therefore, no negative flow velocities occur, contrary to what could have been anticipated from Crespo et al. [32].

It is interesting to note that, while *MaxSum(Ti)* gives good estimates of the turbulence intensity field, the same conclusion cannot be drawn with *MaxSum(U)*, as demonstrated by Fig. 4.6e and Fig. 4.6f. Moreover the induction zone, *i.e.* the region upstream of a turbine subject to blockage effects, is visible for the Reference curve in all the sub-figures of Fig. 4.6. This slight velocity decrease, particularly observable upstream of the first turbine, is symptomatic of the blockage effect. As this effect is not taken into account by any of the models studied here, the velocity field predicted by Model 1, Model 2 and Model 3 falls sharply after each new downstream turbine.

In Fig. 4.6a and Fig. 4.6b, Model 1 can be seen to repeatedly under- and over-estimate Model 3 and the Reference curve. Therefore, the decision whether or not to replace *LUT_Deficit* with *NiayifarGaussianEff* depends on the margin of error allowed in the given situation. Since the predicted power evolves as the cube of the wind speed (Eq. 1.1), it seems reasonable to retain the *LUT_Deficit* single-wake model over *NiayifarGaussianEff* in the scope of this work.

To conclude, the analysis carried out in Sec. 4.3.1 and continued in this section has shown that the turbulence superposition methods *FullSquaredSum(Ti)* and *MaxSum(Ti)* led to little errors with respect to the Reference values. Moreover, the possibility to use the new added turbulence intensity model, *THD2023TurbulenceModel*, as a reliable alternative to *LUT_Turb* has been demonstrated. In this section, the *LinearSum(U)* velocity deficit superposition method was found to outperform the two other tested methods. Eventually, emphasis was placed on the substantial error introduced by the *NiayifarGaussianEff* single-wake deficit model. Hence, it can be concluded that Model 2, although not as memory-efficient as Model 1, appears to be a promising way of reducing by half the memory requirements of the initial RANS look-up table model, without affecting the quality of the predicted Ti_k and U values.

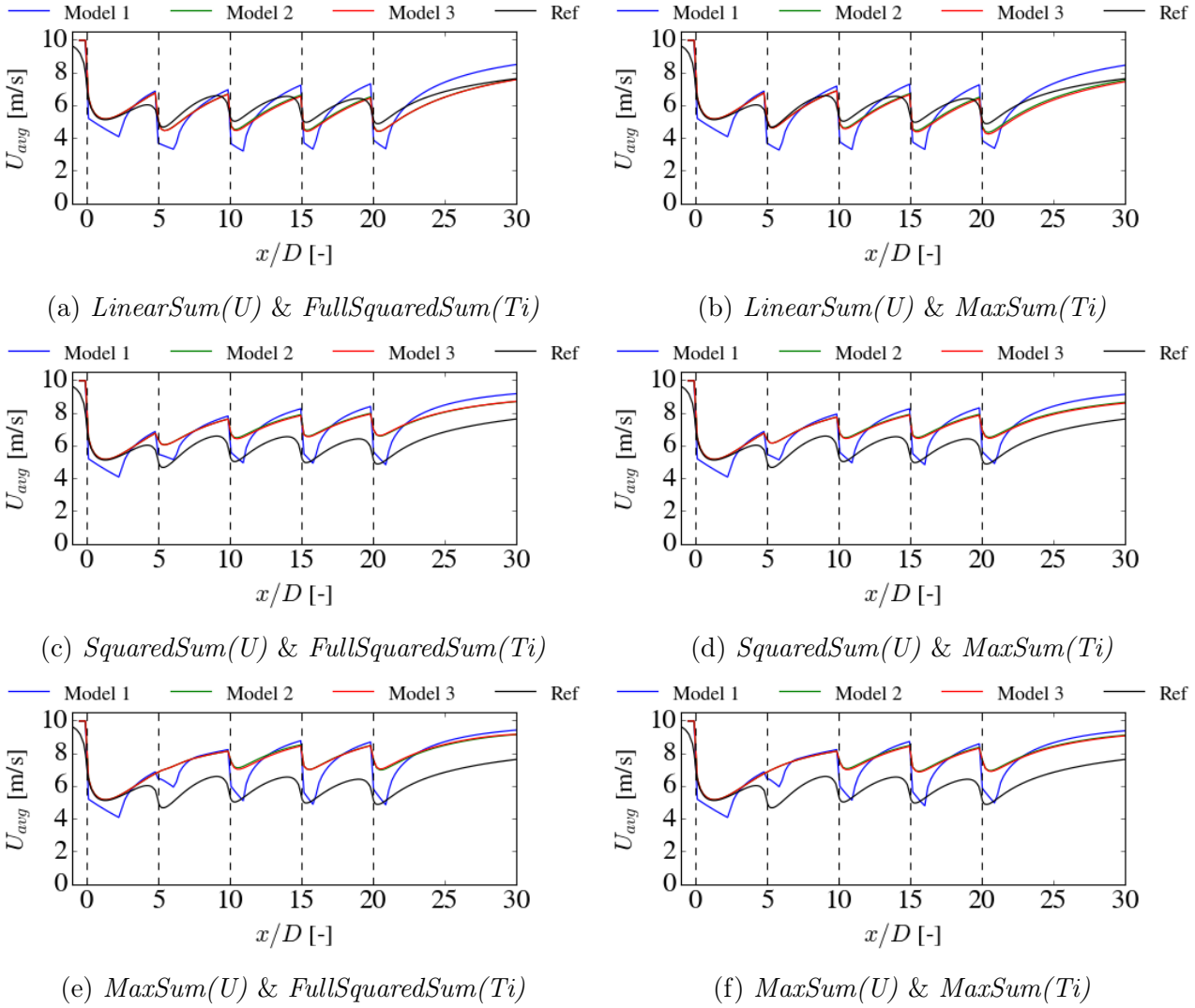

(a) *LinearSum(U) & FullSquaredSum(Ti)*

(b) *LinearSum(U) & MaxSum(Ti)*

(c) *SquaredSum(U) & FullSquaredSum(Ti)*

(d) *SquaredSum(U) & MaxSum(Ti)*

(e) *MaxSum(U) & FullSquaredSum(Ti)*

(f) *MaxSum(U) & MaxSum(Ti)*

Figure 4.6: Comparison of the three velocity deficit superposition methods listed in Tab. 4.3a in terms of the averaged velocity. *FullSquaredSum(Ti)* is used in (a), (c) and (e). *MaxSum(Ti)* is used in (b), (d) and (f). The position of each of the five turbines in the array is indicated by a black vertical dotted line.

Chapter 5

Conclusion

5.1 Summary

This final section provides a brief summary of the issues addressed in this work and the main results obtained in each part. Primarily, the first chapter outlines the main objectives of this work and examines the physics of the flow in a wind farm. The notions of velocity deficit ΔU, added turbulence intensity $\Delta \mathrm{Ti}_k$ as well as the concepts of wake recovery and blockage effects are introduced. This is followed by a in-depth review of the current velocity deficit and added turbulence intensity models. The superposition methods currently used to model wind farm flows are discussed, along with their physical interpretations. The differences between the existing definitions of the added turbulence intensity are highlighted and clarified.

In the second chapter of this work, the decomposition of the Reynolds stress lead to the theoretical determination of two suitable scalings of the added turbulence intensity. Subsequently, a comparison between the RANS data generated by EllipSys and the existing models enables to identify which of these models offer the most accurate representation of the RANS database. Each of the two theoretical scalings is then used to define a corresponding new added turbulence intensity model. In both cases, a product of three functions is employed to model the evolution of $\Delta \mathrm{Ti}_k$ with thrust coefficient C_T, downstream distance x and inflow turbulence Ti_k^0. However, by comparison with the RANS database, no clear trend stands out for the dependence on Ti_k^0, which therefore remains undetermined. This leads to the development of a hybrid model based on the two scalings, designed to more reliably represent the evolution of $\Delta \mathrm{Ti}$ with x. Despite a local improvement around $x = 1D$, this method appears still insufficient to fully establish a new added turbulence model. Nevertheless, an important result obtained in this section is the analytical expression for the position $\tilde{x}_{max}$ of the added turbulence intensity peak $\Delta \mathrm{Ti}_{k,absmax}$. In light of this last result, a new $\Delta \mathrm{Ti}_k$ model is written using a self-similar function f_N. A relation is proposed for $\Delta \mathrm{Ti}_{k,absmax}$, the modelling complexity of which is deduced to be strongly related to the definition used for $\Delta \mathrm{Ti}_k$. In addition, the Rayleigh function suggested by Scott et al. [35] is replaced by a modified Weibull law for f_N, thus introducing an additional parameter and greater flexibility into the model. Overall, the resulting $\Delta \mathrm{Ti}_k$ model shows good agreement with the RANS database and, in general, leads to lower error than the

traditional models. Eventually, an analytical sensitivity study provides a more in-depth view of the model.

The third chapter tackles the determination of a two-dimensional single-wake model for both the turbulence and the velocity field. To do so, a re-calibration of the velocity deficit model proposed by Niayifar and Porté-Agel [17] is performed and enriched with a sensitivity analysis. Overall, the re-calibrated model for the deficit shows encouraging results and is generalized in three-dimension under the axisymmetric wake assumption. Similarly, an axisymmetric profile of added turbulence is studied and represented by a Gaussian two-term, the amplitude of which is determined by $\Delta \mathrm{Ti}_k$. The sensitivity to amplitude and wake width modeling errors is discussed in parallel. Although excellent results are obtained for the two-dimensional added turbulence intensity model, the extrapolation of this profile to a three-dimensional axisymmetric model is seen to be more disputable than for the deficit.

In the fourth chapter, the focus is placed on the testing of the new model in a multiple-wake situation. In particular, the configuration consists in a row of five wind turbines operating in common flow conditions. The PyWake software is introduced, together with the key elements related to the implementation of the new wake model. Particular attention is paid to the development of a reliable averaging method of the flow quantities. In this section, the results of a RANS simulation of the whole array are used as a reference, against which the superposition of different combinations of ΔU and Ti_k models are tested. This allows to investigate both the superposition methods themselves and the degree to which the new wake model can effectively replace the RANS look-up table model. For $\Delta \mathrm{Ti}_k$, the study reveals a close correspondence between the new model and the initial RANS look-up table model, whatever the superposition method used. Moreover, two superposition methods lead to substantial reductions of the discrepancies with respect to the RANS simulation of the whole array. The former is consistent with the assumption of the additive nature of the turbulent kinetic energy, while the latter assumes that only the wake of the most upstream turbine should be considered. This analysis therefore reveals a close link between the definition chosen for $\Delta \mathrm{Ti}_k$ and the suitable superposition method. The study of the velocity deficit in the merged wake clearly indicates that the linear approach is the most appropriate. Eventually, the large discrepancies obtained with the new wake velocity deficit model suggest the use of an hybrid model. This in-between solution, relying on the new added turbulence intensity model in parallel to the RANS look-up table modelling of the velocity deficit, is a promising first step towards a more efficient RANS modelling of the wake.

5.2 Future perspectives

Throughout this work, several avenues for improvements have been suggested. To conclude, a few points that could be the topic of future projects are addressed. Subject to certain assumptions, a theoretical analysis has allowed to obtain a rough idea of the evolution of turbulence in the wake. In order to overcome the empiricism of the models developed in this project, the theoretical analysis could be pursued further to build more physically-based models. It has also

been explicitly shown that the data in the RANS look-up table are intrinsically flawed. Therefore, the methodology followed in this work could be applied to a higher fidelity database, for example resulting from LES simulations. In addition, some improvements to the method itself can be pointed out. A better representation of the turbulent wake growth could be studied by combining the new model with the wake expansion equation recommended by Nygaard [10] (Sec. 3.2.1). In addition, a correction term could be applied to the two-dimensional profile to reduce the large deviations arising from the axisymmetric wake assumption (Sec. 3.2.2). The study of the merged wake considered in Chapter 4 is limited to a single row of wind turbines and could therefore be pursued in a more complex configuration. In addition, as suggested in Sec. 4.3.1, the impact of the rotor spacing on the suitable superposition methods could be analysed in a specific study. Finally, the PyWake software could be further exploited to study the performances of the new added turbulence intensity model in the case of significant blockage effects.

Appendix 1

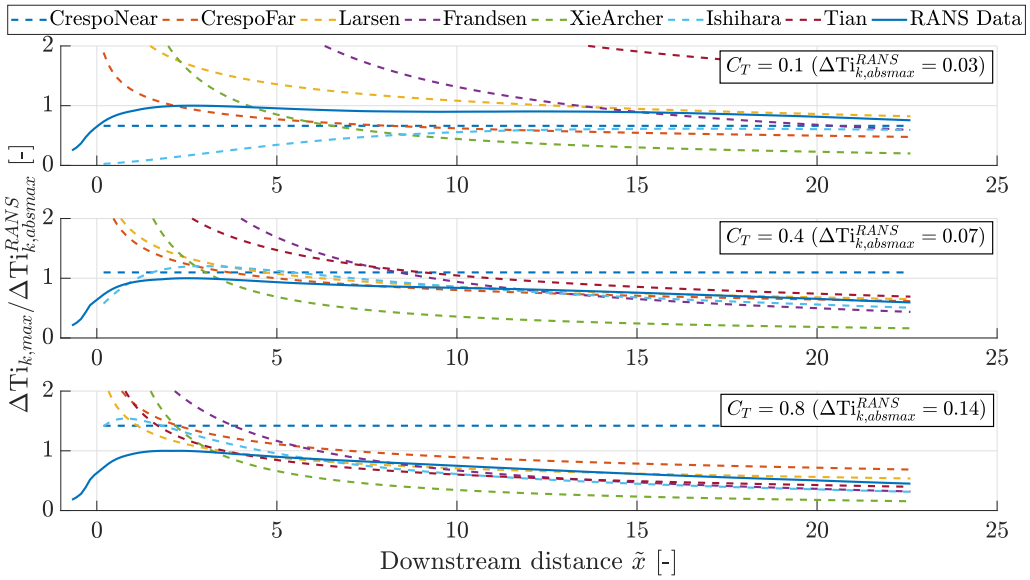

Figure 5.1: Comparison of $\Delta \mathrm{T}_{k,max}(x/D)$ as computed by the RANS simulations and as predicted by the existing models for $\mathrm{Ti}_0^k = 0.15$ and different values of C_T. Data are normalized by the maximal value of the RANS added turbulence intensity over the 3D domain ($\Delta \mathrm{Ti}^{RANS}_{k,absmax}$).

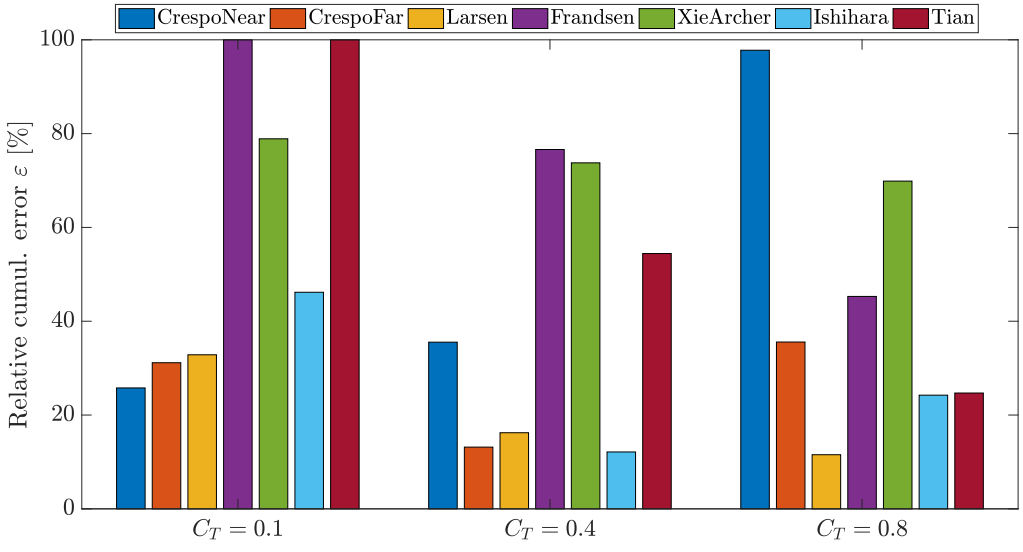

Figure 5.2: Comparison of the relative cumulative error ε (Eq. 2.14) for each existing model under $\mathrm{Ti}_0^k = 0.15$ and different C_T conditions.

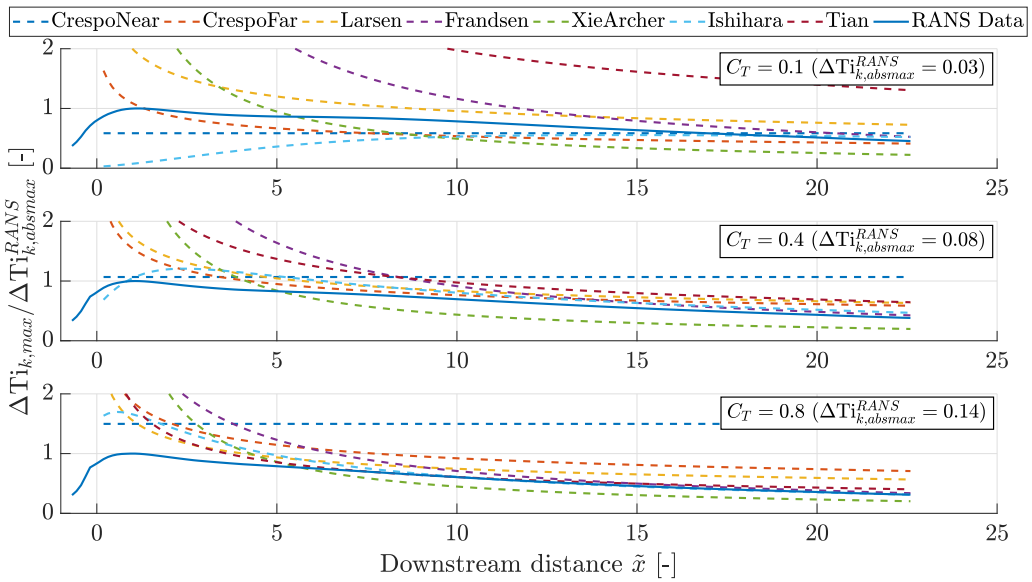

Figure 5.3: Comparison of $\Delta \mathrm{T}_{k,max}(x/D)$ as computed by the RANS simulations and as predicted by the existing models for $\mathrm{Ti}_0^k = 0.30$ and different values of C_T. Data are normalized by the maximal value of the RANS added turbulence intensity over the 3D domain ($\Delta \mathrm{Ti}^{RANS}_{k,absmax}$).

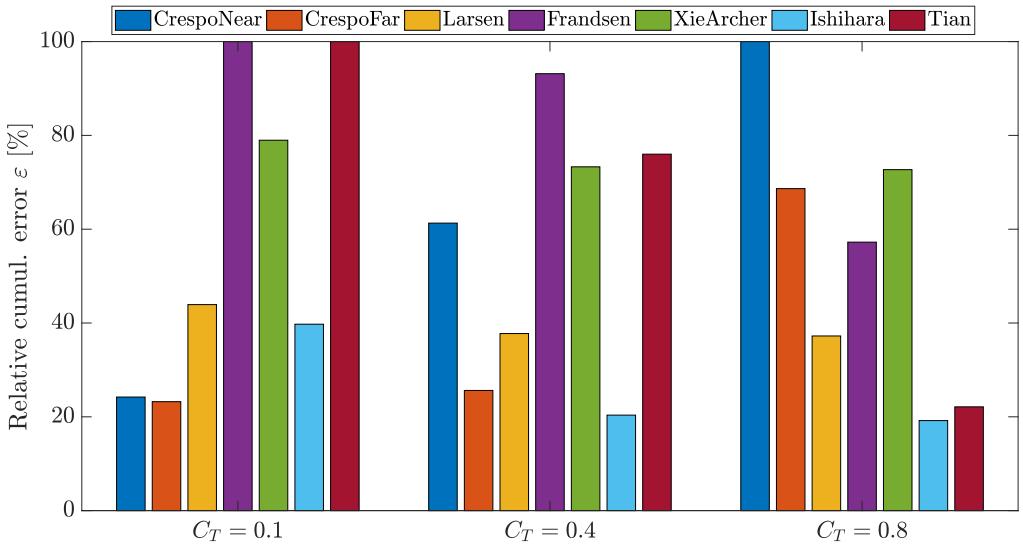

Figure 5.4: Comparison of the relative cumulative error ε (Eq. 2.14) for each existing model under $\mathrm{Ti}_0^k = 0.30$ and different C_T conditions.

Appendix 2

Ti_k^0	0.04	0.047	0.05	0.1	0.15	0.2	0.30	0.4
$C_T = 0.1$	0.296	0.2765	0.2695	0.0820	0.0450	0.0485	0.0505	0.0460
$C_T = 0.2$	0.3515	0.3130	0.3015	0.1080	0.0595	0.0550	0.0485	0.0405
$C_T = 0.3$	0.3960	0.3530	0.3350	0.1295	0.0750	0.0650	0.0530	0.0435
$C_T = 0.4$	0.4225	0.3775	0.3595	0.1450	0.0900	0.0740	0.0580	0.0460
$C_T = 0.5$	0.4240	0.3920	0.3785	0.1720	0.1055	0.0835	0.0625	0.0485
$C_T = 0.6$	0.3975	0.3495	0.2800	0.1805	0.1130	0.0845	0.0670	0.0510
$C_T = 0.7$	0.3650	0.3275	0.3170	0.1895	0.1290	0.0935	0.0715	0.0535
$C_T = 0.8$	0.3300	0.3055	0.2930	0.1505	0.1350	0.1030	0.0760	0.0560

Table 5.1: Look-up table for the values of the m parameter

Bibliography

[1] Paul van der Laan. *EllipSys3D large eddy simulation data of single wind turbine wakes in neutral atmospheric conditions*. URL: https://doi.org/10.11583/DTU.10259936.v1. (accessed: 09.06.2023).

[2] DTU Wind Energy. *PyWakeEllipSys*. URL: hhttps://topfarm.pages.windenergy.dtu.dk/cuttingedge/pywake/pywake_ellipsys/v3.5/introduction.html. (accessed: 06.06.2023).

[3] S. Haiying, G. Xiaoxia, and Y. Hongxing. "A review of full-scale wind-field measurements of the wind-turbine wake effect and a measurement of the wake-interaction effect". In: *Renewable and Sustainable Energy Reviews* 132 (2020), p. 110042. URL: https://doi.org/10.1016/j.rser.2020.110042.

[4] N. Wildmann, N. Vasiljevic, and T. Gerz. "Wind turbine wake measurements with automatically adjusting scanning trajectories in a multi-Doppler lidar setup". In: *Atmospheric Measurement Techniques* 11 (2018), pp. 3801–3814. URL: https://doi.org/10.5194/amt-11-3801-2018.

[5] N.O. Jensen. "A note on wind generator interaction". In: *Risø - M* 2411 (1983). URL: https://backend.orbit.dtu.dk/ws/portalfiles/portal/55857682/ris_m_2411.pdf.

[6] I. Katic, J. Højstrup, and N.O Jensen. "A simple model for cluster efficiency". In: *EWEC'86. Proceedings* 1 (1987), pp. 407–410. URL: https://backend.orbit.dtu.dk/ws/portalfiles/portal/106427419/A_Simple_Model_for_Cluster_Efficiency_EWEC_86_.pdf.

[7] R.J. Barthelmie et al. "Modelling and measuring flow and wind farm turbine wakes in large wind farms offshore". In: *Wind Energy* 12 (2009), pp. 431–444. URL: https://doi.org/10.1002/we.348.

[8] N.G. Mortensen et al. *Wind Atlas Analysis and Application program (WAsP): Vol. 1: Getting started*. English. Vol. 1. Risø-I 666(v.1)(ed.2)(EN). Risø National Laboratory, 1998.

[9] DTU Wind Energy. *PyWake*. URL: https://topfarm.pages.windenergy.dtu.dk/PyWake/notebooks/Overview.html. (accessed: 31.05.2023).

[10] N.G. Nygaard et al. "Modelling cluster wakes and wind farm blockage". In: *Journal of Physics: Conference Series* 1.1618 (2020), pp. 407–410. URL: https://backend.orbit.dtu.dk/ws/portalfiles/portal/106427419/A_Simple_Model_for_Cluster_Efficiency_EWEC_86_.pdf.

[11] S.T. Frandsen. "Turbulence and turbulence-generated structural loading in wind turbine clusters". In: (2007). URL: https://orbit.dtu.dk/en/publications/fc7f0107-228f-4f0f-9884-134cafdacbb2.

[12] G.C Larsen. "A simple wake calculation procedure". In: *Risø - M* 2760 (1988). URL: https://backend.orbit.dtu.dk/ws/portalfiles/portal/55857682/ris_m_2411.pdf.

[13] G.C Larsen. "A simple stationary semi-analytical wake model". In: *Technical report Risø* (2009). URL: https://backend.orbit.dtu.dk/ws/portalfiles/portal/122941920/Simple_analytical_wake_model_final_10.pdf.

[14] S. Frandsen et al. "Analytical modelling of wind speed deficit in large wind farms". In: *Wind Energy* 9 (2006), pp. 39–53. URL: https://doi.org/10.1002/we.189.

[15] M. Bastankhah and F. Porté-Agel. "A new analytical model for wind-turbine wakes." In: *Renew. Energy* 70 (2014), pp. 116–123. URL: https://doi.org/10.1016/j.renene.2014.01.002.

[16] C.R. Shapiro, D.F. Gayme, and C. Meneveau. "Modelling yawed wind turbine wakes: a lifting line approach". In: *J. of Fluid Mech.* 841 (2018).

[17] A. Niayifar and F. Porté-Agel. "Analytical Modeling of Wind Farms: A New Approach for Power Prediction". In: *Energies* 9 (2016), p. 741. URL: https://doi.org/10.3390/en9090741.

[18] A. Crespo and J. Hernandez. "Turbulence characteristics in wind-turbine wakes". In: *Wind Engineering and Indus. Aero.* 61 (1996), pp. 71–85. URL: https://doi.org/10.1016/0167-6105(95)00033-X.

[19] E. Lingkan and O. Buxton. "An assessment of the scalings for the streamwise evolution of turbulent quantities in wakes produced by porous objects". In: *Renewable Energy* 209 (2023), pp. 1–9. URL: https://doi.org/10.1016/j.renene.2023.03.101.

[20] F. Blondel and M. Cathelain. "An alternative form of the super-Gaussian wind turbine wake model". In: *Wind Energ. Sci.* 5 (2020), pp. 1225–1236. URL: https://doi.org/10.5194/wes-5-1225-2020.

[21] H.A. Panofsky and J.A. Dutton. *Atmospheric turbulence*. Wiley, 1984.

[22] G.C. Larsen. "Wind fields in wakes". In: *1996 European Union wind energy conference. Proceedings* (1996), pp. 764–768. URL: https://orbit.dtu.dk/en/publications/wind-fields-in-wakes.

[23] S. Xie and C. Archer. "Self-similarity and turbulence characteristics of wind turbine wakes via large-eddy simulation." In: *Wind Energ.* 18 (2015), pp. 1815–1838. URL: https://doi.org/10.1002/we.1792.

[24] G.W. Qian and T. Ishihara. "A New Analytical Wake Model for Yawed Wind Turbines." In: *Energies* 11 (2018), p. 665. URL: https://doi.org/10.3390/en11030665.

[25] L. Tian et al. "A new three-dimensional analytical model for wind turbine wake turbulence intensity predictions." In: *Renew. Energy* 189 (2022), pp. 762–776. URL: https://doi.org/10.1016/j.renene.2022.02.115.

[26] S. Zbigniew. "Structure of the atmospheric boundary layer". In: *Prentice Hall Advanced Reference Series* (1989).

[27] D.C. Quarton and J.F. Ainslie. "Turbulence in Wind Turbine Wakes". In: *Wind Engineering* 14.1 (1990), pp. 15–23. URL: http://www.jstor.org/stable/43749409.

[28] P.E.J. Vermeulen. "An Experimental Analysis of Wind Turbine Wakes." In: *Int. Symp. on Wind Energy Syst.* (1980), pp. 431–450. URL: https://ui.adsabs.harvard.edu/abs/1980wes..symp..431V/abstract.

[29] Haohua Zong and Fernando Porté-Agel. "A momentum-conserving wake superposition method for wind farm power prediction". In: *Journal of Fluid Mechanics* 889 (2020), A8. DOI: 10.1017/jfm.2020.77.

[30] E. Machefaux, G.C. Larsen, and J.P.M. Leon. In: *Journal of Physics: Conference Series* 625 (2015).

[31] Peter B. S. Lissaman. "Energy Effectiveness of Arbitrary Arrays of Wind Turbines". In: *Journal of Energy* 3 (1979), pp. 323–328.

[32] A. Crespo, J. Hernández, and S. Frandsen. "Survey of modelling methods for wind turbine wakes and wind farms". In: *Wind Energy* 2.1 (1999), pp. 1–24. URL: https://doi.org/10.1002/(SICI)1099-1824(199901/03)2:1%3C1::AID-WE16%3E3.0.CO;2-7.

[33] S. Voutsinas, K. Rados, and A. Zervos. "On the Analysis of Wake Effects in Wind Parks". In: *Wind Engineering* 14.4 (1990), pp. 204–219. URL: http://www.jstor.org/stable/43749429.

[34] M. Paul van der Laan et al. "An improved k- model applied to a wind turbine wake in atmospheric turbulence". In: *Wind Energy* 18.5 (2015), pp. 889–907. URL: https://onlinelibrary.wiley.com/doi/abs/10.1002/we.1736.

[35] R. Scott et al. "Evolution of the Eddy Viscosity in the Wake of a Wind Turbine". In: *Wind Energ. Sci.* 8 (2023), pp. 449–463. URL: https://doi.org/10.5194/wes-8-449-2023.

[36] Peter Davidson. *Turbulence: An Introduction for Scientists and Engineers*. Oxford University Press, 2015. URL: https://doi.org/10.1093/acprof:oso/9780198722588.001.0001.

[37] P.A. Durbin and R. Pettersson. *Statistical Theory and Modeling for Turbulent Flows*. 2010. URL: https://onlinelibrary.wiley.com/doi/book/10.1002/9780470972076.

[38] M. Bastankhah and F. Porté-Agel. "Experimental and theoretical study of wind turbine wakes in yawed conditions". In: *Journal of Fluid Mechanics* 806 (2016), pp. 506–541. URL: http://infoscience.epfl.ch/record/222488.

[39] M. Abramowitz and A. Stegun. *Handbook of Mathematical Functions*. Dover, 1970.